UFRGS
UNIVERSIDADE FEDERAL
DO RIO GRANDE DO SUL

Instituto de Física – IF

Magnetic White Dwarfs rich in Hydrogen

Larissa Luciano Amorim

Porto Alegre - RS

Junho de 2021

Larissa Luciano Amorim

Magnetic White Dwarfs rich in Hydrogen

Dissertação submetida ao Programa de Pós Graduação em Física do Instituto de Física da UFRGS, como quesito parcial para obtenção do título de Mestre em Física, com ênfase em Astronomia.

Universidade Federal do Rio Grande do Sul – UFRGS

Instituto de Física – IF

Supervisor: Dr. Kepler de Souza Oliveira Filho

Porto Alegre - RS

Junho de 2021

Este trabalho é dedicado a todas as pessoas que fazem a ciência brasileira avançar, apesar das adversidades.

Acknowledgements

Agradeço primeiramente à minha família pela companhia nessa parte da minha jornada, principalmente nos momentos turbulentos vividos devido à pandemia de COVID-19. Agradeço especialmente ao meu irmão Dann Luciano de Menezes, cujo apoio foi indispensável no desenvolvimento deste trabalho. Sou grata ainda aos amigos que mesmo distantes fisicamente permaneceram ao meu lado, me apoiando, em todos os momentos.

Gostaria de agradecer também aos colegas e professores do Instituto de Física da UFRGS com quem tive a oportunidade de interagir, mesmo que apenas remotamente, discutir e sobretudo aprender física e astrofísica.

Meus agradecimentos finais ao meu orientador pela oportunidade de estudar um assunto tão interessante e à CAPES pelo suporte financeiro à minha pesquisa.

"Joy does not come only from finding the discovery, but it is part of the search process. And teaching and learning cannot take place out of search, out of beauty and joy.
(Paulo Freire)

"A alegria não chega apenas no encontro do achado, mas faz parte do processo da busca. E ensinar e aprender não pode dar-se fora da procura, fora da boniteza e da alegria.
(Paulo Freire)

Resumo

Na busca para compreender a natureza e suas leis buscamos estudar a matéria sob as mais diversas condições. Nesse contexto, anãs brancas se mostram um excelente laboratório de pesquisa, podendo apresentar temperaturas, pressões e campos magnéticos inatingíveis na Terra. Para entender melhor como esses três parâmetros físicos interagem entre si e com outras características estelares, nós determinamos o campo magnético para 803 anãs brancas ricas em hidrogênio. Fizemos o ajuste aos espectros observados com o *Sloan Digital Sky Survey* usando modelos atmosféricos que consideram o efeito Zeeman decorrente do campo magnético em cada ponto do disco estelar. Além disso, determinamos o período de variabilidade fotométrica para 380 dessas anãs brancas observadas com o *Transiting Exoplanet Survey Satellite* e buscamos por correlações com as outras grandezas. Encontramos que as anãs brancas com campos magnéticos mais altos tendem a apresentar massas mais elevadas, temperaturas mais baixas e processo de cristalização já iniciado, reforçando a hipótese de o campo estar sendo gerado e/ou amplificado já no processo de resfriamento da anã branca. Nosso trabalho constitui a mais extensa determinação de campos magnéticos e períodos de rotação de anãs brancas obtidos até o presente.

Palavras-chaves:Anãs Brancas. Campo Magnético.

Abstract

The way to understand nature and its laws is through the study of matter under the most diverse conditions. In this context, white dwarfs prove to be an excellent research laboratory, as they reach have temperatures, pressures, and magnetic fields that are unattainable on Earth. To better understand how these three physical parameters interact with each other and with other stellar features, we determined the magnetic field strength for 803 hydrogen-rich white dwarfs. We fitted the spectra observed with the Sloan Digital Sky Survey using atmospheric models that consider the Zeeman effect due to the magnetic field at each point in the stellar disk. In addition, we determined the period of photometric variability for 380 of these white dwarfs observed with the Transiting Exoplanet Survey Satellite and looked for correlations with the other quantities. We found that the white dwarfs with higher magnetic fields tend to have higher masses, lower temperatures, and a crystallization process that has already begun. This reinforces the hypothesis that the field is being generated and/or amplified already in the cooling process of the white dwarf. Our work constitutes the most extended determination of magnetic fields and variation period of white dwarfs to the present day.

Key-words: White Dwarfs. Magnetic Field.

List of Figures

Contents

1 Introduction

Since immemorial times, humanity has been intrigued by the lights in the sky. This interest influenced the evolution of science, technology, and society as a whole. As our knowledge of astronomical objects evolved, so did our perception of the physical laws that influences our lives. This knowledge allowed us to build instruments to augment even further our understanding of nature.

From the beginning of our learning journey to the present day, we have already answered several questions such as where is the source of the light we see, what are these objects made of, where do they come from, why do they shine, why some are brighter than others, why they have different colors, will they always exist, and many others. As we attained more information, we grouped objects in categories in search of new insights, new answers, and new mysteries.

In this work, we delve into a particular subgroup of stars, the magnetic hydrogen-rich white dwarfs. Some questions that we hope to address, at least to some extent, are how frequent they are, where does the magnetic field come from, and how can it relate to other stellar parameters. To achieve this, we must investigate a large statistically significant sample of these stars. But before delving into these topics, it is necessary to understand the previous evolution of this group of stars to better base our study.

1.1 Stars

A fundamental tool in the study of stars is the Hertzsprung-Russell diagram (HRD). Developed independently with an observational and a theoretical approach by Ejnar Hertzsprung and Henry Norris Russell, this diagram presents stellar absolute magnitudes or luminosities versus their spectral classification/color index or effective temperatures. Not all regions of this diagram are populated equally, which led to the subdivision into different categories depending on which region of the plot the star belonged to. Some outstanding groups are the Main Sequence, the Red Giant Branch, the Asymptotic Giant Branch, and the White Dwarfs, but different classes stand out depending on the sample of stars under investigation.

Such classification proved to be fundamental for the understanding of stellar evolution, especially with the analysis of globular clusters which are groups of stars that are supposed to have the same age and metallicity by virtue of originating from the same cloud. The study of these clusters throws light on our understanding of how the mass of the star influences its evolution, which will be further discussed in the next section. One

example of HRD is illustrated in Fig. 1.

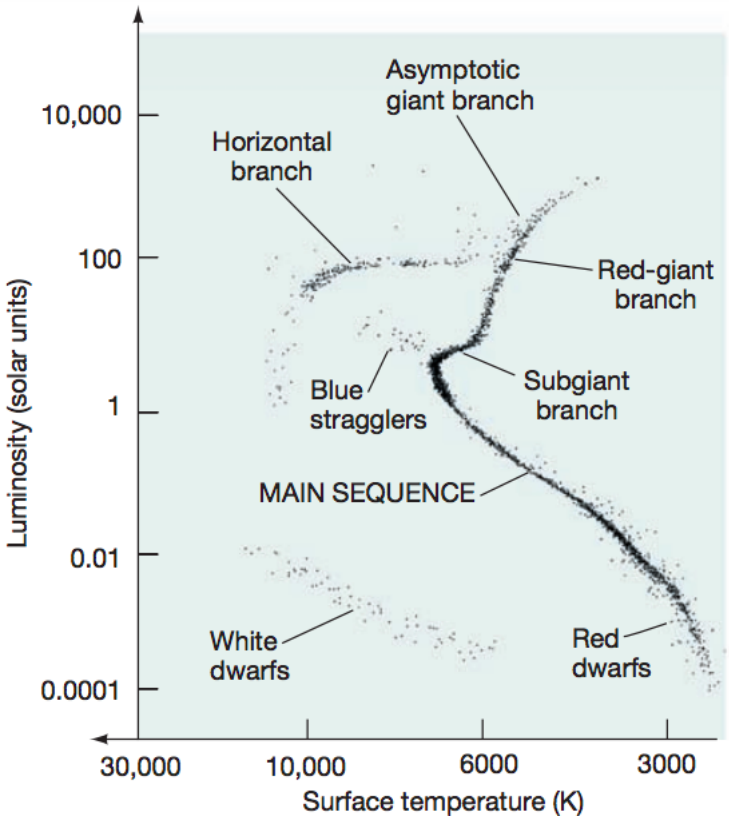

Figure 1 – Combined H–R diagram, based on ground- and space-based observations, for several globular clusters similar in overall composition to M80. The various evolutionary stages are visible. Note also the blue stragglers— main-sequence stars that appear to have been "left behind" as other stars evolved into giants. They are probably the result of mass transfer or merging binary systems or actual collisions between stars of lower mass in dense stellar systems. Original figure by Chaisson, and McMillian (2014)

1.2 Stellar Evolution

Stars are formed from huge clouds of dense gas. Clumps may start to form and grow by the effect of gravity due to small inhomogeneities of the distribution of matter. These clumps can achieve stability because their inner pressure can compensate for gravity. However, external perturbations may trigger a collapse, and, depending on the circumstances, each group can form a different number of stars.

Each fragment gives rise to a protostar after gravitationally contracting. The protostar has to be massive enough to ignite stable core hydrogen burning to become a star. That corresponds to roughly 0.08 $M_{\odot}$(solar mass) for gas with chemical composition similar to that of the Sun's atmosphere (approximately the solar metallicity).

Once core burning starts, the gravitational collapse will be compensated by the energy released from these reactions, and the star will remain in equilibrium for a long time (up to billions of years) until the hydrogen is exhausted from its core. This is one of

the longest stages in the stellar evolution, resulting in an overpopulated region of the HR diagram called Main Sequence. This stage is represented in the HRD in Fig. 2.

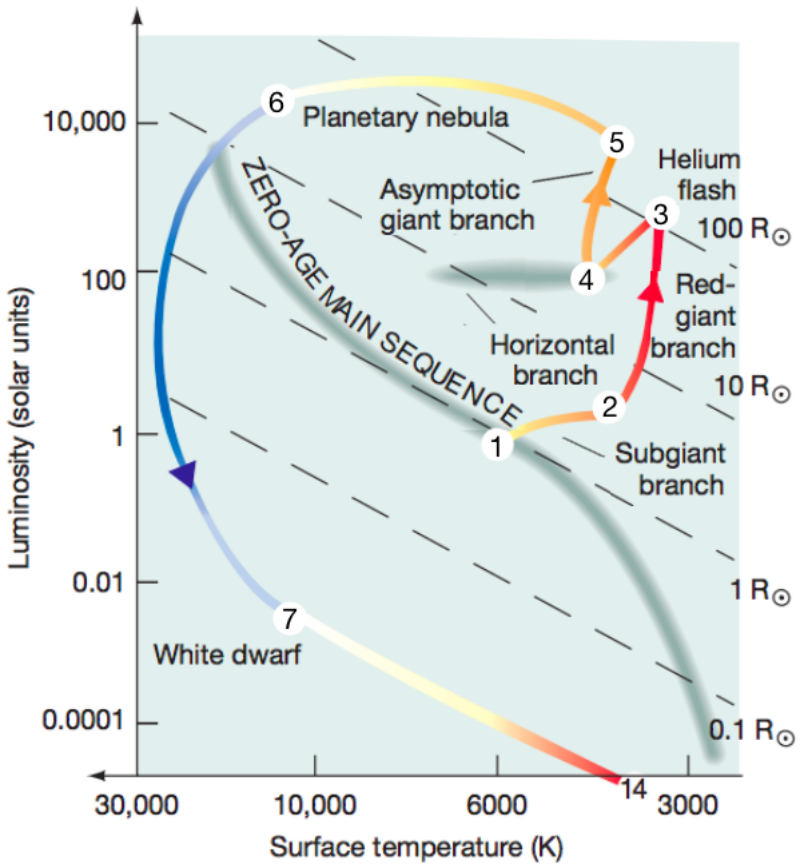

Figure 2 – Evolutionary path and stages after the Main Sequence for a star similar to the Sun in mass and metallicity. Figure adapted from Chaisson, and McMillian (2014)

The duration of core hydrogen burning depends upon the mass and metallicity of the star. The more massive the star, the hotter it is going to be in its core. Hence, the reactions will be more efficient and consume all the available fuel faster. The presence of metals in the stellar atmosphere obscures the outflow of energy from the stellar core, warming it up, and resulting in a similar effect of shortening this stage.

The effect of mass is evident in globular clusters. Since all stars have roughly the same age and metallicity, only the more massive stars had time enough to finish core hydrogen burning. This is seen in Fig. 1 as a "turn off point" of the main sequence and is used to constrain the age of the cluster.

When hydrogen is exhausted in the nuclei of stars, the balance between gravity and the pressure resulting from the energy released in nuclear reactions is lost. Therefore, the core collapses under gravity and contracts. The layers around it, however, still have hydrogen and a temperature high enough for fusion, so the nuclear reactions continue (on a shell).

The energy released by the contraction of the core partially contributes to heating the core itself. If it reaches a temperature around 10^8 K (or, correspondingly, masses around 0.45 $M_\odot$) the fusion of helium will occur. The other part of the energy is lost to the next layer and enhances the temperature of the shell. This makes hydrogen fusion more and more efficient, emitting increasingly more energy, which expands the outer layers of gas. Furthermore, the helium resulting from the burning in the layer increases the core mass. As the envelope becomes very extensive, the surface layer of the star cools, resulting in a reddish coloration. Stars in this stage fill a region in the HR diagram called Subgiant Branch.

The difference in temperature between the core and the surface gets high enough to make radiative transfer an inefficient energy transport mechanism. So, an extensive convective layer is formed. The star then starts to grow at almost constant effective temperature and fills a region in the HR diagram called Red Giant Branch (RGB).

As the star continues to expand, the convective zone deepens, possibly reaching the core and bringing heavier elements to the stellar surface. This phenomenon is known as the first dredge-up, and stars undergoing this process can be seen in an HRD as an overpopulated area of the RGB. The presence of metals in the atmosphere increases the opacity, preventing light to get to the surface, consequently reducing stellar luminosity and making the star stay on the same region of the diagram for a longer time.

The next stage of evolution is the core helium burning, which is different depending on the initial mass of the star. Those that began their evolution with masses smaller than 2 $M_\odot$will have inactive helium cores that grow in mass very slowly. The conditions in density and pressure will force all the electrons in it to be in the lower energy state possible, resulting in degeneracy pressure that opposes to the gravitational collapse. All matter in this degenerate core has the same increasing temperature. In consequence, when it reaches 10^8 K, a huge amount of helium is burnt in a very short timescale (of hours) in an episode called the helium flash. This event triggers a high energy release in the core of the star, causing it to expand and raising the degeneracy leading to a more stable fusion of helium (triple-α).

When the nucleus expands, it moves the hydrogen-burning layer to an outer and colder region of the star. Its productivity is reduced, resulting in a contraction of the star's surface layers. The radius contraction generates a decrease in the star's luminosity and an increase in surface temperature. This phenomenon is scaled by the mass and metallicity of the star, thus forming a horizontal branch in the HR diagram.

In opposition, when more massive stars run out of hydrogen in their cores, it is almost massive/hot enough to start helium burning. The triple-α starts before degeneracy is established, resulting in a stable fusion, without the "flash".

At this point, another bifurcation in evolution occurs. If the original mass of the star was higher than approximately 10 $M_\odot$, it will attain a temperature high enough to burn carbon and subsequent heavier atoms until iron. The fusion of iron is an endothermic process that absorbs energy and causes a collapse of the star, called a Supernova. If the star had a mass of less than about 25 $M_\odot$ in the Main Sequence, the remnants of this disruption will be a neutron star. Otherwise, it will become a black hole.

However, if the original mass of the star was lower than approximately 10 $M_\odot$, it will never attain a temperature high enough to burn carbon. When the nuclei of the stars run out of helium, they go through a new phase of growth of the outer envelope. This process is similar to the one present in the RGB (with another possible dredge up), and the region in the HRD is called the Asymptotic Giant Branch (AGB). Though, this time, the star has two sources of energy, the layer that burns hydrogen into helium and the layer that continues to burn helium into carbon, since the helium has depleted only in the core. It is noteworthy that the specific mass that distinguishes these different processes depends on the metallicity of the star and interactions with a possible close-by companion.

As the core is now inert, it gravitationally collapses, increasing its temperature and the temperature of neighboring layers. This time, the helium-burning process is taking place in the neighboring layer. Triple-α is even more temperature-dependent than the hydrogen-burning process (CNO cycle). As a result, the envelope expands even more than in the RGB with the energy coming from the burning in layers. This continuous expansion process is known as "early AGB".

The helium-burning layer becomes thinner as time passes. The dependence of the triple-α reaction on temperature is so high that the efficiency of the reactions at the base of the layer is much greater than that on the surface of the layer, causing the base to move towards the surface.

The thin thickness of the helium-burning layer causes an unstable burning process similar to the helium flash. However, the temperature continues to increase and feeds the efficiency of the reactions, not due to the degeneration of the gas, as in the previous case, but due to a geometric factor. This results in a large emission of energy in a short period called a thermal pulse.

This process is stopped by the fact that about half of the energy released is used in the expansion of the star. The result is an expansion of the layer in which helium burns and the process becomes stable again. This mechanism significantly changes the star's luminosity cyclically and can be observed. For more massive stars, the characteristic time can reach the order of 10 years. Despite the process being cyclical, the timescale is not constant, since the chemical composition of the star changes between pulses, as well as the mass, temperature, among other stellar features.

The expansion of the star also generates a detachment of the hydrogen-burning layer, which passes to colder regions. The conditions are no longer favorable to nuclear fusion and the production of helium ceases. The reactions are resumed as the luminosity decreases and the star contracts. In this process, there is also a strong loss of mass, as the star starts to present such a large radius that the outer layers suffer little gravitational influence when the contraction process starts, and part of this matter is no longer part of the star.

Furthermore, with each pulse, the luminosity released by the burning of hydrogen gets smaller, as the layer becomes more and more external, at lower temperatures. In contrast, the luminosity of helium is increased, among other factors, due to the increase in the carbon nucleus caused by the previous pulses. The contraction of the carbon nucleus releases more energy, increasing the temperature and triple-α efficiency.

In the last pulse, there is a greater loss of mass due to winds, as the envelope is already quite eroded due to previous pulses, and the energy released by the fusion of helium is the most powerful. The envelope's mass becomes too low to absorb all the energy released in the pulse. After this last pulse, the pressure that the remaining envelope makes on the inner layers is too low to maintain nuclear fusion conditions, and the reactions cease to occur.

As these outermost layers are lost in the pulses, the AGB stars are responsible for enriching the interstellar medium with heavy elements, along with supernovae. It is noteworthy that these heavier elements are not limited to carbon and oxygen. Nitrogen is produced in the dredge up process, taken to the nucleus, where it combines with an α particle, generates an atom of magnesium, and releases a neutron. As the neutron flux is low, there are processes of generation of heavier elements, possibly heavier than iron (some elements are produced only through this process and not in supernovae).

The last thermal pulses are responsible for the formation of the planetary nebula. The core that remains in the center of the system is exposed, has high temperatures (typically in the order of 10^5 K), and emits radiation that ionizes the surrounding gas, generating the visual effect that we detect.

The gas is slowly dispersed into the interstellar medium and the leftover hot core is gradually exposed. Duo to this process, we perceive the temperature of the system increasing. Later, the temperature drops due to the emission of energy. In this stage the star is called a white dwarf and it is usual to count its age (cooling age) starting when it achieves its maximum temperature. These objects have, in most cases, a C-O core and varying size layers of helium and hydrogen. It should be noted that stars that can't burn helium are also going to generate white dwarfs, but with He-cores. However, the time it would take for such low mass single stars to evolve out of the main sequence is bigger than the age of the universe. Hence, the He-core white dwarf that exist today are results

of the evolution of interacting multiple systems.

The white dwarf is the last stage of the stellar evolution. But, despite no longer having nuclear reactions in its core, the white dwarf still goes through several different physical processes. Beyond the cooling process by virtue of its luminosity, it also cools due to the emission of other particles, contracts its radius while at higher temperatures, undergoes sedimentation of heavier elements, crystallizes its core at lower temperatures among other phenomena.

The phenomenon of crystallization was first identified because when a star start to solidify (crystallize) its core, its temperature remains roughly constant. The solidification releases energy, slowing down the cooling process and making stars appear in a different region of the H-R Diagram. This effect can affect the whole structure of the white dwarf and can have a relation with the presence of magnetic fields, thus will be further investigated in this study. For more detailed explanations on stellar evolution see, for example, Erika (1992).

1.3 White Dwarfs

White dwarfs represent a good laboratory for studying matter under extreme conditions because they have densities of roughly 1 tonne per cubic centimeter (about a million times greater than the average density of the Sun) and may start with effective temperatures as high as 200 000 K, as seen above. They are also relevant on a cosmological scale since they represent the result of the evolution of all stars with an initial mass lower than $7-11$ $M_{\odot}$, depending on the metallicity, which represents 97 % of all stars (Lauffer; Romero; Kepler, 2018). In addition to the importance in absolute numbers, they stand out for being used in establishing limits to the age of galaxies once the less massive ones did not have time to cool down below our detection limits.

Despite having well defined major characteristics, white dwarfs can present very different spectra and are subdivided into groups. To understand these classes it is useful to comprehend the classification of stars in general.

Stars were classified according to the features apparent in their spectra since the XIX century. Notwithstanding the huge contribution of the different classification systems that have been developed over the years, most stars are currently classified under the Morgan–Keenan (MK) system. This organization is based on roman capital letters O, B, A, F, G, K, M sorted in order of decreasing temperature. In addiction to the MK system, other complementary classification system were created to encompass star-like objects that didn't fit the classical system as is the case for white dwarfs that receive the letter of identification D to denote that they are degenerate objects.

The class of white dwarfs was further divided according to the main elements present in the spectra: A for hydrogen, B for neutral helium, O for ionized helium, C for no spectral lines, Q for carbon, Z for metals, or X for spectra with no clear information. Besides the classification according to the atmospheric composition, another classification is made to relate different features as E for emission lines, V for variability, and P or H for magnetic field detection with or without polarization measurements. For more detailed explanations on the classification of white dwarfs see, for example, McCook, and Sion (1999).

We draw attention to the fact that not necessarily the spectra represent the atmospheric composition of the star since some atoms don't present observable lines at certain temperatures. For example, when DBs achieve temperatures below (8 000 K) the lines of helium disappear and we may observe a DC even though the star has a helium-dominated atmosphere.

As in this work we are interested in studying the magnetic field of a large sample of white dwarfs and it is impracticable to carry out individual polarimetric measurements, we choose to determine the magnetic field only based on spectra of the stars. In addition to that, we limit our sample to hydrogen-rich white dwarfs since this represents a considerable simplification for the models while maintaining 84% of the sample.

1.4 Magnetic Field

Electromagnetism is one of the fundamental forces of nature, and it has aroused questions that are crucial to the understanding of our Universe. A historical moment in which this was especially true was in 1896 when Pieter Zeeman observed a clear widening of the sodium D-lines under the influence of a magnetic field. Hendrik Antoon Lorentz developed a theory based on the existence of charged vibrating particles inside atoms.

He proposed that the observed widening was actually a splitting of the lines in three components when observed in a direction perpendicular to the field. His work also suggested that in a direction parallel to the field two lines would be visible, with opposite circular polarizations. This prediction was experimentally verified and the assumption made by Lorentz to his theory was corroborated, constituting the first indications of the existence of a new charged particle, later known as the electron.

More than a decade later, this same phenomenon was used by George E. Hale to demonstrate that sunspots were under the influence of magnetic fields. Regardless of its use, this effect was only better understood with the advent of quantum mechanics. Not only the quantization of atomic energy levels was necessary to explain the normal Zeeman effect, but also the existence of spin is needed to explain the anomalous Zeeman effect (splitting of the lines in more than three components).

To have an idea of the effect of the magnetic field in the stellar spectra we can look at a much simpler example, one hydrogen atom at low fields. If we do not consider the effect of the spin we have the normal Zeeman effect. We can write the Hamiltonian of the system starting with the Hamiltonian of the system without magnetic field and adding a term that represents the effect of the magnetic field. The same happens with the associated energy:

$$\hat{H} = \hat{H}_0 + \frac{B\mu_B}{\hbar}\hat{L}$$
$$E_{nlm} = E_n^0 + mB\mu_B,$$

where μ_B is the Bohr magneton, $\hat{L}$ is the orbital angular momentum and n, ℓ and m are quantum numbers.

Part of the degeneracy has been broken, in other words, levels that previously had the same energy now have different energies. We observe this as a split in the lines of absorption in the spectra since they reflect the difference in energy of the level between which the electron transits. A schematic idea of this phenomenon can be seen in Fig. 3.

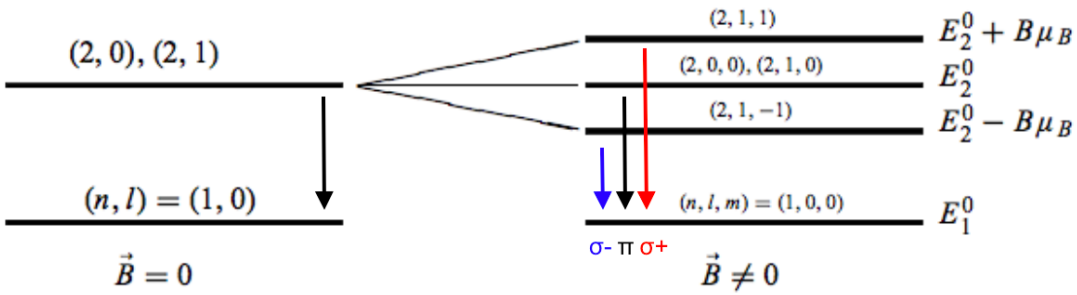

Figure 3 – Some energy levels of hydrogen without and with the action of a magnetic field. The colored arrows symbolize the absorption lines observed in the spectrum. Image adapted from Zettili (2009).

These effects were already used to find magnetic fields of the order of hundreds of millions of Gauss (MG) in white dwarfs, which are expected to last for millions of years. In comparison, the strongest continuous magnetic field we can create on state-of-the-art equipment on Earth are only of the order of a fraction of an MG.

1.5 Spectral Lines

As we will use spectral lines to estimate the magnetic field strength on the surface of the white dwarfs, it is crucial to comprehend our current knowledge on the physical process involved in its formation.

Our understanding of spectral lines has widened and deepened considerably since it was first systematically studied for the Sun by Joseph von Fraunhofer in the early XIX century. In addition to the more evident information about which elements are present in

the atmospheres of the stars, we can use spectra to estimate the effective temperature, the surface gravity, the magnetic field. One can also study its companions through the variation of the longitudinal velocity of the star or the difference between the spectra of the star and the spectra during eclipses.

All this is achievable because we attain information not only from the wavelength of the spectral line but also from its shape. If we were to consider only one atom, one could imagine that the spectral line should be infinitely thin. Only photons with the exact wavelength corresponding to the difference of energy of the level its transitioning to and from would be absorbed, expressed by

$$E = \frac{hc}{\lambda} = E_f - E_i \Rightarrow \lambda = \frac{hc}{E_f - E_i},$$

in which E_f and E_i are the energy of the final and initial states respectively.

But this is not observed because the uncertainty principle states that there must exist a limited certainty in the energy, dependent on how long is the lifetime of an excited state. That can be represented as

$$\Delta E \Delta t = \frac{\hbar}{2},$$

in which ΔE is the uncertainty in the energy of a transition, Δt its lifetime and $\hbar$ the Planck constant h divided by 2π. As a result of this effect, the spectral line takes on the shape of a Lorentzian profile. This is called natural broadening.

As we will study a gas, it is necessary to consider the velocity distribution of its atoms once the observed spectral line will suffer a shift in wavelength $\Delta\lambda$ due to the Doppler effect:

$$\Delta\lambda = \frac{v}{c}\lambda_0,$$

in which v is the velocity of the transitioning atom with respect to the measurement instrument which is much smaller than the velocity of light c. The original wavelength of the transition is λ_0.

A gas in thermal equilibrium has a Maxwell-Boltzman velocity distribution that depends on the temperature:

$$P(v)\ dv = \left(\frac{m}{2\pi k_B T}\right)^{1/2}\ e^{-\frac{mv^2}{2k_B T}}\ dv$$

in which $P(v)\ dv$ is the probability of one particle having velocity in the interval $[v, v+dv]$, m is the mass of the particles, k_B is the Boltzmann constant and T is the temperature.

As a result of this effect, even in thermal equilibrium, the spectral line takes on the shape of a Gaussian profile, which gets wider as the temperature increases. This is called the Doppler broadening.

Another source of broadening that can occur in stars is the rotation of the star along its axis. Because we see the star as a source point, the light emitted from the

different sides of the rotation axis will suffer contrasting shifts making the spectral line broader. However, this effect in broad lines of white dwarfs is too small to be measured with typical instruments, as was seen by Heber, Napiwotzki, and Reid (1997).

A further effect is pressure broadening, also known as collision broadening. When particles collide with the transitioning system, the emission or absorption is altered. The reduction in its characteristic time implies an augment in the uncertainty in the energy, as discussed in the natural effect. This causes a broadening of the line, but it can also introduce a wavelength shift of the center of the line, unlike the previously mentioned effects.

Aside from line broadening and wavelength shift, the line can be split due to the lifting of the atom's degeneracy. This occurs when the atoms are submitted to electric fields, Stark effect, or magnetic field, Zeeman effect. Even though these effects are in reality splitting the line, it is possible that when in convolution to the other effects the net outcome is a line broadening.

The Stark effect is usually the dominant one in white dwarfs and is employed to build models that are used to estimate two main properties, effective temperature, and surface gravity. However, the application of this method is not recommended for magnetic white dwarfs since the Zeeman splitting can be unresolved and misinterpreted as indication of a higher mass (Kepler et al., 2013).

1.6 Overview

The origin of magnetic fields in white dwarfs is an open question that has been addressed with different approaches for the past decades, some are presented in Chapter 2. However, most studies concentrate on small samples of stars. We would like to throw some light on this problem by building a large sample of magnetic white dwarfs.

To allow us access to data of many stars we choose spectroscopy (measuring the Zeeman spliting in spectral lines) as a method (instead of spectropolarimety, that can detect weaker magnetic fields but are available for much less stars). In addition to that we choose to study only white dwarfs with atmosphere dominated by hydrogen, since they are 84% of all white dwarfs and this simplifies a lot the estimation of the magnetic field magnitudes. The sources of our data are presented in Chapter 3.

As we want to understand better the origin of magnetic fields we determine some properties of the field in each star and its probable rotational period. Our methods are presented in Chapter 4 and our results can be seen in Chapter 5. We discuss the possible relation between magnetic field strength/incidence and stellar mass/temperature/crystallization status in Chapter 6 and we present our conclusions in Chapter 7.

2 Previous works

Magnetic fields of different orders of magnitude have been found in white dwarfs depending on the technique used. Vanlandingham et al. (2005) identified fields between 1.5 - 1 000 MG analyzing spectra, as we did in this work. Fields as low as 57 kG can be measured if spectropolarimetry is applied, as was done by Landstreet et al. (2016).

Strong magnetic fields are common in white dwarfs rich in hydrogen (DAs). Kepler et al. (2013) showed that at least 4% of all DAs observed with *Sloan Digital Sky Survey* (SDSS) until Data Release 7 have magnetic fields greater than 1 MG. The authors inspected visually all DA spectra and found 521 stars with Zeeman splittings. A more robust method to estimate the magnetic fields however was presented by Külebi et al. (2009), who used least-squares minimization to find the best model of magnetic field geometry to fit the observed data. They applied this technique to 141 magnetic white dwarfs rich in hydrogen (DAH). In this work, we use this method to estimate the magnetic field of 803 DAHs.

This systematic study is crucial to the construction of a significant statistical sample, and may help us better understand the origins of magnetic fields in white dwarfs, which is still an open question after more than fifty years of the first discovery by Kemp et al. (1970). The magnetic field could be formed in three different stages of the white dwarf (WD) evolution: before it starts to form, during its formation, or the cooling process.

The main hypothesis of the first group corresponds to the fossil fields from Ap/Bp stars (chemically peculiar and with stronger magnetic fields than classical A- or B-type stars). When stars have an initial mass above 1.5 $M_{\odot}$, they have convective cores during the main sequence in which a magnetic field can be formed through a dynamo process. These fields usually are small, of the order of a few kG as first shown by Babcock (1947). The magnetic field is boasted through conservation of the magnetic flux up to 100 MG when the star gets stripped of its outer layers and its core gets exposed and starts to contract.

This possible origin of the magnetic field is very attractive because the Ohmic decay in degenerate matter suggests that these fields should last billions of years. However, Wickramasinghe, and Ferrario (2005) concluded that the amount of magnetic Ap/Bp stars that have been detected cannot account for the fraction of magnetic white dwarfs (MWD) measured, so other mechanisms must be happening.

For the magnetic field to arise during the formation of the white dwarf, the system may not be single. It can be due to the merger of two degenerate cores or it can be formed during the interaction of the two components of the binary (common envelope)

as presented by (Tout et al., 2008). However, this channel of magnetism formation would lead to a much higher magnetic incidence among white dwarfs in close binaries than is currently observed (Belloni; Schreiber, 2020).

Measuring the rotational period of MWD may help us distinguish different origins. The ones descendant from mergers could show high speeds ($P_{rot} \sim$ minutes) as suggested by King, Pringle, and Wickramasinghe (2001). Extremely slow rotators ($P_{rot} >$ years) could be produced if the magnetic field locks the forming white dwarf to the escaping envelope of its progenitor as proposed by Spruit (1998).

Using the Jacobus Kapteyn Telescope, Brinkworth et al. (2013) studied the photometry of 30 isolated magnetic white dwarfs. They derived periods for 5 of them (between 105 minutes and 6.68 hours) and detected variability in 9 others. Kawka (2020) joined this data with other previously determined rotational periods in magnetic white dwarfs. Including other methods like spectropolarimetry, she built a sample of 38 stars and found that most of the magnetic white dwarfs have rotation periods shorter than 10 hours with a distribution peaking at 2 - 3 hours.

In this work, we search for photometric variability in light curves observed with *Transiting Exoplanets Survey Satellite* (TESS) and estimate a period of variability for 380 stars observed until sector 46, in December 2021. We don't expect the same distribution in periods as Kawka (2020) because most of our sample consists in 30 minutes cadence data, biasing our results against short periods.

The possible origins mentioned so far are in agreement with the higher mass that MWDs have when compared to the whole sample as presented by Kepler et al. (2013). Nevertheless, there is evidence of yet another way of forming magnetic fields in white dwarfs. Kepler et al. (2013) also stated that the distribution of the magnetic field strength with temperature has a peak in lower temperatures, which means that the white dwarf must be producing or enhancing the magnetic field.

When the white dwarf cools below 14 000 K, it develops a convective layer in which the dynamo process can occur, giving a boost to the field. However, as the temperature continues to drop, the kinetic energy of the envelope becomes larger and eventually the convective cells mess up the magnetic field lines. This is coherent with the further drop of magnetic field strength at even lower temperatures.

We could also mention other possibilities that could account for the magnetic field in white dwarfs like the crystallization of its core (Isern et al., 2017) and the interaction with orbiting planets (Schreiber et al., 2021). The first effect will be further studied in this work, but we have yet no evidence to believe that the later effect is statistically significant to the complete sample.

3 Data

As mentioned in the previous sections, to better understand the nature of the magnetic fields in white dwarfs, it's crucial to have a sample large enough to allow statistical studies of its distribution and its relation to other physical quantities. As a result of this, we need a large sample of spectra from which derive the magnetic field. This was made possible by the advent of surveys that mapped the sky such as Sloan Digital Sky Survey(SDSS) (Ahumada et al., 2020). SDSS has taken spectra for more than three million astronomical objects among which more than thirty thousand have been identified by Kepler et al. (2021) as white dwarfs rich in hydrogen, our group of interest.

Despite the possibility of using the spectroscopic data to determine other physical parameters such as mass and temperature, we chose not to do so. There is a possibility that the magnetic field could introduce systematic error as its effect over the spectral lines is not taken into account by the models that derive these quantities from the spectra. In stars with several components at the atmosphere, it may be possible to choose lines of certain elements that are less sensitive to the magnetic field, but this cannot be done with DAs, since they have the spectra dominated only by hydrogen lines, strongly affected by the magnetic field. Instead, we opted for the parameters acquired based on precise astrometry from GAIA by Gentile Fusillo et al. (2021).

GAIA is a space observatory of the European Space Agency (ESA) that measures the positions of stars with unprecedented precision and aims to observe the whole sky (Gaia Collaboration et al., 2016). With this measurements it can be derived their distances, and proper motions. Gentile Fusillo et al. (2021) calculated stellar parameters (effective temperature, surface gravity, and mass) by fitting Gaia astrometry and photometry with synthetic pure-H, pure-He, and mixed H-He white dwarf atmospheric models.

Besides magnetic field, effective temperature, and mass we also want to study the rotational period of the stars of our sample. To do so we needed photometric data. We use data from TESS, an all-sky survey mission that searches for exoplanets around nearby bright stars (Ricker et al., 2015).

4 Stellar properties

4.1 Magnetic Field

When we study spectra in search of magnetic field information, we are investigating the net effect caused by the field in all points of the visible stellar atmosphere. It is important to note that the magnetic field is not constant for a given radius and can have simple geometries or a more complex one.

The computational routines used in this work were developed by Külebi et al. (2009) as a modified version of a code developed by Euchner et al. (2002) called Yet Another White dwarf Program (YAWP). It accounts for magnetic field geometry by multipolar expansions of the field topology over the visible stellar hemisphere on the basis of spherical harmonics. YAWP adds up appropriately weighted model spectra for a large number of surface elements and then evaluates the goodness of fit to the observed spectra with a least-squares quality function.

Based on synthetic atmospheric models described in Koester (2010), Külebi et al. (2009) pre-computed a grid of models with $\log\ g = 8$, effective temperatures ranging between 7 000 K and 50 000 K in 14 steps, magnetic field strength ranging between 1 MG and 1 200 MG in 1 200 steps, and 17 different directions relative to the line of sight (9 entries, equally spaced in $\cos\psi$). It is noteworthy that YAWP fits only the lines, not the continuum. The plot is multiplied by the continuum used in the normalization. The strength of the lines is affected by the continuum and the limited effective temperature and $\log g$ grid.

We emphasize that YAWP uses a radiative transfer code for magnetized white dwarf atmospheres developed by Jordan (1992) which considers Balmer lines from $n = 3$ to $n = 7$. These are not the only lines modeled in the literature, and an upgrade could be made by adopting lines up to $n = 15$ presented by Schimeczek, and Wunner (2014). For fields larger than around 30 MG, the $n > 7$ lines do affect the optical spectra.

As mentioned earlier, the Zeeman effect is not the only one affecting the absorption line profile, and the Stark broadening must also be considered. However, the presence of both magnetic and electric fields is not well understood for arbitrary strengths and angles between the two fields. Consequently, the low-field regime $\leq$ 5 MG, where the Stark effect dominates, has high and unavoidable systematic uncertainties by the treatment of the stark effect with a crude approximation as presented by Jordan (1992).

4.1.1 Magnetic Field Geometry

Independently of the complexity of the field geometry, it is always possible to represent it as a sum of spherical harmonics, but to utilize all the terms of this sum is not computationally viable (Külebi, 2010). One could start by assuming the simplest model and looking for systems that are not well described. The simplest magnetic field geometry is a centered dipole.

From classical electrodynamics, it is widely known that the magnetic field generated by a dipole is given by

$$\boldsymbol{B}(\boldsymbol{r}) = \frac{\mu}{4\pi}\frac{3(\boldsymbol{m}\cdot\hat{\boldsymbol{r}})\hat{\boldsymbol{r}} - \boldsymbol{m}}{r^3},$$

where $\boldsymbol{m}$ is the magnetic dipole moment centered at the origin of the system.

Carefully choosing the magnetic moment aligned with $\hat{\boldsymbol{z}} = \cos\theta\hat{\boldsymbol{r}} - \sin\theta\hat{\boldsymbol{\theta}}$ we can write the field components in spherical coordinates as

$$\boldsymbol{B}(r,\theta) = \frac{\mu_0 m}{4\pi r^3}(2\cos\theta\hat{\boldsymbol{r}} + \sin\theta\hat{\boldsymbol{\theta}}).$$

On the pole, where $\theta = 0$ and at a unitary radius we have

$$B_p = \frac{\mu_0 m}{2\pi}.$$

We can rewrite the magnetic field in Cartesian coordinates as

$$\begin{aligned}\boldsymbol{B}(x,y,z) = \frac{\mu_0 m}{4\pi r^3}[&2\cos\theta(\sin\theta\cos\phi\hat{\boldsymbol{x}} + \sin\theta\sin\phi\hat{\boldsymbol{y}} + \cos\theta\hat{\boldsymbol{z}}) + \\ &\sin\theta(\cos\theta\cos\phi\hat{\boldsymbol{x}} + \cos\theta\sin\phi\hat{\boldsymbol{y}} - \sin\theta\hat{\boldsymbol{z}})].\end{aligned}$$

Or, in terms of the components as

$$\begin{aligned}B_x &= \frac{\mu_0 m}{4\pi r^3}\frac{3xz}{r^2} = \frac{B_p 3xz}{2r^5},\\ B_y &= \frac{\mu_0 m}{4\pi r^3}\frac{3yz}{r^2} = \frac{B_p 3yz}{2r^5},\\ B_z &= \frac{\mu_0 m(3z^2 - r^2)}{4\pi r^5} = \frac{B_p(3z^2 - r^2)}{2r^5}.\end{aligned}$$

When we compute the modulus of the magnetic field at any point in space we have

$$\begin{aligned}B(x,y,z) =& \sqrt{B_x^2 + B_y^2 + B_z^2} = \frac{3B_p z}{2r^5}\sqrt{x^2 + y^2 + \frac{(3z^2 - r^2)^2}{9z^2}}\\ =& \frac{3B_p z}{2r^5}\sqrt{x^2 + y^2 + \frac{(9z^4 - 6z^2r^2 + r^4)}{9z^2}}\\ =& \frac{3B_p z}{2r^5}\sqrt{x^2 + y^2 + z^2 - \frac{2r^2}{3} + \frac{r^4}{9z^2}} = \frac{3B_p z}{2r^4}\sqrt{\frac{1}{3} + \frac{r^2}{9z^2}},\end{aligned}$$

in which there is a clear symmetry of rotation along the z-axis once the modulus does not depend on x or y. In addition to this, there is another symmetry around the plan xy at $z = 0$ that can be seen in the black line in Fig. 4.

Unfortunately, there are several stars for which a centered dipole does not explain the profiles of the spectral lines. This is the case for the white dwarf SDSSJ113839.49-014903.0, P-M-F = 3775-55207-0698 whose spectra is shown in Fig. 5.

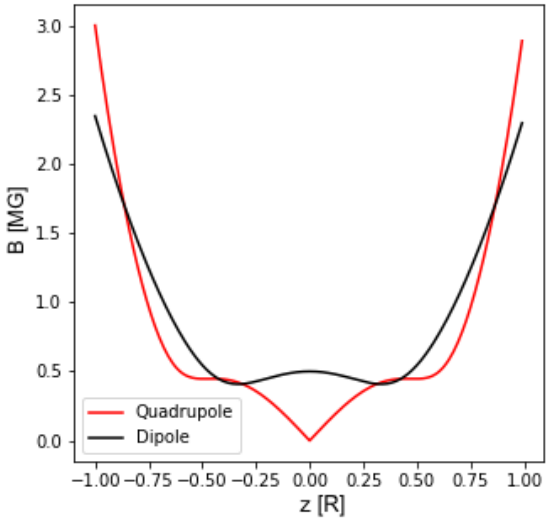

Figure 4 – Distribution of magnetic field modulus as a function of z for a centered dipole in black and a centered quadrupole in red.

One could then consider the next term of the sum, represented by quadrupole geometry, but the problem would persist since a centered quadrupole has the same symmetry as it is shown by the red line in Fig. 4 . Instead of adding more complex centered terms, it is possible to consider simply an offset of the center of the dipole in relation to the center of the star (Achilleos; Wickramasinghe, 1989).

It can be easily seen that to apply a displacement on the dipole is equivalent to rewrite $\boldsymbol{r} \to \boldsymbol{r} - \boldsymbol{r'}$ which implies

$$\boldsymbol{B}(\boldsymbol{r}, \boldsymbol{r'}) = \frac{\mu}{4\pi}\left[\frac{3\boldsymbol{m}(\boldsymbol{r'})\cdot(\boldsymbol{r}-\boldsymbol{r'})}{|\boldsymbol{r}-\boldsymbol{r'}|^5}(\boldsymbol{r}-\boldsymbol{r'}) - \frac{\boldsymbol{m}(\boldsymbol{r'})}{|\boldsymbol{r}-\boldsymbol{r'}|^3}\right].$$

This allows much more complex distributions, the poles may have very different magnetic fields for example, with the inclusion of only one parameter (the offset). A representation of an offset dipole distribution is presented in Fig.6. However, the fit for the observed spectra is still inappropriate as it can be seen with the offset of -0.2 $R_\star$ presented in Fig. 7.

In this context, it is relevant to consider that the stars more commonly are not with their rotation axis perpendicular to our line of sight, making it necessary to consider

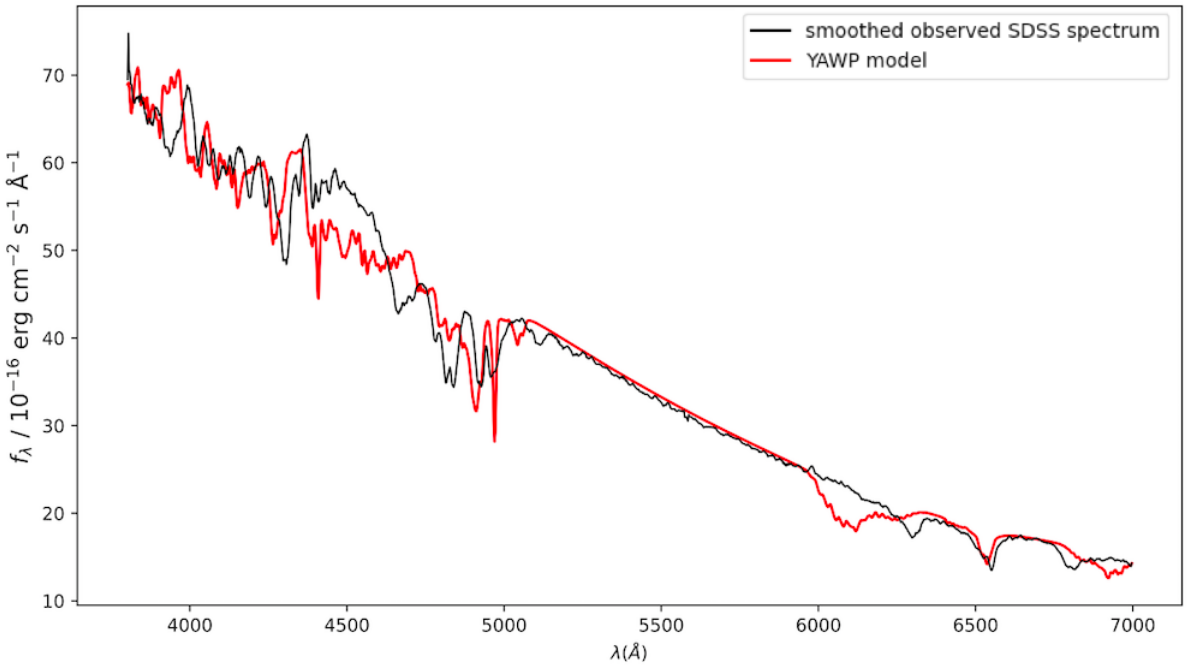

Figure 5 – Observed SDSS spectrum of the star SDSSJ113839.49-014903.0 in black and YAWP model in red considering a centered dipole. The central line of $H_\alpha = 6\,564.6$ Å is well modeled, but the σ lines are misrepresented. The χ^2 for this model is 2.38.

its inclination. With this one more parameter considered, the model fits almost all features of the spectra, as shown in Fig. 8 so we decided to compute all magnetic fields with offset dipole geometry.

4.2 Variability

There are several reasons why the brightness we measure of a star can vary. They can be related to some physical changes at the star itself, of its environment, or the circumstances of its measurement. The stellar brightness can vary due to pulsations, dark spots, hot spots, thermal pulses, and others. Moreover, even when the stellar luminosity is constant, we can measure a varying magnitude if a body occludes our line of sight such as orbiting planets, comets, or even a companion star in cases of binary systems.

The information we have to try to distinguish between different types of variability is the timescale in which they occur. As we are interested in finding the rotational period of the stars in our sample we focus on periods of some hours or days. For this purpose, a cadence data of 30 minutes is suitable since it won't display quick variations coming from pulsations. However, this creates a bias against fast rotators that may be overlooked. Additionally, some close binary systems can also fit the range of periods considered.

Independently of the source of variation, we are interested in finding the periods, or equivalently the frequencies, of these fluctuations. A traditional technique used in cases

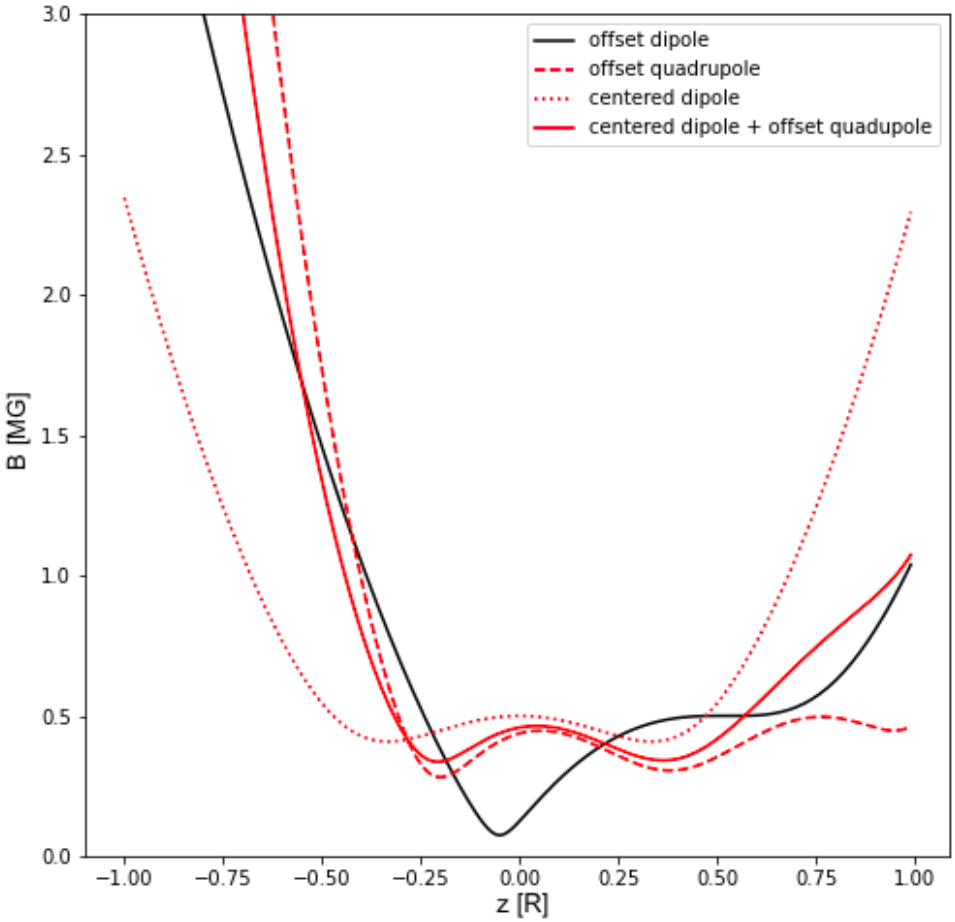

Figure 6 – Distribution of magnetic field modulus as a function of z for a centered dipole as a red dotted line, for an offset quadrupole as a red dashed line, the sum of them both as full red line compared to an offset dipole as a black line. Both offsets are of 0.5 $R_\star$.

like this, and adopted in this work, is the Fourier Transform of the temporal photometric data (light curves). This approach is based on the fact that any periodic function can be written as an infinite sum of sinusoids with different weights, but we are interested only in the dominant behavior.

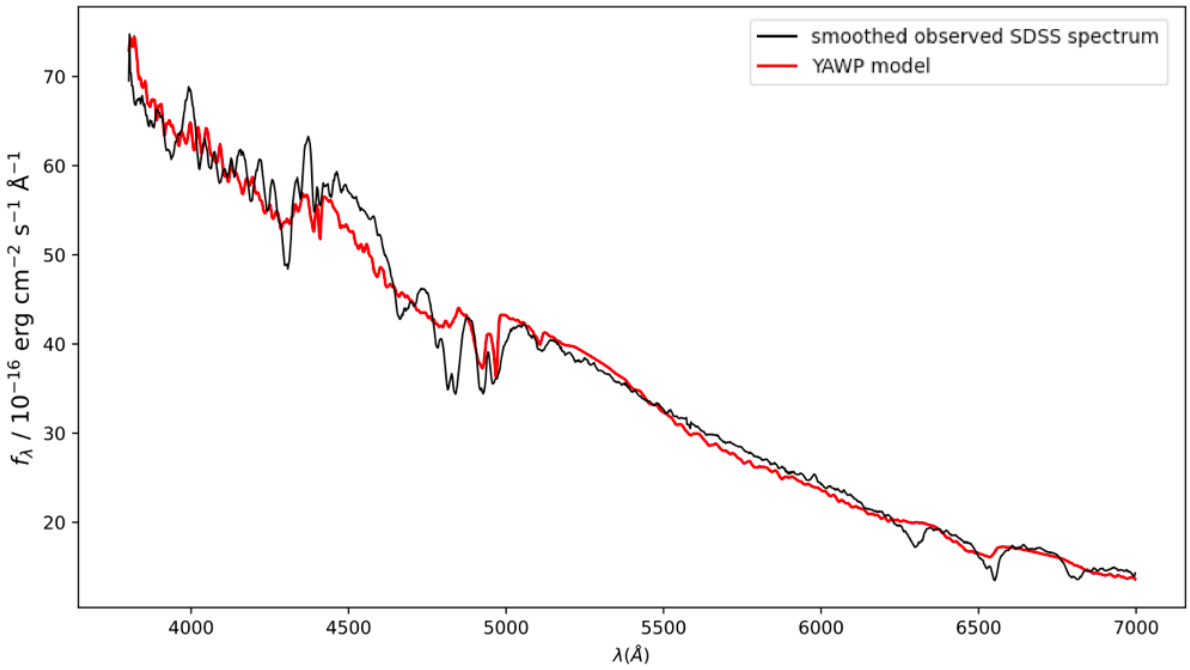

Figure 7 – Observed SDSS spectrum of the star SDSSJ113839.49-014903.0 in black and YAWP model in red considering a dipole with an offset of -0.2 R$_\star$. A better model when compared to the centered dipole model, which is confirmed by the smaller $\chi^2 = 1.40$, but the lines are yet not well modeled.

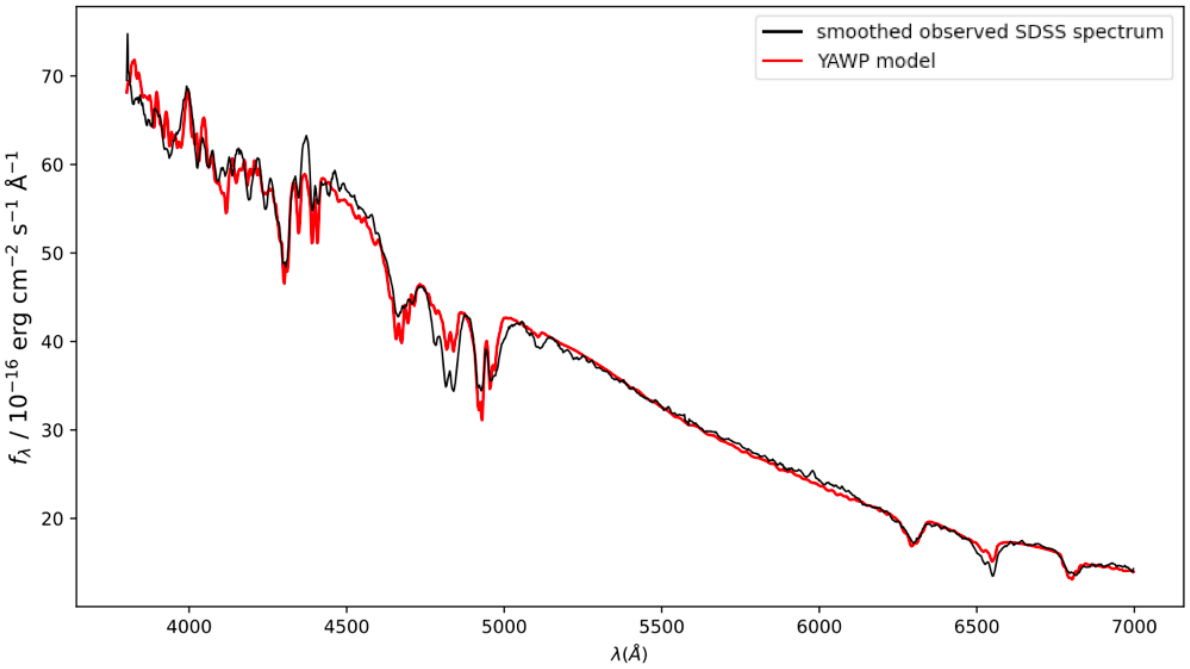

Figure 8 – Observed SDSS spectrum of the star SDSSJ113839.49-014903.0 in black and YAWP model in red considering a dipole with the same offset of -0.2 R$_\star$ and an inclination of 55°. The $\chi^2 = 0.547948$ is the smallest when compared to the previous models and the lines are well modeled, both H_α = 6 564.6 Å and H_β = 4 861.35 Å.

5 Results

5.1 Detection of magnetic fields in SDSS DR16 white dwarfs

To build our sample, we visually investigated all DA spectra up to DR16 in search of Zeeman splitting and concatenated the selected ones with the previously known until DR7, resulting in 803 stars. Then we used the code presented by Külebi et al. (2009) to determine the strength of the magnetic fields. A part of our sample can be seen in Table 1, and Figure 9 presents three white dwarfs with magnetic fields of different orders of magnitude that represent them. A complete table is presented in Appendix C.

Table 1 – The table presents effective temperatures estimated with non-magnetic models used as a fixed input for YAWP and the effective temperature calculated with GAIA astrometry. Although in some cases they differ a lot, this does not strongly affect the magnetic field estimation since the temperature affect mostly the depth of the line and not its position, which is dominant in the estimation of the magnetic field. In addition to the results from the spectroscopic analysis, the last but one column presents the period of highest amplitude from TESS photometry. And finally, the magnetic field modulus resulted from the best YAWP model for each star.

PMF	TIC	T_{eff} YAWP (K)	T_{eff} GAIA (K)	P(h)	B (MG)
0366-52017-0591	1400842448	11500	15000	164.56	25.60
0367-51997-0318	1271054357	30000	30000	181.16	64.50
0367-51997-0461	1400761333	15000	25000	157.21	25.00
0406-51900-0490	630263660	9500	9500	352.35	21.60
0406-52238-0071	630251962	16500	16500	196.93	13.00
0413-51929-0313	649786561	30000	30000	210.40	148.40
0415-51879-0485	453828065	9500	9500	111.83	717.10
0416-51811-0590	649819568	8000	9500	208.28	25.00
0419-51879-0147	611261863	8000	9000	61.17	30.00
0437-51869-0369	141117787	9000	11000	6.71	453.80
0453-51915-0325	841143629	12000	18500	86.82	20.40
0459-51924-0002	651936432	9500	13500	259.49	13.00
0475-51965-0315	842119542	10500	14000	102.80	30.20
0476-52314-0597	842095343	24000	24000	182.39	2.58
0480-51989-0082	842138864	9000	16500	51.61	22.90
0480-51989-0251	842141925	9500	13000	149.87	20.10
0483-51902-0296	802265153	15000	15000	170.00	24.70
0483-51924-0203	802348105	10000	10000	165.53	10.00
0489-51930-0079	900616508	18000	18000	175.62	195.00
0489-51930-0535	900624504	9500	12500	217.00	22.20
0490-51929-0205	900618725	18000	23000	1837.74	100.00
0501-52235-0077	842039397	40000	30000	70.43	38.50
0547-52207-0019	801914894	22000	22000	118.68	20.20
0556-51991-0326	841061440	9000	_	188.97	2.26

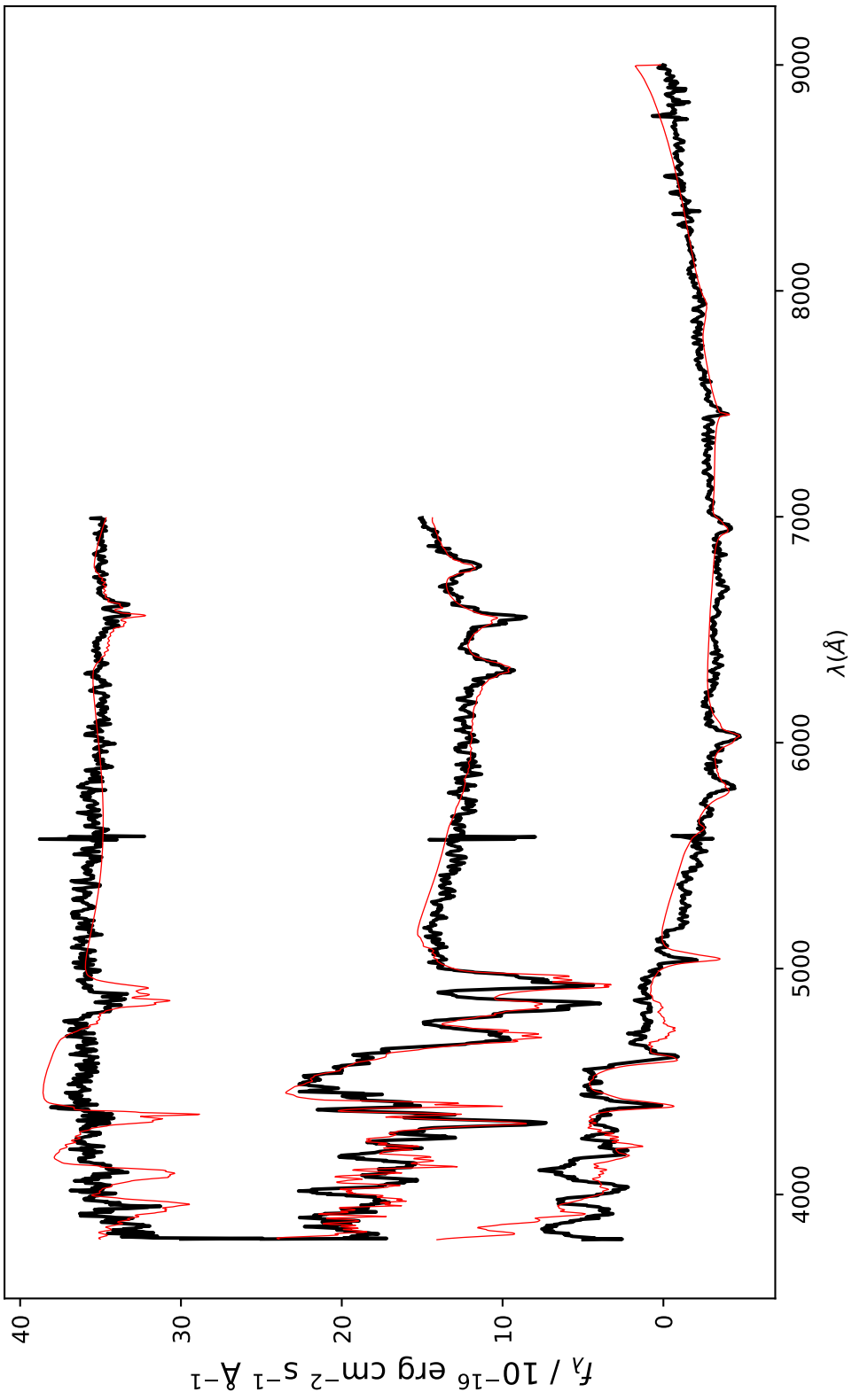

Figure 9 – SDSS spectrum of three of the stars we computed the magnetic field. The model with the best least-squares fit to the observed data is showed in red. From top to bottom we have (a) Plate-MJD-Fibre = 1237-52762-0533, B = 2.51 MG, S/N = 12 and $T_{\rm eff}$ = 8 000 K; (b) Plate-MJD-Fibre = 0733-52207-0522, B = 20.71 MG, S/N = 20 and $T_{\rm eff}$ = 10 000 K; (c) Plate-MJD-Fibre = 5445-55987-0530, B = 202.58 MG, S/N = 11 and $T_{\rm eff}$ = 16 500 K. We corrected linearly the inclination of the spectra and attributed an arbitrary shift in flux for a better visualization. Recall that H_α = 6 564.6 Å and H_β = 4 861.35 Å.

As already discussed, the magnetic field affects the line profiles, and we cannot use them to estimate surface gravity directly. Thereby, the models used in the code are calculated with $\log g = 8$ for all the stars as an approximation. This value was originally chosen considering that it is the mean value for white dwarfs. It has been acknowledged that it is not the best value to represent magnetic white dwarfs once they are found to be more massive than the non-magnetic ones. Unfortunately, these are the best models that we have access to, constituting a very interesting way in which our work could be further improved in the future.

The code also presents the possibility of searching for the temperature spectroscopically, together with the magnetic field parameters. But, due to the uncertainties, we opted to use a previously estimated temperature acquired by comparing the observed fluxes with hydrogen-rich atmospheric models. These models lead to a table of colors in the bands u, g, r, and i used by SDSS for each temperature. One can compare this values, specially their differences (color index), to the values from the observed spectra thus obtaining an estimated temperature. We chose not to use the i-band since it is observed a lot of noise in the corresponding wavelengths.

Although the original range of temperatures varied from 6 000 K to 50 000 K, we only used temperatures between 8 000 K and 40 000 K when varying the magnetic field due to convergence problems. This limits our capacity to model the magnetic field of stars outside this range of temperature, as the models present deeper lines than those observed in the SDSS spectra. The depth of the absorption lines however doesn't have a big impact on the determination of the magnetic field amplitudes which are predominantly determined by the wavelength displacement and presence of splits.

This effect can be seen on the upper part of Figure 9, in which a WD with a temperature below 8 000 K is presented. The best model, in red, clearly has lines deeper than the observed spectra but well represents the splitting on the $H_\alpha = 6\,565$ Å and $H_\beta = 4\,861$ Å lines.

As the original data has many points and usually are noisy, we present them after the application of a smooth function. Besides, the noise in the observed spectra is dependent on the wavelength and is significantly higher above 7 000 Å. It is noticeable that the absorption lines of hydrogen don't spread to these high wavelengths in field regimes below 25 MG ($\log B \approx 1.4$), as visible in Figure 11 from Schimeczek, and Wunner (2014). Thereby, we do not consider higher wavelengths in spectra of DAH with lower fields to minimize the noise effect, which can be seen on the first two panels of Figure 9.

For some stars, YAWP did not find any plausible solution within reasonable computing time (hours), and we resorted to a simpler visual analysis to estimate the magnetic field, used it as a fixed input to the code, and allowed only the inclination and the offset to vary. Some illustrative examples of the visual inspection can be seen in Fig. 10. The

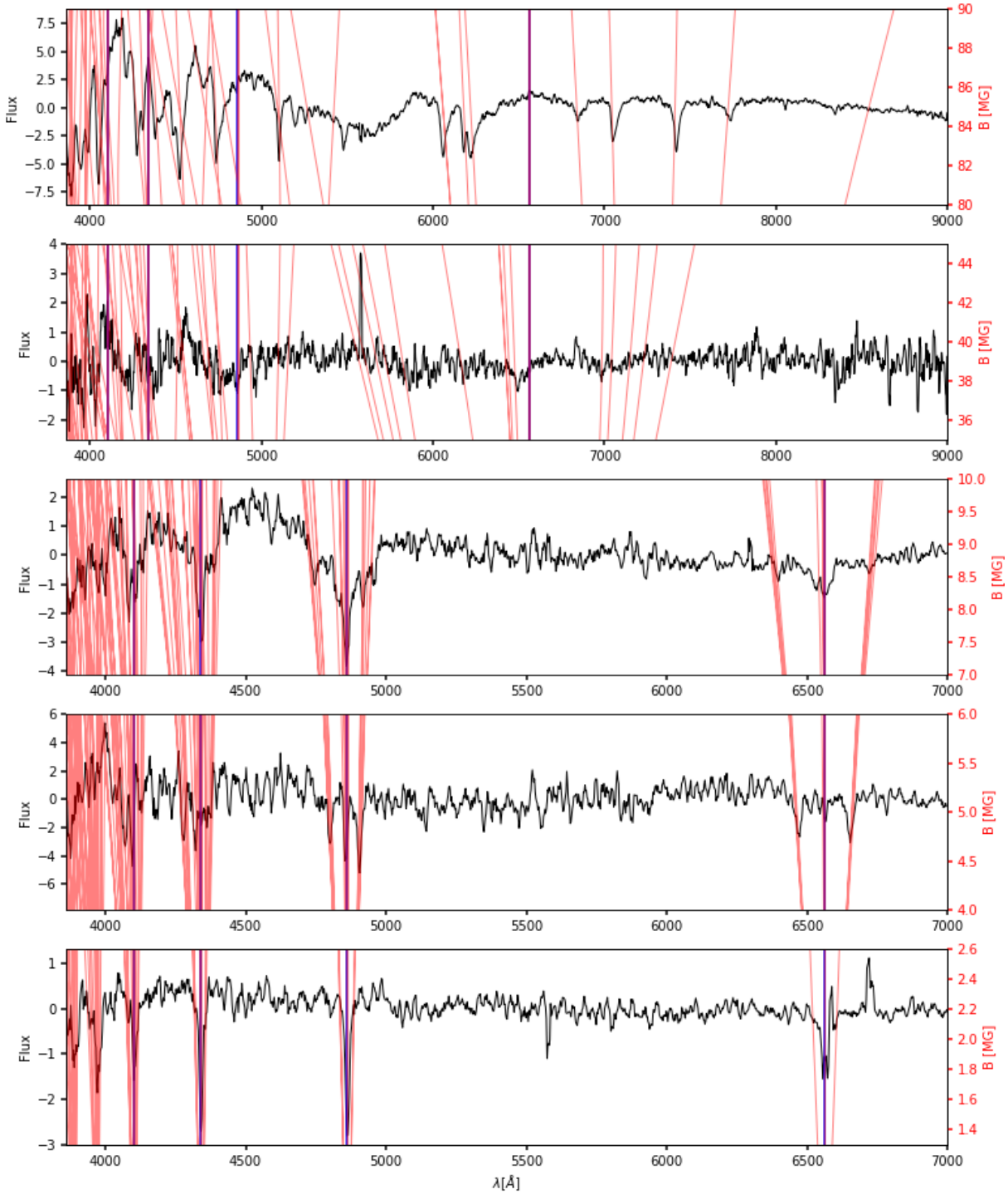

Figure 10 – Spectra of MWDs after applying the smooth function and normalizing by a third-degree polynomial function for better display. From top to bottom we have MWDs with Plate-MJD-Fibre 5179-55957-0778, 0545-52202-0009, 0690-52261-0594, 1311-52765-0421, 3183-54833-0179, and magnetic field equal to 85, 38, 8.5, 5, 2 MG respectively. The flux is f_λ / 10^{-16} $erg\ cm^{-2}\ s^{-1}$ Å^{-1}. The red lines represent the magnetic field strength as a function of the wavelength as computed by Schimeczek, and Wunner (2014). The blue vertical lines represent the position of absorption lines for hydrogen when no magnetic field is applied.

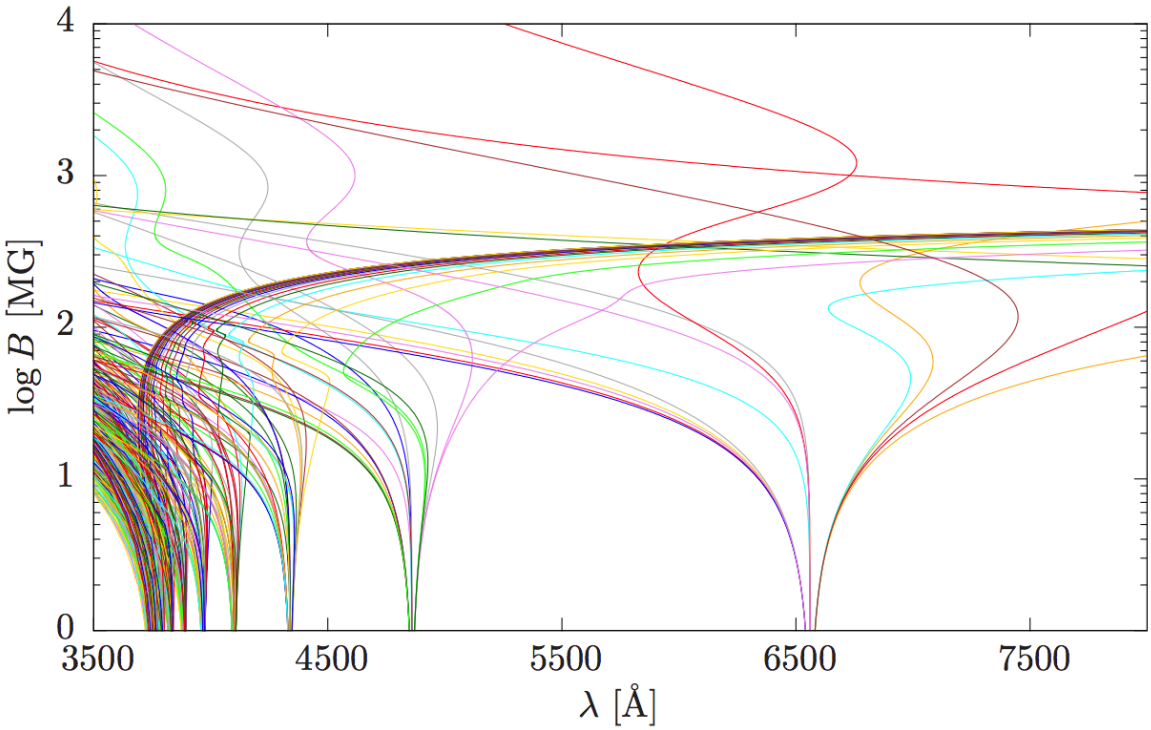

Figure 11 – Magnetic field strength as a function of the wavelength of the first 325 transitions in the Balmer series, which emerge from the field-free Balmer transitions up to principal quantum numbers n = 10. Colors were arbitrarily assigned to facilitate visualization.

best model computed with the magnetic field fixed for one of these MWDs is portrayed in Fig. 12. The visual estimation was also used for stars with magnetic fields below 1 MG, but not used as input since it is below the threshold of the first method. An example can be seen in Fig. 13.

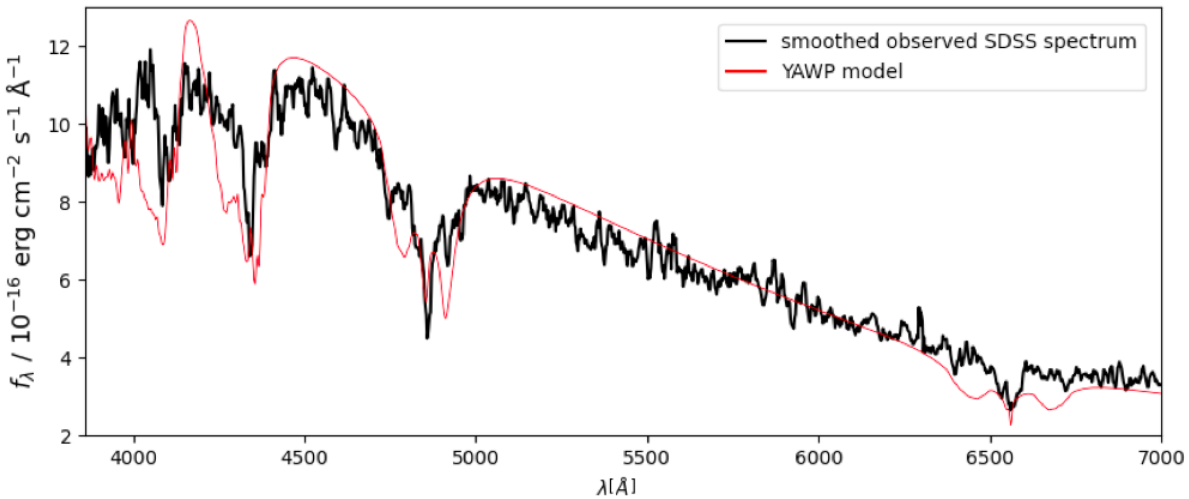

Figure 12 – SDSS spectrum of the star with Plate-MJD-Fibre = 0690-52261-0594, B = 8.5 MG, S/N = 7.5 and T_{eff} = 14 000 K is presented in black. The model with the best least-squares fit to the observed data with B = 8.5 MG is shown in red.

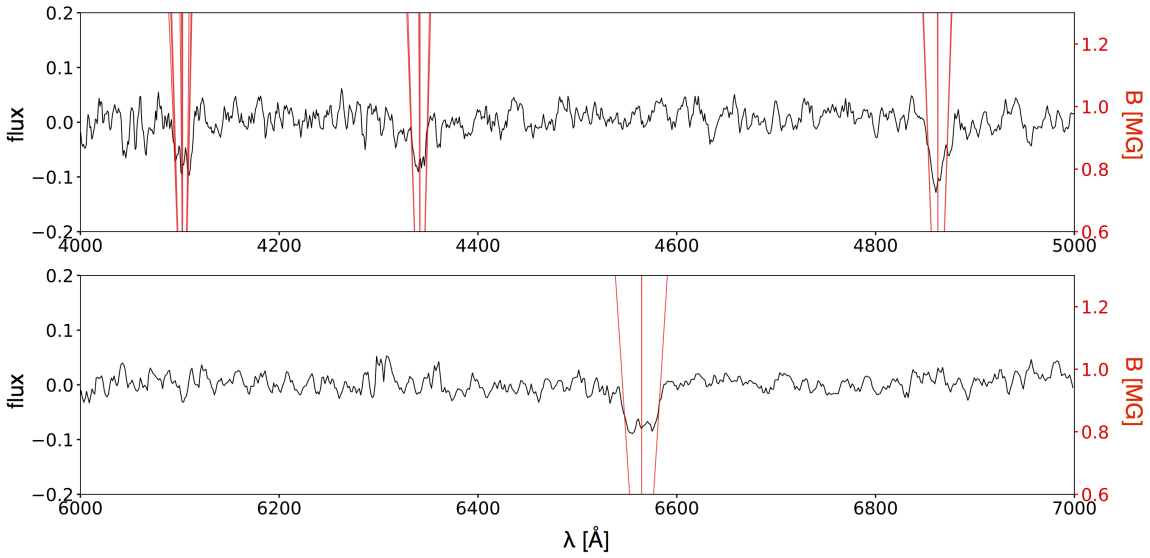

Figure 13 – Spectra of the star with Plate-MJD-Fibre = 4868-55895-0730 after applying the smooth function and normalizing by a third-degree polynomial function for better display. The flux is f_λ / 10^{-16} $erg\ cm^{-2}\ s^{-1}$ Å^{-1}. The red lines represent the magnetic field strength as a function of the wavelength as computed by Schimeczek, and Wunner (2014).

The only geometry of magnetic field considered to our determinations was the non-centered dipole, which is a good approximation for these objects. We emphasize that if the offsets are large, the polar field strength is not representative of the global magnetic field on the visible surface. Besides, the field difference between regions of a star can get very high (orders of magnitude) as the polar field increases. This was illustrated in subsection 4.1.1.

This effect can be seen in Fig. 14. The model that best reproduces the observational data has a B = 61.2 MG. However, it can be seen in the second panel that the field over the surface varies between 30 and 110 MG, being more expressive around 30 MG, the value that would be found if the visual inspection was used.

Besides that intrinsic variation, we estimate that our precision cannot be lower than 1 MG since the spectra are not precise enough due to resolution and signal-to-noise ratios. Beyond these limitations, our errors are approximately 12% of the computed value.

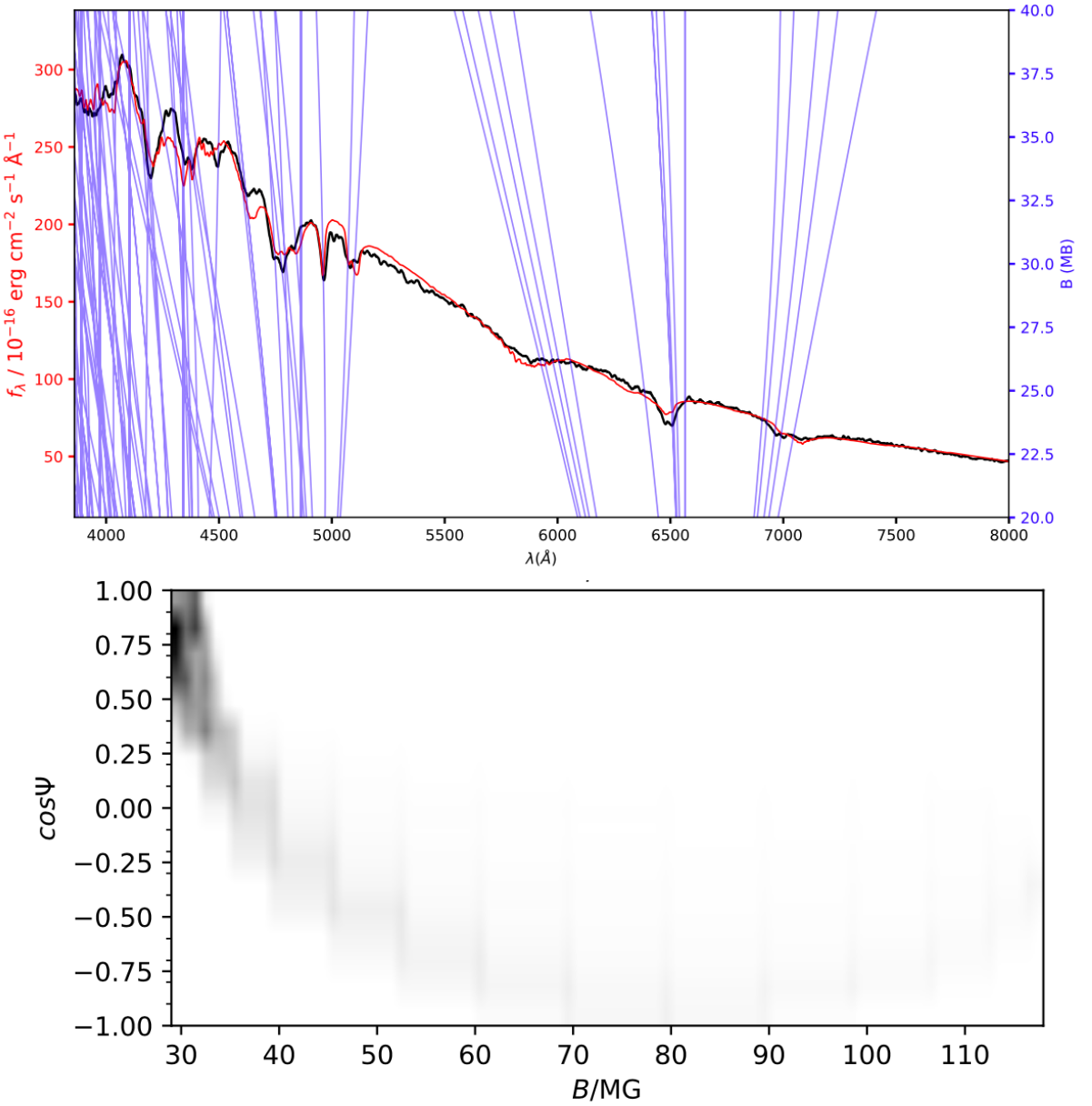

Figure 14 – Top panel showing the SDSS spectrum of the star with Plate-MJD-Fibre = 4568-55600-0952, B = 61.2 MG, S/N = 63 and $T_{\rm eff}$ = 13 500 K is presented in black. The model with the best least-squares fit to the observed data is shown in red. The blue lines represent the magnetic field strength as a function of the wavelength as computed by Schimeczek, and Wunner (2014). Bottom panel showing the distribution of magnetic field over the stellar surface due to the inclination of 29.35° and $z_{\rm offset}$ of -0.38 $R_\star$ delineated by the best model.

5.2 Detection of Periodicity in TESS Full Frame Image

We made a cross-match of the list of DAH with measured magnetic field and the TESS catalog and found correspondence to 785 white dwarfs. However, not all of them have been observed until Sector 46. With the ones already observed, we constructed light curves at 30 minutes cadence (up to sector 39) or 10 minutes cadence (after sector 40) from the TESS full frame images (FFI) using the eleanor pipeline from Feinstein et al. (2019). We extracted postage stamps of height=15, width=15, and a background size=31. We did not use the eleanor features for removing light curve systematics using either the point spread function or principal component analysis options. It is important to consider that in the future TESS will provide 200 seconds cadence for all observed stars, which will improve the possibility to detect high frequency variations.

We computed Fourier transforms (FTs) of the light curves to find periods of variability for all observed stars, concatenating different sectors when available. To minimize systematic errors due to noise in the light curve, we compute a false alarm probability (FAP). We randomly changed the order of the observations, recomputing the FT, and calculating the amplitude at which there is a 0.1%= 1/1 000 probability of any peak being due to noise, as suggested by Kepler (1993). We report the higher amplitude frequency above the 0.1 FAP threshold of 380 stars. A part of our sample can be seen in table 1.

Some of these stars have been already studied before, as it's the case of TIC 141117787 which had a rotational period detected by Brinkworth et al. (2013). They referred to the star as WD0756+437 and found a period of $6.68^{+0.02}_{-0.03}$ h. We found a 6.71 h variability period, which is consistent with their error margin. This star in particular has 2 minutes cadence available and is a good example to demonstrate how the 30 minutes cadence can be useful when the 2 minutes is absent. Fig. 15 and Fig. 16 portray the folded light curve and Fourier transforms for 2 minutes and 30 minutes data respectively. In both cases, the highest peak in frequency is well above the detection limit and the pattern of variability can be easily seen in the folded light curve.

In total, 29 stars in our sample also present 2 minutes cadence, and 2 of them present 20 seconds cadence. Not all of them have a period above the FAP in the fast cadence data and the ones that have aren't all compatible with the first period determination. To be consistent in precision for all sample, we made our analysis only based on the longer cadence. To assure that our results would be coherent we compared the periods determined from different cadences and present them in Appendix A.

We emphasize that the period measured is not necessarily the rotational period. Other possibilities are orbital period in binaries, pulsations, or variability due to multiple spots on the stellar surface. To exemplify this we can look at Fig. 17 where is represented the folded light curve over twice the period of higher amplitude of the star with

TIC800350281. It is easy to see two valleys of different depths most likely indicating the two eclipses of a binary system. This is also noticeable if we analyze its FT in Fig. 18. Since eclipses are not well described by a sinusoidal function, a pattern of harmonic frequencies appears.

We found only two other stars with these binary features, so we expect these contaminants in rotational period to be low. In this cases, there is still a chance that the period detected is indeed the rotational period since spin-orbit synchronization occurs by tidal force $dF \propto M/d^3$, where M is the mass of the companion and d its distance. And according to the third law of Kepler $d^3 \propto P^2$, where P is the orbital period.

Beyond the physical processes that could be generating variability there is a possible systematic origin of detected periods. Each TESS sector is 27 days long, with a pause in observation in the middle, causing a false detection of periods around 160 hours (a quarter of a sector).

Besides the DAH for which we determined a magnetic field, we detected photometric variability in previously known DAHs and DAPs. We present a table of the periods as extra information in Appendix B. It is noteworthy that this analysis was made upon 120 seconds cadences, or 20 seconds, when available, presenting a much lower detection limit than the 30 minutes cadence data.

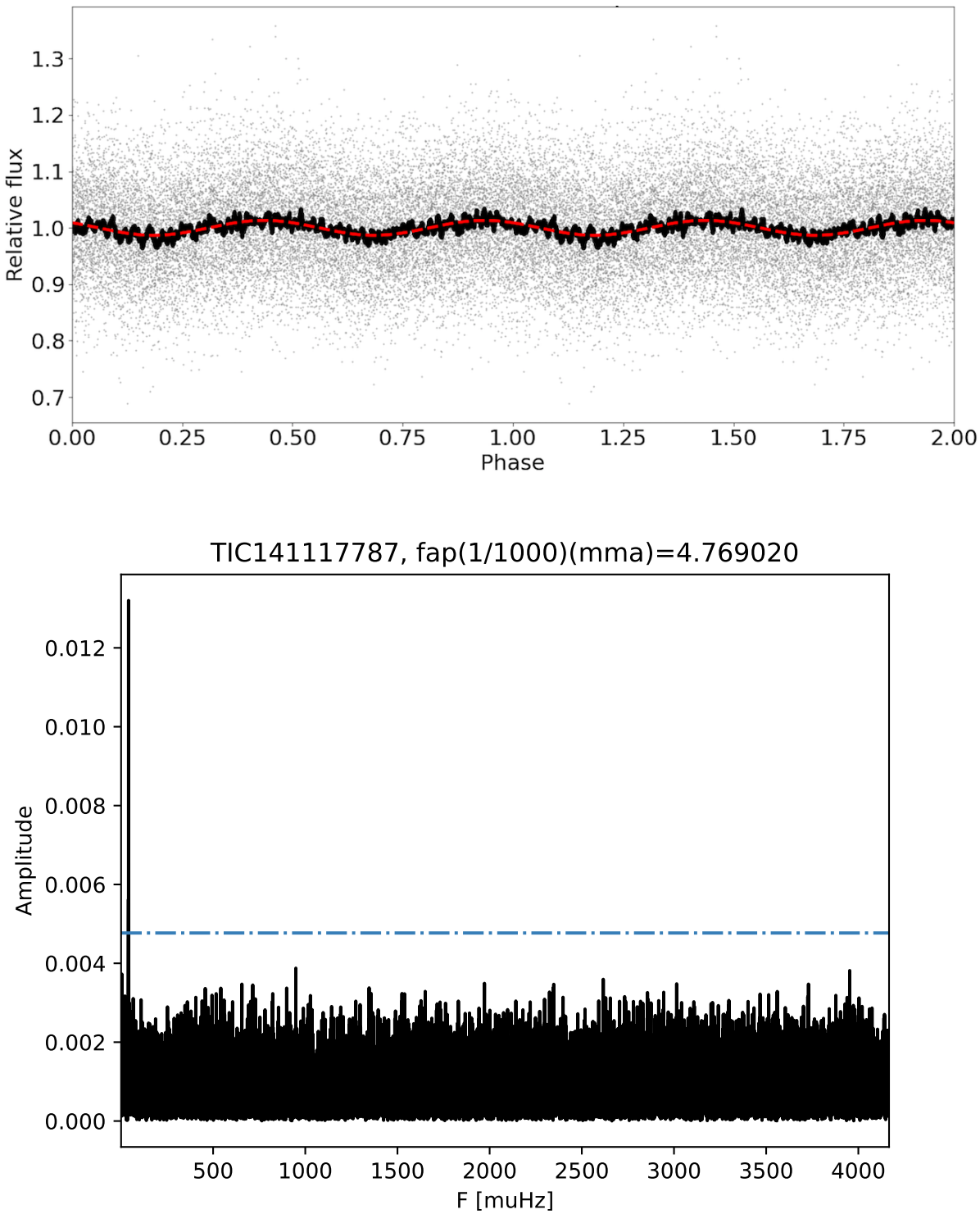

Figure 15 – TESS 2 minutes cadence data of star with TIC 141117787. Top panel showing folded light curve over twice the period of higher amplitude. Bottom panel showing Fourier Transform. The blue line is the False Alarm Probability.

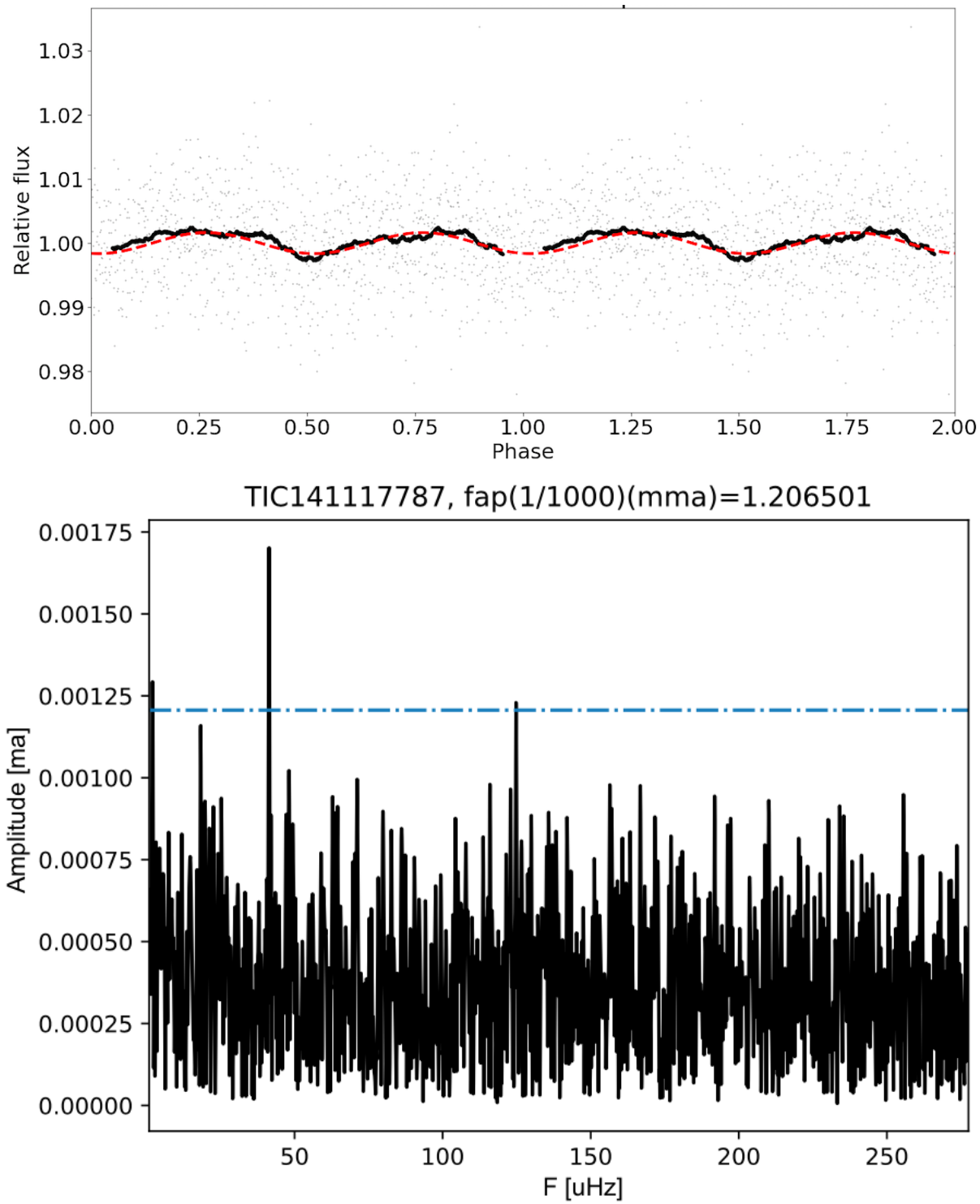

Figure 16 – TESS 30 minutes cadence data of star with TIC 141117787. Top panel showing folded light curve over twice the period of higher amplitude. Bottom panel showing Fourier Transform. The blue line is the False Alarm Probability.

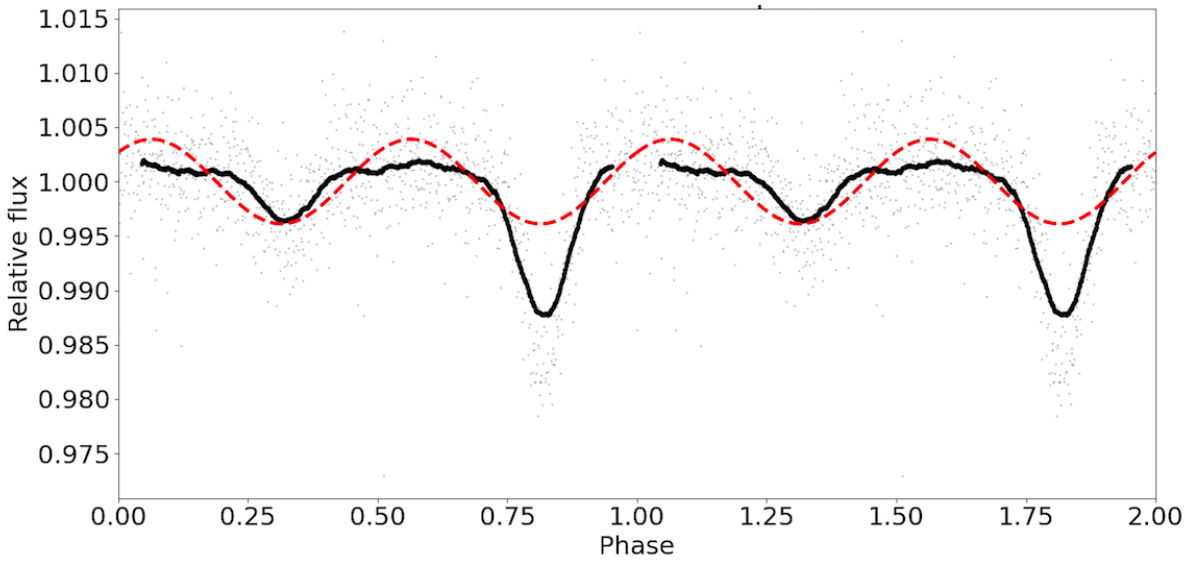

Figure 17 – Folded light curve over twice the period of higher amplitude of the star with TIC 800350281.

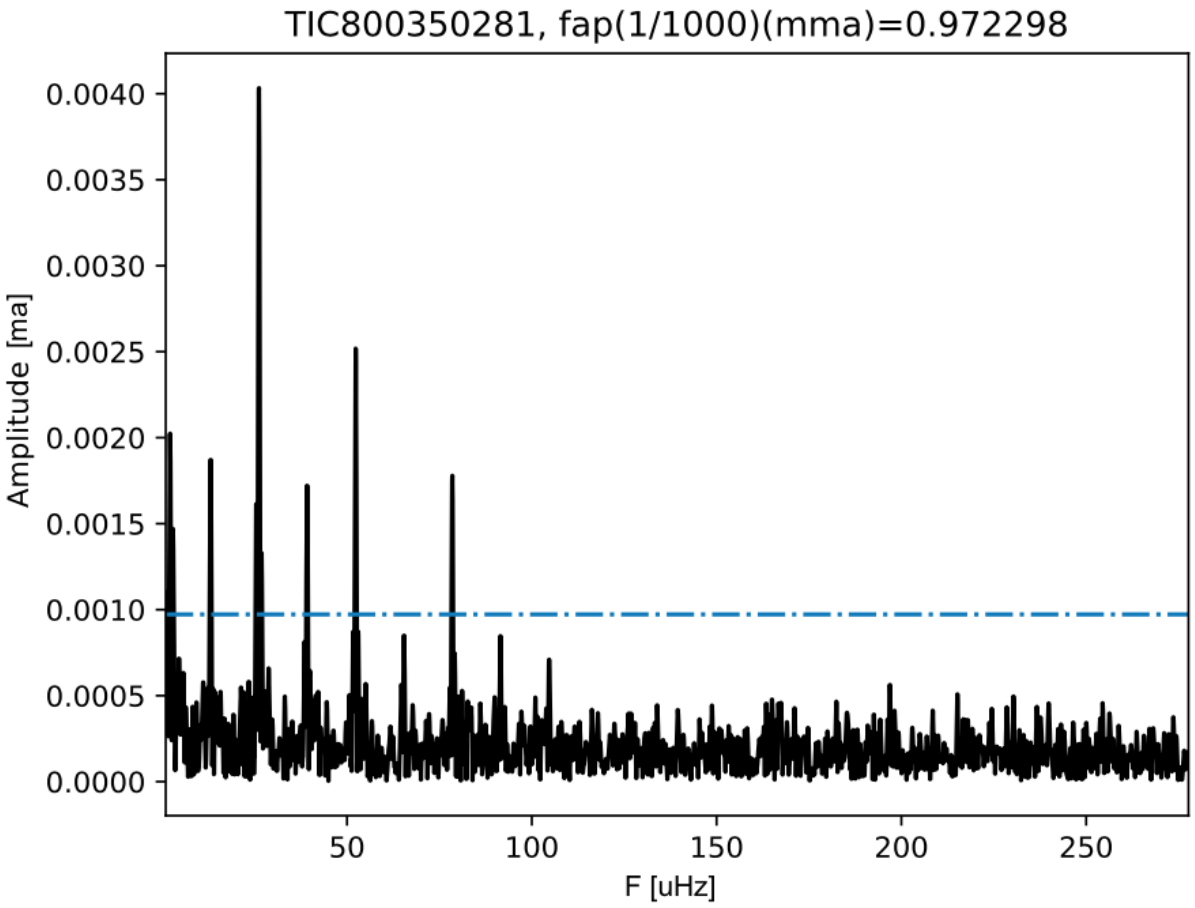

Figure 18 – Fourier transform of the TIC 800350281 light curve, showing several harmonics of the eclipse period.

6 Discussion

Liebert, Bergeron, and Holberg (2003) propose that magnitude limited samples, as the one studied in this work, have a bias against higher mass white dwarfs since for a given temperature they have a smaller radius than those with less mass and consequently a smaller luminosity. This would lead them to be detected less frequently. However, they did not take into consideration that more massive white dwarfs take longer to cool down because they have a smaller radius and start cooling at higher temperatures.

Since it is not straightforward which of these effects predominate at a given time, we present Fig. 19 extracted from Bagnulo, and Landstreet (2021). It is clear that magnitude limited samples have a complex bias against or in favor of higher masses depending on the stellar age. One can more rightly conclude that there is a bias in favor of younger stars independently of their mass.

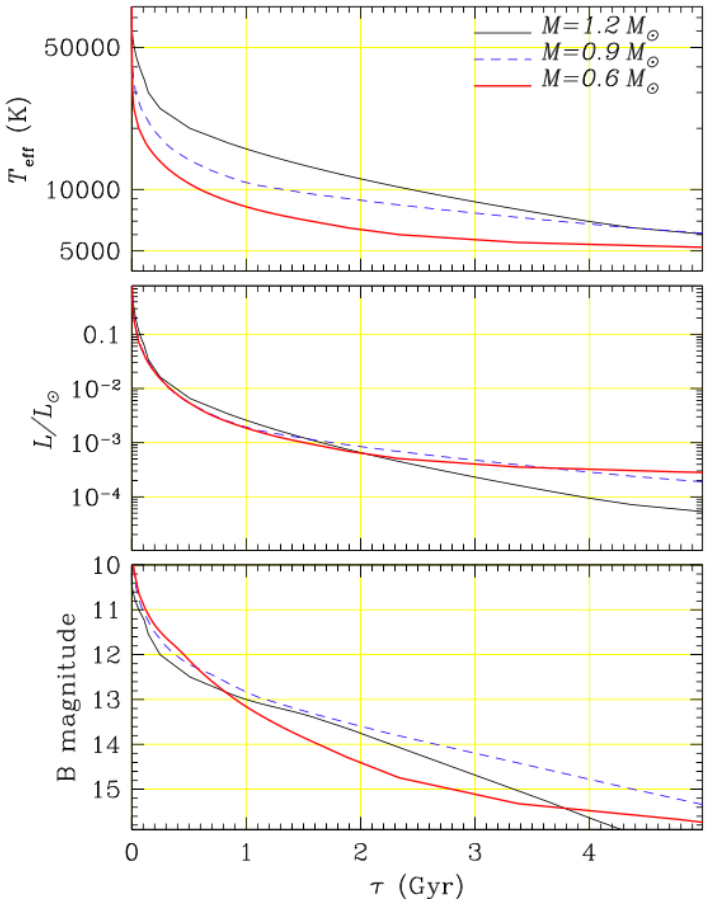

Figure 19 – Cooling history of 1.2 $M_\odot$(black solid lines), 0.9 $M_\odot$(blue dotted lines), and 0.6 $M_\odot$(tick red solid lines) WDs. Top panel: T_{eff} versus cooling age τ; mid-panel: luminosity versus cooling age; bottom panel: Johnson B absolute magnitude versus cooling age. Data from Montreal cooling curve database.

Bagnulo, and Landstreet (2021) found also that the frequency of magnetic white dwarfs is substantially depressed in stars younger than 0.5 Gyr and that this difference probably reflects the action of the mechanisms that produce magnetic fields in white dwarfs.

Even though it favors younger stars, magnitude limited surveys especially with low-resolution spectroscopy are the ones that can go deeper in magnitude and examine a larger sample of stars. With this in perspective, we will discuss the distribution of magnetic field strength, the relation between magnetic field and mass, effective temperature and period, and some specific cases that stand out in our sample.

6.1 Distribution of magnetic field strength

The fraction of magnetic white dwarfs rich in hydrogen found in this work was 2.7%. A number far below the previous values presented in the literature. We call attention to the strong bias present in our sample due to the chosen survey. The choice of which stars are going to be observed by SDSS has changed over time, resulting in a smaller number of magnetic white dwarfs in the latest data releases because white dwarfs in general were not targeted.

We also note that the visual identification of Zeeman splittings is much more efficient for magnetic fields below 60 MG when the effect is well behaved as can be noticed in Fig. 11. With these reservations, we present the distribution of the magnetic field strength of our sample in Fig. 20. A higher appearance of magnetic fields of strength below 3 MG is noticeable.

As was mentioned in Section 1, the HR-Diagram is a fundamental tool to the study of stellar evolution. Thus, we looked into the HRD with magnetic field amplitudes in search of evidence of magnetic field interference in its star host. The HRD of our sample in the form of CMD (Color-Magnitude Diagram) can be seen in Fig. 21, and it is distinguishable that the more massive ($M_G \gtrsim 12$) white dwarfs display higher fields. This could be a reflection of the fact that the mean mass of the DAH is significantly higher than the non-magnetic ones or perhaps another effect is happening. We investigate it further in the next section. Although it is not clear a relationship between effective temperature and magnetic field in Fig. 21 due to the density of points, we dive deeper into this analysis in section 6.3.

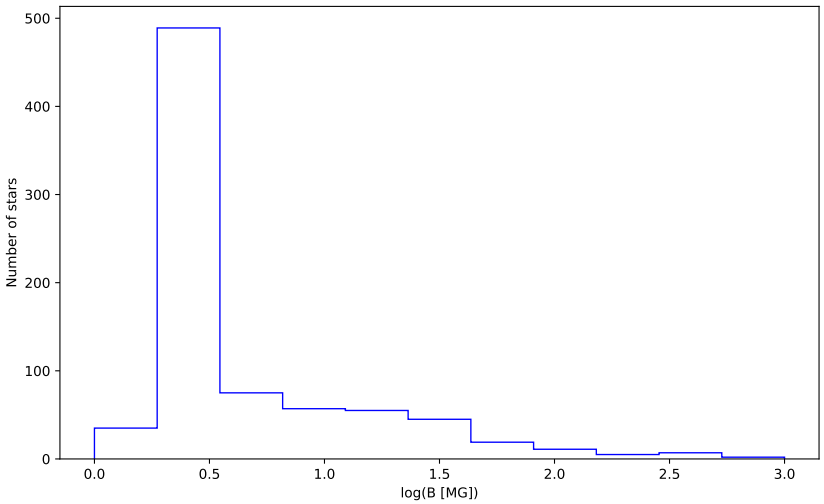

Figure 20 – Magnetic field strength histogram for all magnetic white dwarf in our sample.

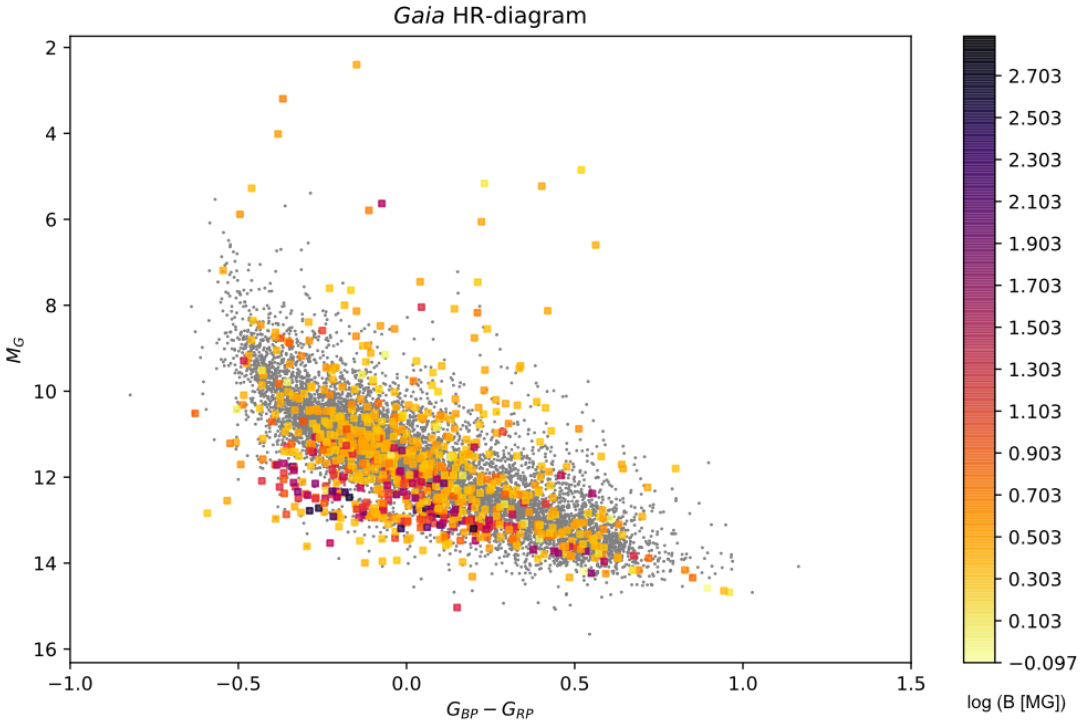

Figure 21 – HR Diagram with data from GAIA for white dwarfs rich in hydrogen. Grey points represent DAs without a detected magnetic field and other colors indicate the logarithm of the magnetic field strength in MG. It is evident the accumulation of higher magnetic fields at the more massive region of the diagram.

6.2 Relation between mass and magnetic field

To further examine the possible relation between magnetic field and mass, we made Fig. 22 to study the number of stars with magnetic fields and Fig. 23 to study the connection between the absolute magnitude of the magnetic field and the star's mass.

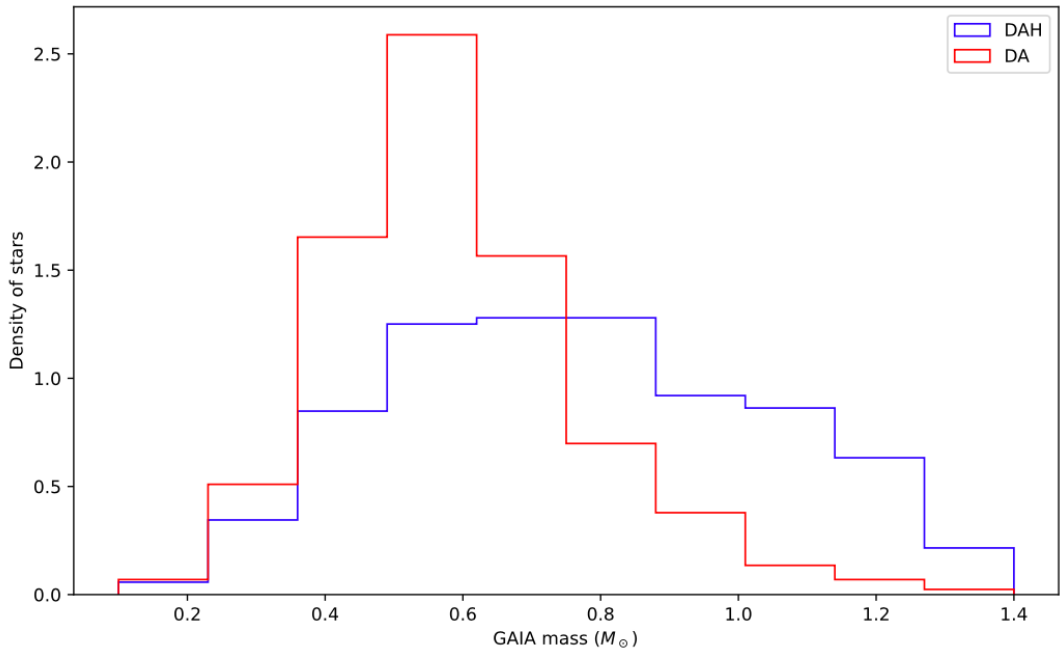

Figure 22 – Histogram of mass calculated with GAIA data for all DAs in red and only the magnetic ones in blue.

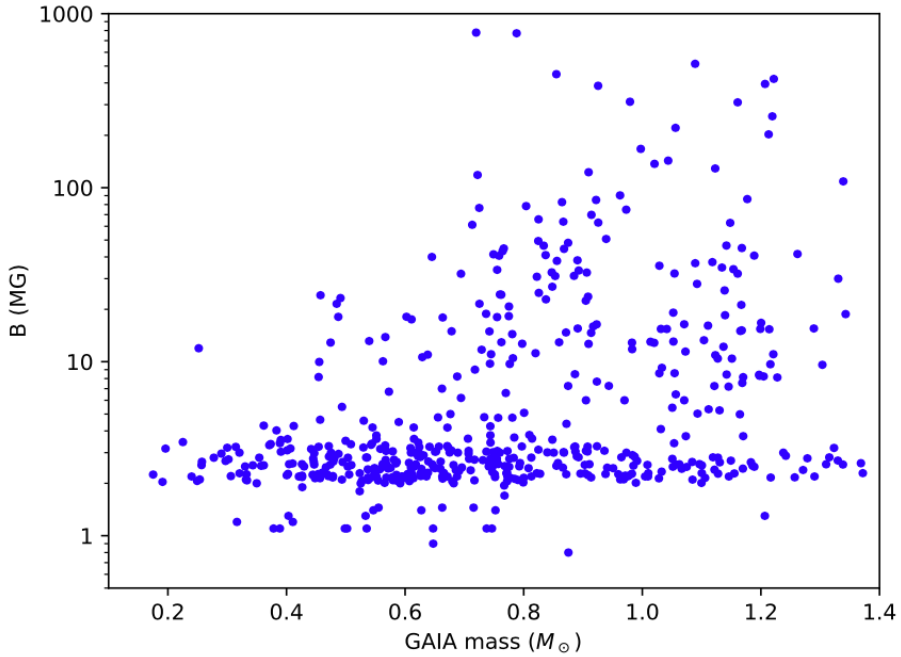

Figure 23 – Magnetic field versus mass calculated with GAIA data showing a clear absence of highly magnetic white dwarfs with lower masses.

It is perceptible that the distribution of mass of DAH can be approximated by a Gaussian centered in 0.78 $M_{\odot}$ with no further remarkable features. Meanwhile, Fig. 23 shows an evident lack of low mass DAH with strong fields.

6.3 Relation between effective temperature and magnetic field

In the search for a better understanding of the magnetic field origin, we investigate its relation to the effective temperature of the inspected stars. Fig. 24 shows that the magnetic field strength increases as the effective temperature decreases.

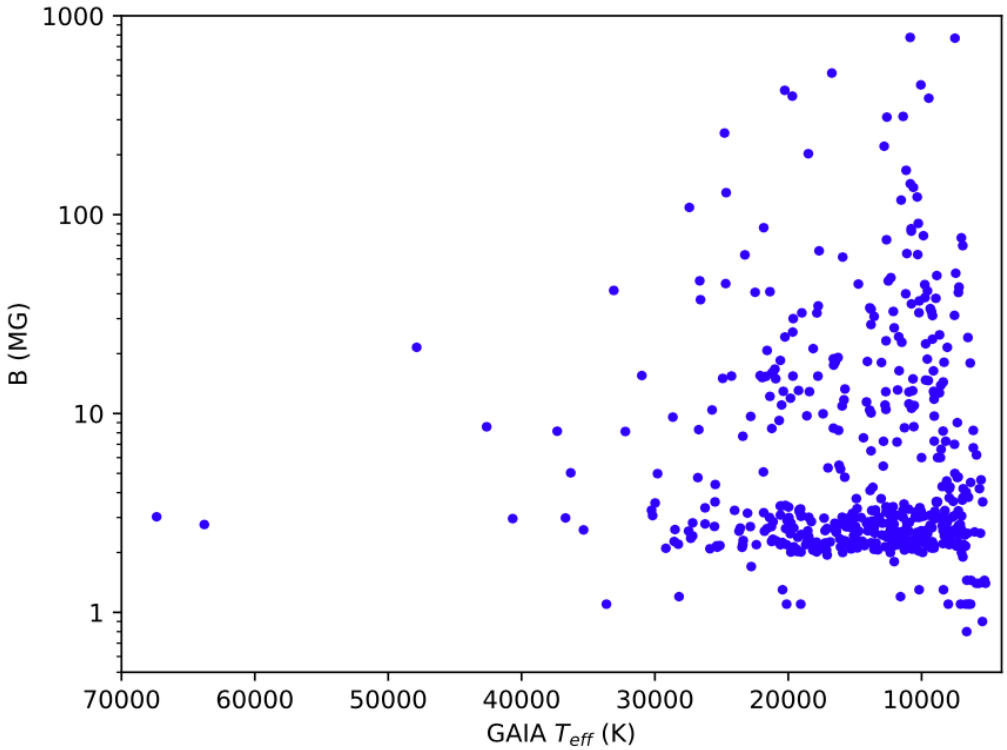

Figure 24 – Magnetic field versus effective temperature calculated with GAIA data showing a clear increase of highly magnetic white dwarfs with lower temperatures.

Not only do we find white dwarfs with stronger magnetic fields, but also we detect more magnetic white dwarfs at lower temperatures. The second effect is naturally expected because it is easier to detect white dwarfs at lower temperatures since they spend more time cooling down. To consider this effect and check if there are really more magnetic white dwarfs at lower temperatures, we study the fraction of DAH compared to the whole sample of white dwarfs rich in hydrogen. This is illustrated by Fig. 25 and it is noticeable that the fraction of magnetic stars is indeed increasing as the temperature decreases.

It is especially outstanding the rapid growth in magnetic fraction around effective temperature of 25 000 K ($\log T_{eff} \approx 4.4$), temperature at which a convective zone of helium is internally formed in the white dwarf that could be responsible for this increase.

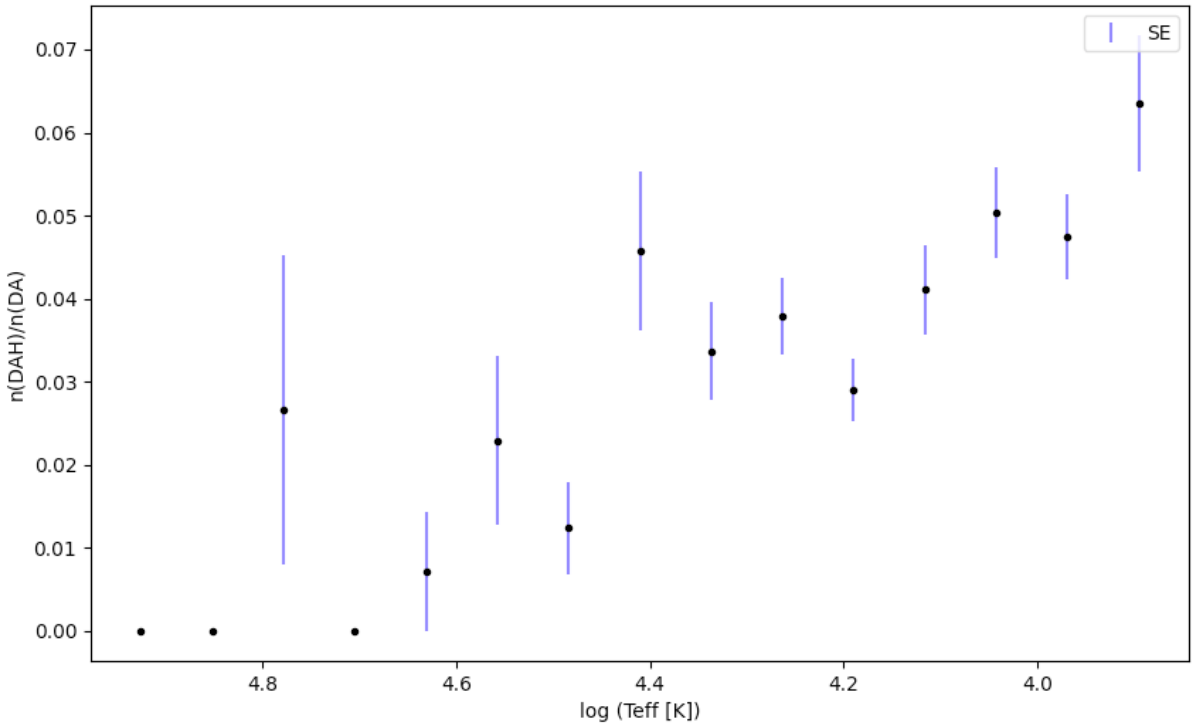

Figure 25 – The ratio of the number of DAHs to the number of DAs versus effective temperature showing a peak of abundance near T_{eff} = 25 000 K. The blue vertical lines represent the standard errors for each point.

We also call attention to the build-up in the magnetic fraction that starts around effective temperature of 16 000 K (log $T_{eff} \approx 4.2$). At this temperature, a convective zone of hydrogen is formed in the white dwarf, and it could be responsible for the rise in the magnetic fraction.

A question then arises: does the effect change depending on the stellar mass? To answer this question we divided our sample in two at M = 0.8 $M_{\odot}$and at M = 1 $M_{\odot}$and compared the results, which can be seen in the left and right panel of Fig. 26 respectively.

It is perceptible that the distribution of DAs doesn't change much except for the fact that there are considerably fewer stars with M>1 $M_{\odot}$. Differently, in the DAH there is a significant variation of the distribution. We highlight the valley around 10 000 K (log $T_{eff} = 4.0$) as being a consequence of convective mixing and dilution. They pollute the stellar atmosphere with helium and thin the hydrogen layer, reducing the number of DAs and augmenting the number of DABs or DBAs. This effect is constrained in temperature in consequence of the disappearance of the lines of helium at lower temperatures, meaning that the star may contain helium in its atmosphere, it is only not possible to observe it through the spectra.

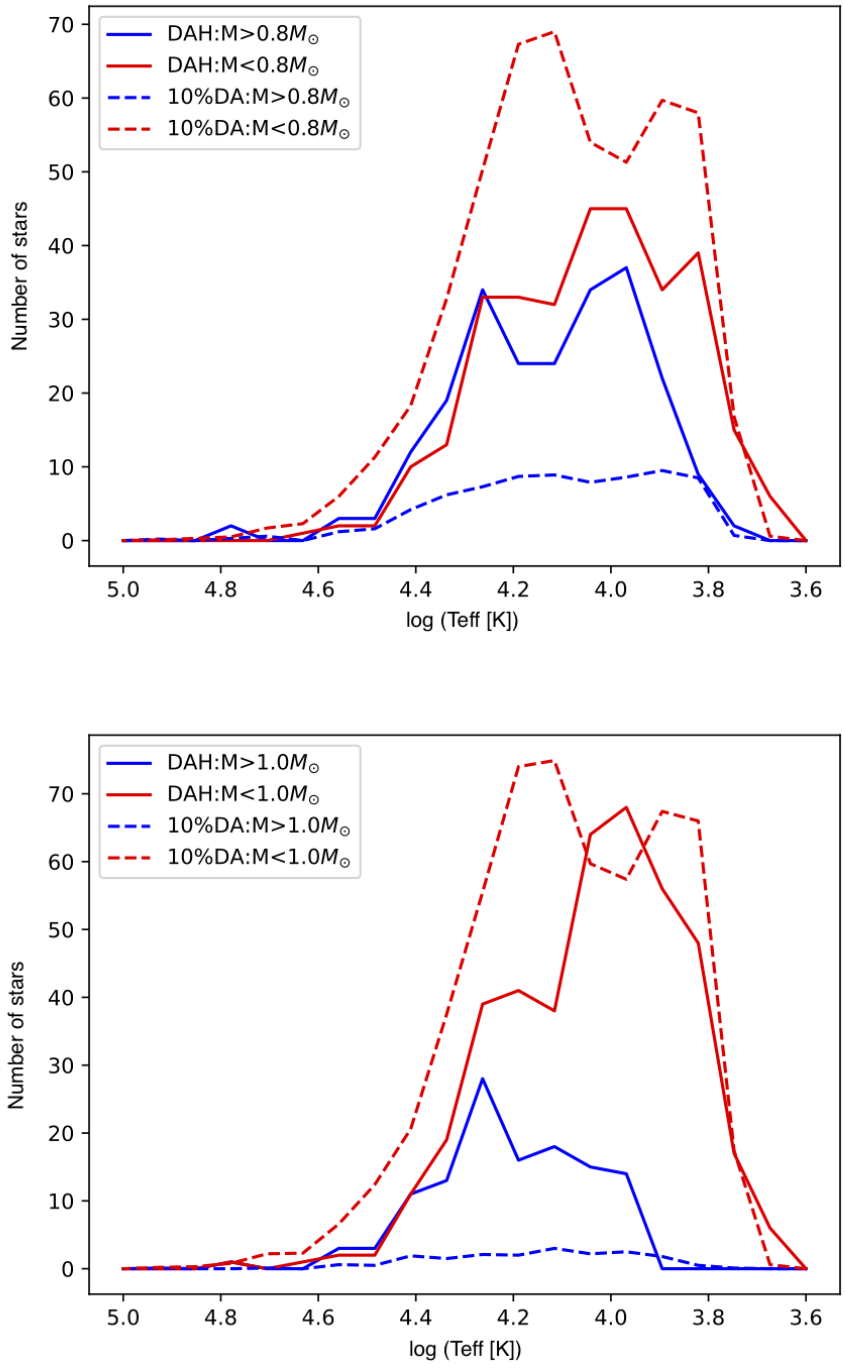

Figure 26 – Both panels show the number of DAHs and DAs versus the effective temperature. The sample was divided at 0.8 $M_\odot$and 1.0 $M_\odot$, represented in the upper panel and the lower panel respectively. We divided the absolute number of DAs by ten to allow better visualization. It is evident a change in behavior of the distribution of DAHs that is not accompanied by the distribution of DAs.

The magnetic DAs with mass above 0.8 $M_\odot$have a similar double peak behavior, even though it is more restricted in temperature. The magnetic DAs with mass above 1 $M_\odot$on the other hand have the second peak missing. Some mechanism must be inhibiting the magnetic field for higher masses at temperatures around 16 000 K (log $T_{eff} \approx 4.2$).

This same effect is not observed for masses below 1 $M_{\odot}$. In fact, the exact opposite occurs, and they show the second peak much higher than the first. The behavior of the lower mass DAHs is exactly the one discussed earlier thus becoming necessary the understanding of what could be suppressing the higher masses magnetic fields.

One very important physical process that is highly dependent on the white dwarf mass is the crystallization of its core, and we suppose that it is the one holding the magnetic field back. In the search for a better understanding of the relation between the crystallization and the magnetic field, we divided the star in two groups (the ones that have already started the crystallization process according to the models and the ones that haven't) and built Fig. 27. This figure was not very helpful since both groups present various magnetic field intensities.

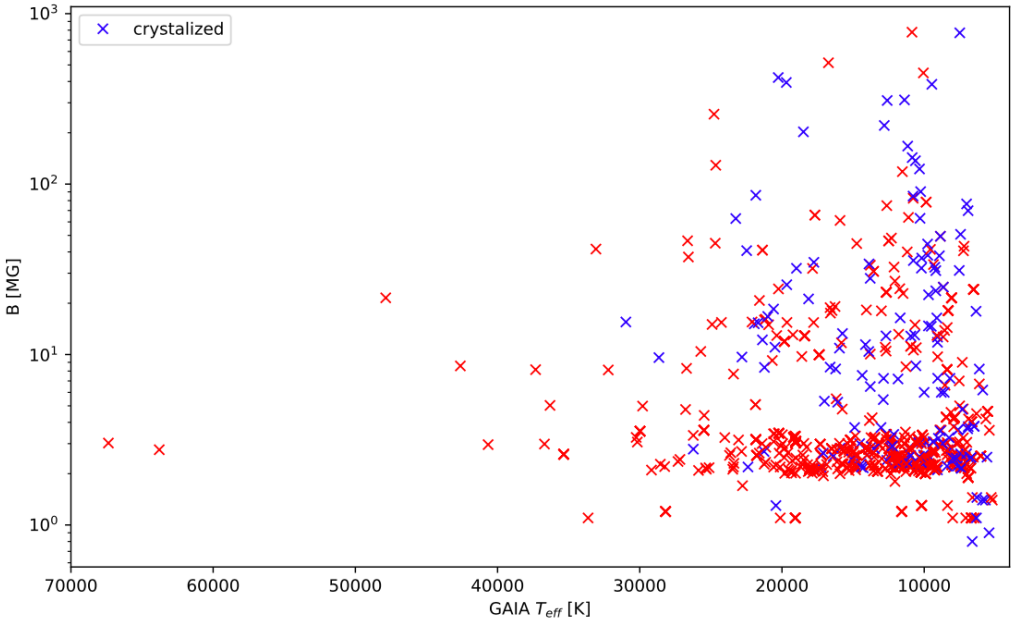

Figure 27 – Magnetic field versus effective temperature calculated with GAIA data showing no clear evidence of the influence of crystallization over the magnetic field strength.

To investigate this question even further, we built Fig. 28, in which one can see not only if the star has started to crystallize its core, but also have an idea of how advanced this process is. The further the star is from the crystallization line in the colder direction more crystallized its core is. We emphasize that the crystallization line has an intrinsic uncertainty to the models used to compute it.

It is recognizable that most of the stars with higher magnetic fields have started the crystallization process, which goes against the hypothesis that crystallization is responsible for the lower fraction of magnetic DAs with higher masses. In fact, Isern et al. (2017) proposed a mechanism of generation of magnetic fields of strengths of up to 0.1 MG by the dynamo in the convective region generated by the phase separation due to the crystallization process. Ginzburg, Fuller, and Kawka (2022) found that these fields could

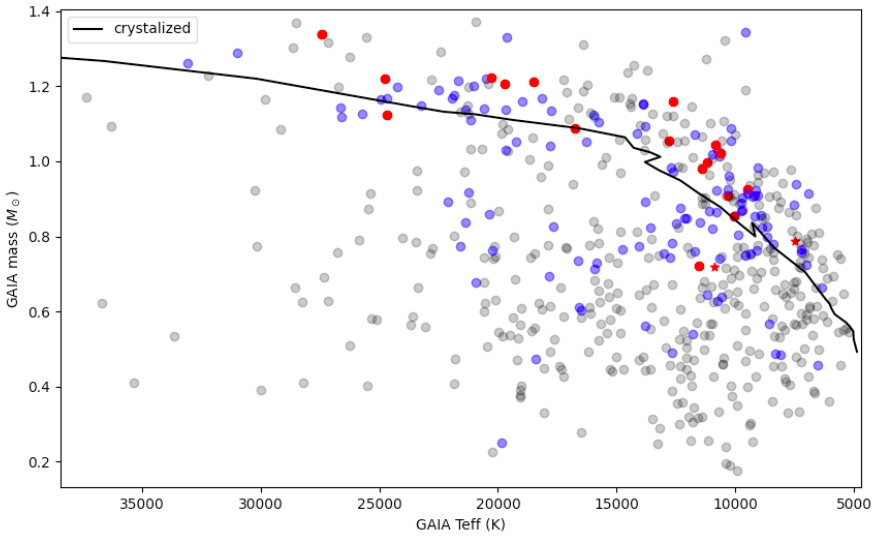

Figure 28 – Mass versus effective temperature calculated with GAIA data. The colors black, blue, and red represent magnetic fields below 10 MG, between 10-100 MG, and above 100 MG respectively. The two red stars represent the most magnetic DAs with a magnetic field above 700 MG. The solid black line represents the temperature of crystallization for the single evolution of white dwarfs of different masses as presented by Romero et al. (2013), Horowitz, Schneider, and Berry (2010) and Lauffer, Romero, and Kepler (2018). The crystallization increases to the right from the line.

go as high as 100 MG depending on the rotational period of the star and its mass.

6.4 Relation between periodicities and magnetic field

The periods detected are well spread and not localized around 2-3 hours as seen in Kawka (2020). Even though they are not necessarily the rotational periods, we looked for a relationship between them, the strength of the magnetic fields measured and the temperature of the star. We didn't find any significant trend as shown in Fig. 29.

This absence in correlation is in agreement with Brinkworth et al. (2013), who found no correlation between rotation period and mass, temperature, magnetic field, or age.

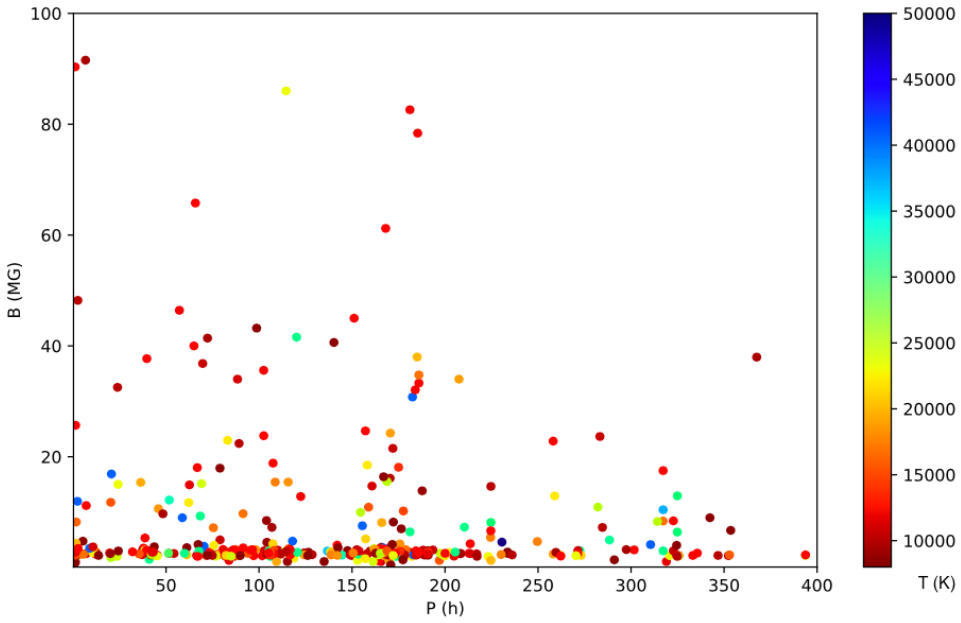

Figure 29 – Magnetic field versus variation period. The color of the dots indicates their respective temperatures in K.

6.5 Particular Stars

Some stars have more than one spectrum observed by SDSS in which it is possible to look for variability in the line profiles as an indication of the rotational period. Besides the inclination of the star in respect to the line of sight, which may allow us to see different portions of the stellar surface as it rotates, the line profiles can also change due to the misalignment between the magnetic field axis and the rotation axis.

Here we highlight the star SDSS J030407.40-002541.74 in which this effect is prominent. In Fig. 30 we can see that the H_α line varies between a deeper central line to equally deep triplet components. It is also visible that the $\sigma-$ component of the H_β line appears and disappears.

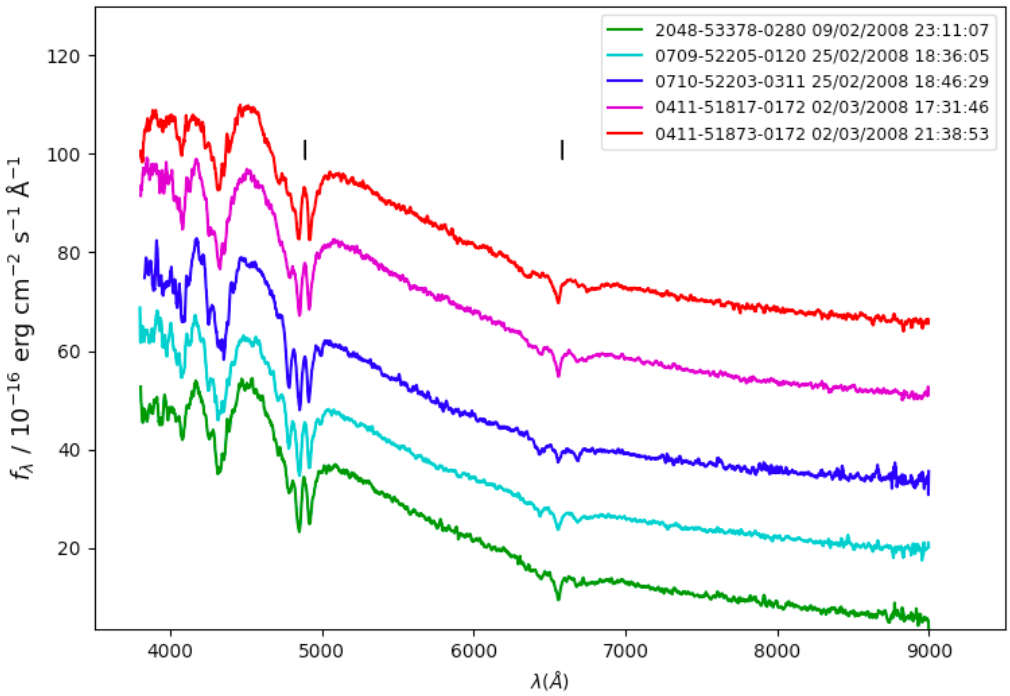

Figure 30 – Different spectra of SDSS J030407.40-002541.74 with their respective observation dates. The two small vertical black segments mark the position of H_β and H_α lines.

This star has also been observed by TESS and we have 30 minutes data from sectors 4 and 31. Unfortunately, no variation above the detection limit was identified, which is understandable since it is very faint (GAIA Mag = 17.8528).

The same process that affects the SDSSJ030407.40-002541.74 H_β lines could be responsible for the H_β line profile of SDSSJ030407.39-002541.9 which is illustrated in Fig. 31. Kilic et al. (2021) argued that assuming a hydrogen atmosphere, an inclination, and an offset dipole geometry the lines could not be reasonably reproduced. We found a very good fit to the observed spectra except for the lateral components of the H_β line, which is expected to change as shown for SDSSJ030407.40-002541.74.

Kilic et al. (2021) assumed then a centered dipole as in Fig 31 lower panel and explained the difference in the line depth between the model and the observed spectra with the assumption of a non-pure hydrogen atmosphere. We believe that this additional complexity is not needed to explain the data.

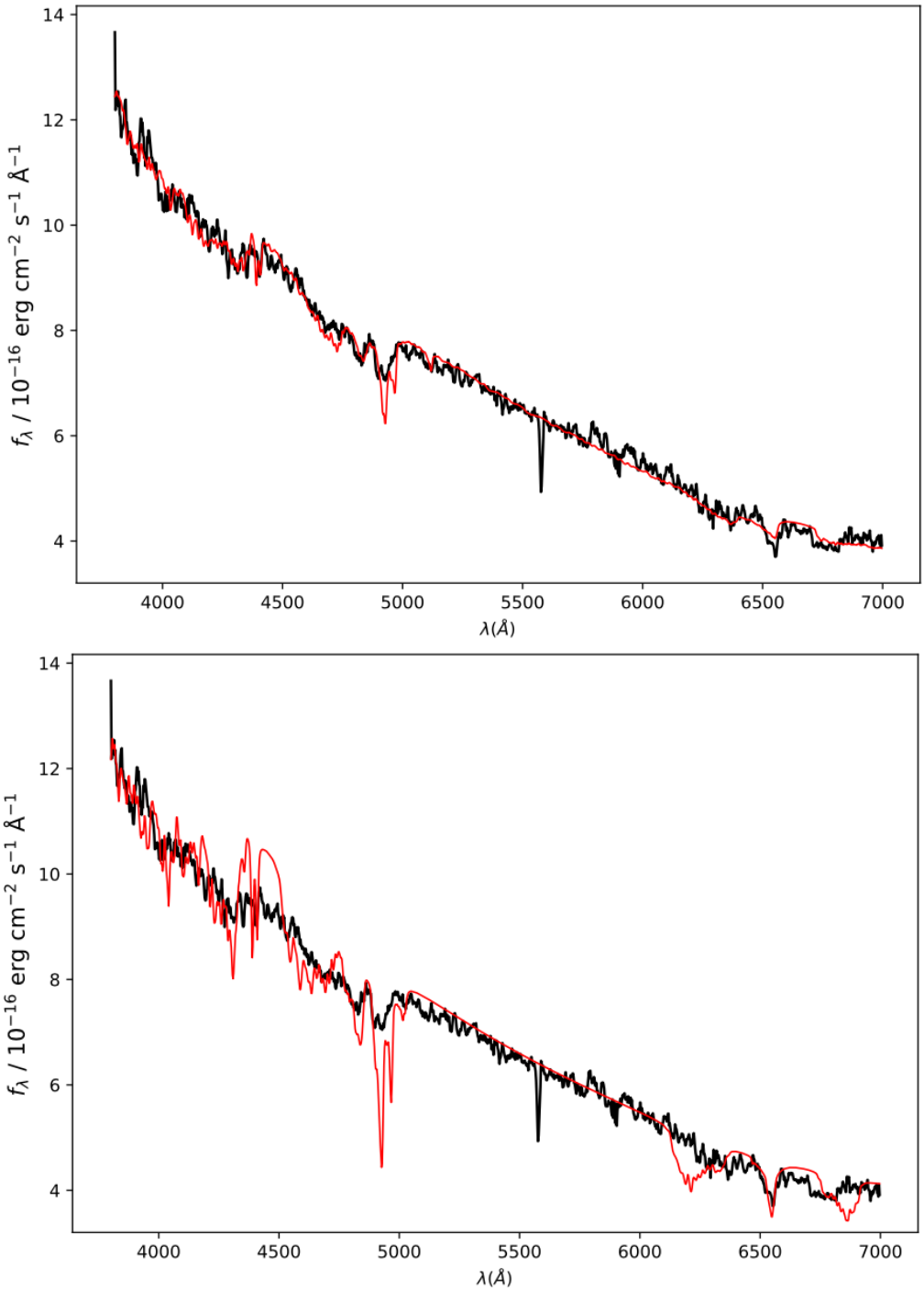

Figure 31 – Observed spectrum of SDSSJ030407.39-002541.9. The model with the best least-squares fit to the data is shown in red. We highlight that the line near 5 500Å is due to systematic error of joining to different observations by SDSS. The upper panel shows a model with computed offset magnetic dipole field geometry while the lower panel shows a model computed not inclined centered magnetic dipole field geometry with the strength found in the previous calculation.

7 Conclusions

In this work, we estimated magnetic field strength for 803 white dwarfs observed from SDSS and the photometric variability of 380 white dwarfs observed with TESS. It consists of the largest number of magnetic field and variation period determinations to date. We searched for relations between magnetic field strength and stellar mass, effective temperature, variation period, and crystallization status.

It was found that a considerable percentage of DAH have fields below 3 MG. This is, to some extent, biased from our spectroscopic method but could also mean that lower fields are more abundant in white dwarfs. This result is in opposition to Bagnulo, and Landstreet (2021) which concluded that within the range of field strength found in the 20 pc volume, which extends between about 40 kG and 300 MG, the probability of fields occurring is roughly constant per dex of field strength.

We found that the magnetic field strength increases as the effective temperature decreases, together with an increase in the fraction of magnetic white dwarfs. This effect corroborates with the surface magnetic field being generated or enhanced in the white dwarf cooling phase.

We could also observe that the highest fields tend to occur in the more massive stars, and that the mean mass was in general higher than the non-magnetic ones (0.78 $M_{\odot}$compared to the usual 0.6 $M_{\odot}$). This does not give us any new information about the origin of the magnetic field because many assumptions already consider a higher mass. But a physical property closely related to the mass is the crystallization, and we found that the most magnetic ones tend to be already crystallized. This is expected since DAH have higher masses so they crystallize at higher temperatures but spend more time (easier to detect) at lower temperatures (already crystallized).

Unfortunately, our investigation around the relation between magnetic field strength and variation period resulted in no clear correlation found. This could be in the future improved by identifying which periods are actually due to rotation and which are related to other sources. So, no conclusion about the origin of the magnetic field can be derived from variability.

The limitations of our work and how they could be improved are as follows:

1. - We considered $\log g = 8$, which is a good approximation for white dwarfs in general but not for the magnetic subgroup, that tends to be more massive. To advance the research, one could consider a $\log g$ more representative of the magnetic sample or augment it even further considering individually the $\log g$ for each star.

2. - Only hydrogen transition lines up to level 7 were considered, even though there are Balmer transitions up to principal quantum number n = 10 available in the literature. The results of our work could be slightly improved by adding these existing models.

3. - It is not certain from the literature if DAHs are good representatives of the other classes of magnetic white dwarfs, even though Bagnulo, and Landstreet (2021) suggest that they are. To corroborate this conclusion it's necessary a study of an extensive sample of other white dwarfs, for which it is crucial a better understanding of the effect of magnetic fields over other atoms besides hydrogen. This is slowly being achieved in the literature.

Bibliography

Achilleos, N.; Remillard, R. A.; Wickramasinghe, D. T. Serendipitous identifications of two magnetic white dwarfs. *MNRAS*, v. 253, p. 522, dez. 1991. Quoted on the page 60.

Achilleos, N.; Wickramasinghe, D. T. Offset Magnetic Dipoles in White Dwarfs. *ApJ*, v. 346, p. 444, nov. 1989. Quoted on the page 25.

Ahumada, R. et al. The 16th Data Release of the Sloan Digital Sky Surveys: First Release from the APOGEE-2 Southern Survey and Full Release of eBOSS Spectra. *ApJS*, v. 249, n. 1, p. 3, jul. 2020. Quoted on the page 22.

Angel, J. R. P.; Borra, E. F.; Landstreet, J. D. The magnetic fields of white dwarfs. *ApJS*, v. 45, p. 457–474, mar. 1981. Quoted on the page 60.

Babcock, H. W. Zeeman Effect in Stellar Spectra. *ApJ*, v. 105, p. 105, jan. 1947. Quoted on the page 20.

Bagnulo, S.; Landstreet, J. D. New insight into the magnetism of degenerate stars from the analysis of a volume-limited sample of white dwarfs. *MNRAS*, v. 507, n. 4, p. 5902–5951, nov. 2021. Quoted 4 times on the pages 41, 42, 53, and 54.

Belloni, D.; Schreiber, M. R. Are white dwarf magnetic fields in close binaries generated during common-envelope evolution? *MNRAS*, v. 492, n. 1, p. 1523–1529, fev. 2020. Quoted on the page 21.

Bergeron, P.; Ruiz, M.-T.; Leggett, S. K. Discovery of Two Cool Magnetic White Dwarfs. *ApJ*, v. 400, p. 315, nov. 1992. Quoted on the page 60.

Brinkworth, C. S. et al. Measuring the Rotational Periods of Isolated Magnetic White Dwarfs. *ApJ*, v. 773, n. 1, p. 47, ago. 2013. Quoted 3 times on the pages 21, 36, and 50.

Chaisson, E.; McMillian, S. *Astronomy Today*. [S.l.]: Pearson, 2014. Quoted 2 times on the pages 10 and 11.

Erika, B.-V. *Introduction to Stellar Astrophysics, Volume 3 Stellar structure and evolution*. [S.l.]: Cambridge University Press, 1992. Quoted on the page 15.

Euchner, F. et al. Zeeman tomography of magnetic white dwarfs. I. Reconstruction of the field geometry from synthetic spectra. *A&A*, v. 390, p. 633–647, ago. 2002. Quoted on the page 23.

Euchner, F. et al. Zeeman tomography of magnetic white dwarfs. II. The quadrupole-dominated magnetic field of <ASTROBJ>HE 1045-0908</ASTROBJ>. *A&A*, v. 442, n. 2, p. 651–660, nov. 2005. Quoted on the page 60.

Feinstein, A. D. et al. eleanor: An Open-source Tool for Extracting Light Curves from the TESS Full-frame Images. *PASP*, v. 131, n. 1003, p. 094502, set. 2019. Quoted on the page 36.

Gaia Collaboration et al. The Gaia mission. *A&A*, v. 595, p. A1, nov. 2016. Quoted on the page 22.

Gentile Fusillo, N. P. et al. A catalogue of white dwarfs in Gaia EDR3. *MNRAS*, v. 508, n. 3, p. 3877–3896, dez. 2021. Quoted on the page 22.

Gianninas, A.; Bergeron, P.; Ruiz, M. T. A Spectroscopic Survey and Analysis of Bright, Hydrogen-rich White Dwarfs. *ApJ*, v. 743, n. 2, p. 138, dez. 2011. Quoted on the page 60.

Ginzburg, S.; Fuller, J.; Kawka, A. Slow convection and fast rotation in crystallization-driven white dwarf dynamos. *arXiv e-prints*, p. arXiv:2202.12902, fev. 2022. Quoted on the page 48.

Greenstein, J. L. Spectrophotometry of Magnetic Degenerate Stars. *ApJ*, v. 194, p. L51, nov. 1974. Quoted on the page 60.

Heber, U.; Napiwotzki, R.; Reid, I. N. Rotation velocities of white dwarf stars. *A&A*, v. 323, p. 819–826, jul. 1997. Quoted on the page 19.

Horowitz, C. J.; Schneider, A. S.; Berry, D. K. Crystallization of Carbon-Oxygen Mixtures in White Dwarf Stars. *Phys. Rev. Lett.*, v. 104, n. 23, p. 231101, jun. 2010. Quoted on the page 49.

Isern, J. et al. A Common Origin of Magnetism from Planets to White Dwarfs. *ApJ*, v. 836, n. 2, p. L28, fev. 2017. Quoted 2 times on the pages 21 and 48.

Jordan, S. Models of white dwarfs with high magnetic fields. *A&A*, v. 265, p. 570–576, nov. 1992. Quoted on the page 23.

Kawka, A. Clues to the origin and properties of magnetic white dwarfs. *IAU Symposium*, v. 357, p. 60–74, jan. 2020. Quoted 2 times on the pages 21 and 50.

Kawka, A.; Vennes, S. Spectroscopic Identification of Cool White Dwarfs in the Solar Neighborhood. *ApJ*, v. 643, n. 1, p. 402–415, maio 2006. Quoted on the page 60.

Kemp, J. C. et al. Discovery of Circularly Polarized Light from a White Dwarf. *ApJ*, v. 161, p. L77, ago. 1970. Quoted on the page 20.

Kepler, S. O. Whole earth telescope data analysis. *Baltic Astronomy*, v. 2, p. 515–529, jan. 1993. Quoted on the page 36.

Kepler, S. O. et al. White dwarf and subdwarf stars in the Sloan Digital Sky Survey Data Release 16. *MNRAS*, v. 507, n. 3, p. 4646–4660, nov. 2021. Quoted on the page 22.

Kepler, S. O. et al. Magnetic white dwarf stars in the Sloan Digital Sky Survey. *MNRAS*, v. 429, n. 4, p. 2934–2944, mar. 2013. Quoted 3 times on the pages 19, 20, and 21.

Kilic, M. et al. The 100 pc White Dwarf Sample in the SDSS Footprint. *ApJ*, v. 898, n. 1, p. 84, jul. 2020. Quoted on the page 60.

Kilic, M. et al. An Isolated White Dwarf with a 70 second Spin Period. *arXiv e-prints*, p. arXiv:2111.14902, nov. 2021. Quoted 2 times on the pages 51 and 52.

King, A. R.; Pringle, J. E.; Wickramasinghe, D. T. Type Ia supernovae and remnant neutron stars. *MNRAS*, v. 320, n. 3, p. L45–L48, jan. 2001. Quoted on the page 21.

Kleinman, S. J. et al. SDSS DR7 White Dwarf Catalog. *ApJS*, v. 204, n. 1, p. 5, jan. 2013. Quoted on the page 60.

Koester, D. White dwarf spectra and atmosphere models. *Mem. Soc. Astron. Italiana*, v. 81, p. 921–931, jan. 2010. Quoted on the page 23.

Külebi, B. et al. Analysis of hydrogen-rich magnetic white dwarfs detected in the Sloan Digital Sky Survey. *A&A*, v. 506, n. 3, p. 1341–1350, nov. 2009. Quoted 3 times on the pages 20, 23, and 29.

Külebi, B. *Constraints on the Origin of Magnetic White Dwarfs*. 2010. Dissertation submitted to the Combined Faculties of the Natural Sciences and Mathematics of the Ruperto-Carola-University of Heidelberg, Germany for the degree of Doctor of Natural Sciences. Quoted on the page 24.

Landstreet, J. D.; Bagnulo, S. Discovery of kilogauss magnetic fields on the nearby white dwarfs WD 1105-340 and WD 2150+591. *A&A*, v. 623, p. A46, mar. 2019. Quoted on the page 60.

Landstreet, J. D. et al. Discovery of an extremely weak magnetic field in the white dwarf LTT 16093 = WD 2047+372. *A&A*, v. 591, p. A80, jun. 2016. Quoted on the page 20.

Lauffer, G. R.; Romero, A. D.; Kepler, S. O. New full evolutionary sequences of H- and He-atmosphere massive white dwarf stars using MESA. *MNRAS*, v. 480, n. 2, p. 1547–1562, out. 2018. Quoted 2 times on the pages 15 and 49.

Liebert, J.; Bergeron, P.; Holberg, J. B. The True Incidence of Magnetism Among Field White Dwarfs. *AJ*, v. 125, n. 1, p. 348–353, jan. 2003. Quoted on the page 41.

McCleery, J. et al. Gaia white dwarfs within 40 pc II: the volume-limited Northern hemisphere sample. *MNRAS*, v. 499, n. 2, p. 1890–1908, dez. 2020. Quoted on the page 60.

McCook, G. P.; Sion, E. M. A Catalog of Spectroscopically Identified White Dwarfs. *ApJS*, v. 121, n. 1, p. 1–130, mar. 1999. Quoted on the page 16.

Raddi, R. et al. Multiband photometry and spectroscopy of an all-sky sample of bright white dwarfs. *MNRAS*, v. 472, n. 4, p. 4173–4192, dez. 2017. Quoted on the page 60.

Ricker, G. R. et al. Transiting Exoplanet Survey Satellite (TESS). *Journal of Astronomical Telescopes, Instruments, and Systems*, v. 1, p. 014003, jan. 2015. Quoted on the page 22.

Romero, A. D. et al. Asteroseismological Study of Massive ZZ Ceti Stars with Fully Evolutionary Models. *ApJ*, v. 779, n. 1, p. 58, dez. 2013. Quoted on the page 49.

Schimeczek, C.; Wunner, G. Atomic Data for the Spectral Analysis of Magnetic DA White Dwarfs in the SDSS. *ApJS*, v. 212, n. 2, p. 26, jun. 2014. Quoted 5 times on the pages 23, 31, 32, 34, and 35.

Schreiber, M. R. et al. Magnetic dynamos in white dwarfs - II. Relating magnetism and pollution. *MNRAS*, v. 506, n. 1, p. L29–L34, set. 2021. Quoted on the page 21.

Spruit, H. C. Origin of the rotation rates of single white dwarfs. *A&A*, v. 333, p. 603–612, maio 1998. Quoted on the page 21.

Tout, C. A. et al. Binary star origin of high field magnetic white dwarfs. *MNRAS*, v. 387, n. 2, p. 897–901, jun. 2008. Quoted on the page 21.

Tremblay, P. E. et al. Gaia white dwarfs within 40 pc - I. Spectroscopic observations of new candidates. *MNRAS*, v. 497, n. 1, p. 130–145, set. 2020. Quoted on the page 60.

Vanlandingham, K. M. et al. Magnetic White Dwarfs from the SDSS. II. The Second and Third Data Releases. *AJ*, v. 130, n. 2, p. 734–741, ago. 2005. Quoted on the page 20.

Wesemael, F. et al. An Atlas of Optical Spectra of White-Dwarf Stars. *PASP*, v. 105, p. 761, jul. 1993. Quoted on the page 60.

Wickramasinghe, D. T.; Ferrario, L. The origin of the magnetic fields in white dwarfs. *MNRAS*, v. 356, n. 4, p. 1576–1582, fev. 2005. Quoted on the page 20.

Wickramasinghe, D. T.; Whelan, J. A. J.; Bessell, M. S. A hot magnetic DA white dwarf with a field of 2 - 4×10^7 gauss. *MNRAS*, v. 180, p. 373–378, ago. 1977. Quoted on the page 60.

Zettili, N. *Quantum Mechanics - Concepts and Applications*. [S.l.]: Wiley, 2009. Quoted on the page 17.

Appendix

A) DAHs with 120 and 20 seconds TESS data

A comparison between the periods determined with 30 minutes cadence and 120/20 seconds cadence is presented in Table 2.

TIC	30 min period (h)	120/20s period (h)
82596432	270.42	289.69
87547997	106.81	236.70
137733927	79.04	35.25
141117787	6.71	6.70
141874000	190.95	19.16
165916724	89.26	0.09
188595599	166.62	135.18
306449009	58.15	66.85
357441103	166.97	63.57
453828065	111.83	110.87
471014089	153.41	58.88
900490689	172.10	173.86
1101159910	317.25	115.56
1205040141	106.03	77.99

Table 2 – The table presents the TIC and highest amplitude period of variability above the FAP for the 30 minutes cadence and the 120/20 seconds cadence data.

B) Previously known magnetic DAs with TESS

For the purpose of completeness we present the Table 3 with variational period measured for previously known magnetic DAs. Between these star we highlight TIC 267166358 as an example of 20s cadence data and detection of short periods. It's Fourier transform is presented in Fig. 32.

TIC	FAP	Period	Classification	References
55096188	4.326	2.75013h@5.102mma	DAH	[1]
85585141	5.043	5.952h@13.605mma	DAH	[2]
91329200	8.023	164307.90s@20.824mma	DAH	[3]
142871516	8.827	24.85987h@45.229mma	DAH	[3]
149767969	4.118	204599.84s@7.652mma	DAH	[3]
201892746	1.788	4.008h@3.407mma	DAH	[4]
274239484	0.991	6937.80s@6.42933	DAH	[5]
283414280	18.871	114.304h@51.973mma	DAH	[6]
289712694	2.381	2650.7300s@3.404mma	DAH	[7]
301021757	2.740	342.45s@3.223mma	DAH	[8]
321159503	7.714	1677.1s@11.11mma	DAH	[9]
345036441	6.542	5924.28s@11.597mma	DAH	[4]
376020501	47.109	547087.14s@97.708mma	DAH	[10]
471013547	6.251	42.49954h@18.272mma	DAH	[11]
1101327387	45.152	4699.45s@217.279mma	DAH	[3]
453828065	4.759	110.87646h@20.319mma	DAH	[12]
115613388	1.354	2534.13s@1.730mma	DAP	[13]
229797408	0.165	153.50411h@0.406mma	DAP	[14]
267166358	0.922	725.725371677s@26.316mma	DAP	[15]
321979116	0.244	2.69517h@2.303mma	DAP	[13]
471013569	83.876	4.10h=14754.05s@88.937mma	DAP	[15]

Table 3 – The table presents the TIC, False Alarm Probability, highest amplitude period of variability above the FAP, together with the spectral classification and its respective reference. [1]-Euchner et al. (2005); [2]-Kawka, and Vennes (2006); [3]-Kilic et al. (2020); [4]-Angel, Borra, and Landstreet (1981); [5]-Greenstein (1974); [6]-Landstreet, and Bagnulo (2019); [7]-Bergeron, Ruiz, and Leggett (1992); [8]-Achilleos, Remillard, and Wickramasinghe (1991); [9]-Tremblay et al. (2020); [10]-Raddi et al. (2017); [11]-Kleinman et al. (2013); [12]-McCleery et al. (2020); [13]-Gianninas, Bergeron, and Ruiz (2011); [14]-Wesemael et al. (1993); [15]-Wickramasinghe, Whelan, and Bessell (1977)

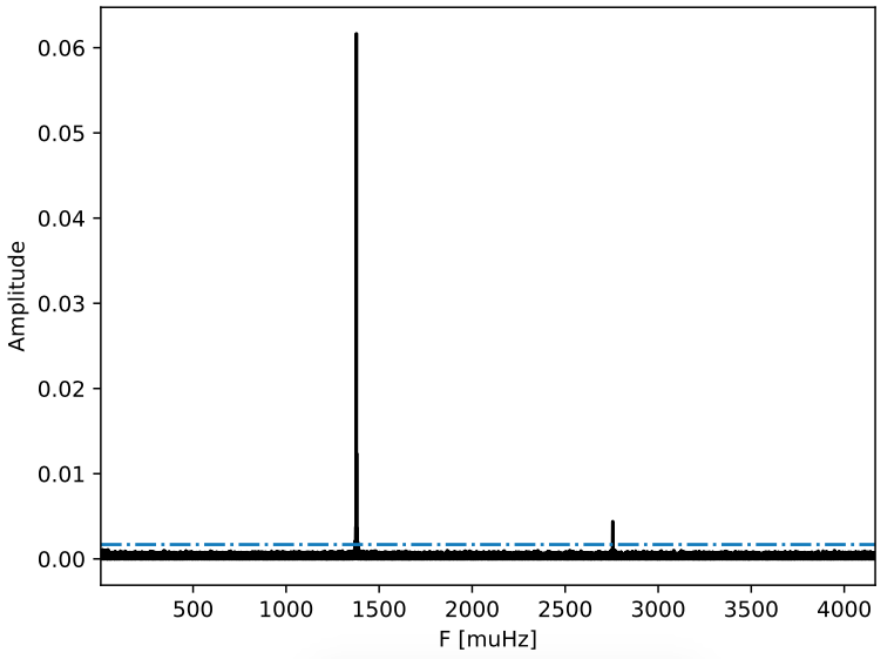

Figure 32 – Fourier Transform for the 20 seconds cadence data of the star with TIC 267166358. The blue line is the False Alarm Probability. The higher amplitude peak is 1379 μ Hz or 725 s.

C) Complete table of determined magnetic fields

To compute the uncertainty in our measurements of magnetic field we used the fact that when using χ^2 if we have a minimum χ_0^2 and change one parameter by d we obtain a new value o $\tilde{\chi}^2$:

$$\tilde{\chi}^2 = \chi_0^2 + \frac{d^2}{\sigma} \implies \sigma = \frac{d^2}{\tilde{\chi}^2 - \chi_0^2},$$

where σ is the uncertainty of the measurement. The mean value of this uncertainty is 3 MG, or in relative terms 12%.

To compute the uncertainty in our measurements of the photometric variability we consider:

$$f = \frac{1}{P} \implies df = \frac{dP}{P^2}.$$

The biggest period that can be considered being the length of the data-set (T), the smallest step in frequency became $dF = T^{-1}$. With this information we computed dP and present it in Table 4. The mean value of this uncertainty is 16%.

SDSS name	PMF	TIC	$T_{eff}(K)$	z_{offset}	incl	B (MG)	dB (MG)	P(h)	dP(h)
J120924.84+331716.3	2004-53737-0418	954316658	8000	-0.26	8.16	4.03	0.23	324.50	162.50
J120547.47+340811.4	2089-53498-0431	954314032	17500	-0.35	60.8	9.74	0.07	91.41	12.89
J121529.84+335158.6	1999-53503-0238	954302696	25000	0.17	0.26	2.6	2.2	197.43	60.15
J122100.20+244443.7	2657-54502-0026	954213969	10500	-0.3	59.35	2.25	0.01	184.43	52.49
J121033.23+221402.6	2644-54210-0167	954207893	10500	-0.3	59.99	2.23	1.65	324.50	162.50
J124751.79+262110.2	5987-56339-0712	954179915	8000	-0.13	21.35	43.21	27.89	98.71	15.04
J121110.29+203429.0	2609-54476-0564	954091318	25000	0.11	0.15	2.26	0.01	nov	—
J121211.27+185228.9	2609-54476-0005	954079192	25000	0.5	3.81	10.92	1.22	282.18	122.88
J121706.46+172855.9	2596-54207-0023	954045818	25000	0.0	33.47	1.2	0.0	—	—
J131426.37+173228.0	2604-54484-0481	953937942	8000	-0.35	13.68	2.62	0.15	nov	—
J124852.85+153641.9	5414-56014-0423	953905152	14000	0.25	3.76	2.7	0.17	185.91	53.34
J123531.30+154418.2	5404-56013-0896	953900136	8000	-0.15	26.27	50.74	16.26	—	—
J123449.88+150348.8	1768-53442-0557	953898624	8000	-0.06	5.68	8.22	0.3	172.22	45.77
J123527.08+145318.6	1768-53442-0074	953898456	16500	0.11	22.21	2.06	0.02	—	—
J125511.49+154929.7	2602-54149-0249	953879555	10000	-0.3	72.69	2.24	0.01	—	—
J125553.38+152555.0	1771-53498-0343	953877146	22000	0.26	33.17	12.88	0.05	—	—
J124819.86+133555.5	1694-53472-0564	953853272	13000	-0.25	82.57	2.14	0.01	97.11	14.55
J120806.25+144942.8	1764-53467-0112	953811354	18000	0.0	33.47	4.7	0.02	249.62	96.16
J121735.25+082810.0	5393-55946-0981	953705711	15000	-0.38	58.03	2.57	0.39	200.00	61.73

Table 4 – The table presents effective temperatures estimated with non-magnetic models used as an fixed input for YAWP besides off-set dipole geometry and the z_{offset}, inclination, magnetic field modulus and uncertainties resulted from the best model for each star. In addition to the results from spectroscopic analysis, the two last columns present the period of highest amplitude from TESS photometry and their respective uncertainties. The stars that were observed by TESS but no period was detected above the FAP are classified as nov (not observed to vary).

SDSS name	PMF	TIC	$T_{eff}(K)$	z_{offset}	incl	B (MG)	dB (MG)	P(h)	dP(h)
J120125.38+084800.3	5389-55953-0671	953680123	8000	-0.1	11.69	2.15	0.08	—	—
J120609.81+081323.7	1623-53089-0573	953677401	16000	0.01	51.31	449.1	35.47	—	—
J131050.04+143520.4	1772-53089-0559	953619288	40000	0.48	2.18	4.15	0.0	310.50	148.78
J131508.96+093713.8	5426-55987-0342	953541114	22000	-0.5	18.22	12.93	8.36	258.96	103.49
J131802.48+071743.2	5429-55979-0448	953511994	15500	0.46	4.43	3.17	0.05	—	—
J124058.11+063645.6	5407-55926-0250	953467669	11000	0.1	32.16	2.08	0.17	—	—
J122238.86+005034.4	2568-54153-0411	953324500	13500	0.15	10.81	2.19	0.01	—	—
J122209.43+001534.1	2568-54153-0471	953323084	19500	0.27	0.79	8.0	0.02	—	—
J121209.31+013627.7	0518-52282-0285	953321496	10500	-0.49	45.46	10.97	0.84	—	—
J121840.75-001005.8	2568-54153-0309	953304337	25000	0.16	89.99	2.33	0.0	—	—
J121635.36-002656.3	0288-52000-0276	953302884	15000	-0.18	59.27	64.24	0.11	—	—
J121105.25-004628.5	0287-52023-0253	953299929	19500	-0.32	66.65	2.56	0.01	—	—
J123706.24-001603.9	2920-54562-0110	953273983	11000	-0.38	62.18	2.55	0.01	—	—
J130805.95+035424.3	4760-55656-0470	953226577	13000	0.3	73.67	2.19	0.13	—	—
J131955.04+015259.5	4006-55328-0358	953160782	12500	0.48	5.3	3.24	0.09	96.41	14.34
J130807.48-010117.0	0294-51986-0089	953140278	18500	-0.21	72.94	2.2	0.0	—	—
J124851.30-022924.7	2922-54612-0607	953088455	9500	-0.15	16.53	4.26	0.4	—	—
J121557.40+665344.5	0493-51957-0104	950688902	8000	-0.35	5.79	2.73	0.35	nov	—
J123159.51+670918.9	7120-56720-0653	950685205	14500	0.49	3.91	3.45	0.56	2.71	0.0028
J122739.16+661224.3	7120-56720-0426	950683981	19000	-0.4	49.18	24.27	4.9	170.60	11.23
J120803.25+625815.3	0778-54525-0511	950622459	40000	0.49	10.42	3.35	0.0	107.65	4.47
J120150.14+614256.8	7106-56663-0100	950603990	10500	-0.49	53.43	14.72	1.54	160.73	9.97
J125040.81+590341.6	2461-54570-0219	950578485	30000	0.0	33.47	2.8	0.01	205.46	32.57
J130033.46+590406.9	2461-54570-0015	950570353	8000	-0.12	36.05	6.72	0.27	353.57	64.31
J124508.48+591551.6	2461-54570-0264	950565443	24000	0.0	33.47	1.1	0.0	161.32	13.39
J125415.99+561204.6	1318-52781-0299	950551887	11500	0.39	13.29	82.6	0.41	181.13	25.31
J125121.86+543215.7	6679-56401-0398	950497645	8500	-0.46	41.29	13.85	0.4	187.71	27.19
J123204.19+522548.2	0885-52379-0319	950487383	8183	-0.13	37.4	8.16	0.04	nov	—

SDSS name	PMF	TIC	$T_{eff}(K)$	z_{offset}	incl	B (MG)	dB (MG)	P(h)	dP(h)
J122249.13+481133.1	1451-53117-0582	950368516	9000	-0.34	77.45	9.71	0.3	48.32	3.60
J124322.38+450002.0	6635-56370-0334	950329680	9500	-0.12	49.92	48.22	36.92	2.57	0.01
J120728.95+440731.6	1369-53089-0048	950314720	19000	0.12	32.1	2.16	0.01	88.90	12.20
J122401.47+415551.9	1452-53112-0181	950280457	10000	-0.28	58.89	23.65	1.21	283.26	123.82
J122748.85+385546.3	1986-53475-0090	950258253	13000	-0.5	62.18	8.44	0.28	322.75	160.75
J124906.90+432543.0	6617-56365-0033	950228416	30000	-0.41	69.68	2.76	0.25	120.65	22.46
J125232.05+423210.8	6619-56371-0368	950225900	30000	-0.37	63.32	2.57	0.24	nov	—
J124816.81+411051.2	4703-55617-0381	950222527	13500	-0.5	50.82	3.09	0.11	—	—
J124806.37+410427.1	1456-53115-0190	950220586	8000	-0.21	7.04	4.8	0.22	—	—
J130214.98+415726.0	1458-53119-0490	950216774	17000	0.24	34.29	2.88	0.01	nov	—
J125101.98+351913.6	1987-53765-0570	950132116	25000	-0.12	0.13	2.25	1.58	43.43	2.91
J125709.63+304317.2	1994-53845-0067	950064435	9500	-0.3	84.23	2.44	0.07	111.75	19.27
J124836.31+294231.2	2457-54180-0112	950061614	8000	-0.39	5.36	2.19	0.11	—	—
J131702.34+281848.6	2243-53794-0533	950037259	9500	-0.21	64.31	2.27	0.01	45.18	3.15
J130535.77+283014.5	2242-54153-0447	950033645	24000	0.17	29.06	2.42	0.01	nov	—
J131544.04+262333.3	2243-53794-0170	950012628	12000	0.48	3.15	3.56	0.0	91.45	12.91
J125044.42+154957.3	1770-53171-0530	92124745	10000	-0.42	40.3	21.51	1.66	171.94	45.62
J115817.44+331719.2	2095-53474-0337	903794234	24000	0.11	4.1	2.03	0.0	23.64	0.86
J113804.15+305310.6	1974-53430-0023	903772636	16500	0.28	0.86	11.77	0.02	20.30	0.64
J113048.38+305720.6	1974-53430-0222	903763990	10000	-0.5	47.33	3.08	0.01	271.46	113.72
J114833.24+303921.2	2222-53799-0577	903752530	18000	0.32	42.73	2.65	0.24	—	—
J114529.26+300824.3	2222-53799-0483	903749706	15000	0.49	5.41	3.33	0.02	—	—
J114917.22+300016.0	2222-53799-0593	903746448	9000	-0.37	65.19	2.75	0.08	259.60	104.00
J113500.52+291206.5	2220-53795-0222	903738718	25000	0.03	2.3	2.02	0.01	1.92	0.01
J112439.29+262422.7	2216-53795-0143	903654707	10500	0.32	79.21	2.33	0.01	37.23	2.14
J113055.04+260115.6	2218-53816-0081	903652474	24000	0.0	33.47	2.4	0.01	nov	—
J113136.70+242122.8	6421-56274-0804	903643203	11500	-0.13	60.34	78.38	15.07	185.29	52.98
J104219.06+203008.7	5874-56039-0134	903602202	40000	0.03	46.61	128.98	100.74	175.40	47.48

SDSS name	PMF	TIC	$T_{eff}(K)$	z_{offset}	incl	B (MG)	dB (MG)	P(h)	dP(h)
J114246.50+205221.9	6432-56309-0563	903545771	10000	-0.11	57.33	74.76	10.78	nov	—
J113409.06+182238.7	5879-56047-0108	903504378	8500	-0.5	1.27	2.24	0.03	190.88	56.23
J111245.75+185719.5	2872-54533-0233	903486889	8500	-0.36	56.52	2.52	0.17	20.09	0.62
J111205.21+183200.2	2872-54533-0284	903486023	9000	-0.39	40.01	2.57	0.06	nov	—
J114827.96+153356.9	1762-53415-0372	903398755	16000	0.15	1.85	2.17	0.56	325.75	163.75
J115345.96+133106.6	1762-53415-0042	903388281	19000	0.0	33.47	2.45	0.0	258.20	102.88
J112148.80+103934.2	5371-55976-0512	903350099	17000	-0.12	86.65	311.79	61.86	—	—
J111812.67+095241.3	1222-52763-0477	903345358	14306	-0.3	54.84	2.27	0.05	—	—
J111608.80+092532.5	2413-54169-0151	903344952	8000	-0.19	17.69	1.4	0.06	—	—
J112328.48+095619.4	1222-52763-0625	903344183	9000	-0.3	63.16	2.25	0.05	—	—
J112605.90+090628.8	5371-55976-0258	903336248	10500	-0.19	9.25	32.12	42.07	—	—
J115554.94+083549.5	1622-53385-0447	903285329	9888	-0.46	59.81	3.04	0.1	322.76	160.76
J115418.14+011711.5	0515-52051-0126	903237515	18000	-0.31	79.1	37.35	13.8	—	—
J105055.04+143359.4	5355-56009-0532	903227550	15500	0.4	23.74	2.81	0.2	190.88	56.23
J104113.69+083505.2	1240-52734-0105	903193097	25000	0.48	3.98	4.04	1.33	—	—
J110735.31+085924.5	1221-52751-0177	903175194	18997	-0.26	56.98	2.64	0.08	—	—
J110341.38+053448.9	4855-55926-0376	903107849	10500	-0.33	72.64	16.41	2.81	—	—
J105709.81+041130.3	0580-52368-0274	903101941	8000	-0.34	41.45	2.77	0.19	—	—
J105332.61+020126.2	0507-52353-0113	903027044	8000	-0.36	42.75	2.54	0.11	—	—
J112059.67-001942.2	3838-55588-0064	902922409	19000	0.47	4.22	3.26	0.16	—	—
J113212.99-003036.8	0282-51658-0278	902915825	20000	0.04	21.79	3.19	0.46	—	—
J112852.88-010540.7	0326-52375-0565	902911171	18000	0.36	0.08	2.81	0.36	—	—
J114720.40-002405.7	0283-51584-0120	902887404	17000	0.0	33.47	2.0	0.0	—	—
J113839.49-014903.0	3775-55207-0698	902875212	9500	-0.15	62.9	24.33	5.06	—	—
J113431.97-031529.0	0327-52294-0131	902859737	15500	0.34	16.44	3.0	0.01	—	—
J111539.09-111350.6	2874-54561-0333	902303586	8000	-0.22	2.66	4.64	0.22	—	—
J112030.34-115051.1	2874-54561-0512	902291885	15500	-0.49	44.33	9.59	0.02	nov	—
J112216.02-122250.9	2874-54561-0071	902288119	13500	0.46	1.16	3.15	0.02	39.54	1.21

SDSS name	PMF	TIC	$T_{eff}(K)$	z_{offset}	incl	B (MG)	dB (MG)	P(h)	dP(h)
J104012.21+660520.1	0489-51930-0535	900624504	9500	-0.35	59.34	2.49	0.02	217.00	72.67
J111150.80+663736.2	0490-51929-0639	900620516	23000	0.0	33.47	5.5	0.0	—	—
J105628.48+652313.4	0490-51929-0205	900618725	18000	-0.1	54.56	23.21	0.01	1837.74	2605.93
J104356.63+650057.2	0489-51930-0079	900616508	18000	0.0	33.47	4.1	0.03	175.62	23.80
J112022.01+635437.4	0597-52059-0308	900591850	9500	0.47	6.99	3.24	0.69	152.53	17.95
J105404.37+593333.1	0561-52295-0008	900533657	15500	0.0	33.47	18.1	0.0	175.02	23.64
J111010.50+600141.3	2414-54526-0323	900530837	19500	-0.5	50.7	8.12	0.02	165.99	14.17
J114006.38+611008.1	0776-52319-0042	900517344	13000	-0.03	68.25	65.78	0.21	65.80	2.23
J115917.38+613914.2	7106-56663-0132	900512818	17000	-0.37	49.2	16.73	0.23	—	—
J110911.12+582209.3	2414-54526-0301	900497527	30000	0.23	37.43	2.95	1.02	67.71	2.36
J111528.74+570125.3	7100-56636-0430	900490689	23000	-0.25	72.44	2.19	0.34	172.10	15.24
J114152.02+572000.9	7092-56683-0812	900452169	11000	-0.23	52.09	2.49	0.01	190.58	14.01
J113357.65+515204.6	0879-52365-0586	900402242	22000	-0.35	80.0	9.67	1.55	nov	—
J105216.00+530120.3	1010-52649-0597	900382009	19500	0.18	0.05	2.44	0.05	—	—
J105328.13+505155.2	0876-52669-0510	900372338	9000	-0.44	56.93	2.82	0.02	nov	—
J105556.92+483652.4	2410-54087-0494	900361291	9500	-0.28	66.87	2.19	0.0	1.96	0.01
J105732.05+480125.9	2410-54087-0117	900355284	16000	-0.32	88.98	2.29	0.01	nov	—
J113408.25+485601.8	0967-52636-0319	900324793	40000	-0.41	60.03	2.77	0.07	nov	—
J112926.23+493931.8	0966-52642-0474	900321433	10000	-0.5	19.54	3.05	0.23	37.24	1.07
J115244.11+501844.5	6683-56416-0330	900305084	9500	-0.43	62.27	14.65	0.42	224.65	77.88
J104136.43+404317.8	1432-53003-0522	900244048	8000	-0.35	9.29	2.73	0.03	3.15	0.02
J110203.75+400558.0	1988-53469-0434	900228013	10000	0.13	0.01	2.11	0.03	—	—
J105833.57+372401.3	2091-53447-0464	900213503	9500	0.19	84.9	2.55	0.04	—	—
J112714.82+411737.6	1443-53055-0302	900178759	8000	-0.48	42.64	3.05	0.08	190.73	56.14
J114852.77+430753.1	1447-53120-0323	900173800	40000	0.24	6.23	2.3	0.0	183.00	51.68
J112014.62+400422.6	1980-53433-0630	900133584	10000	-0.36	72.97	2.54	0.01	54.29	4.55
J113114.44+355007.2	4618-55600-0022	900099937	12500	0.43	1.85	3.0	0.16	—	—
J112257.10+322327.7	1979-53431-0512	900083598	11500	-0.28	50.74	12.87	0.15	nov	—

SDSS name	PMF	TIC	$T_{eff}(K)$	z_{offset}	incl	B (MG)	dB (MG)	P(h)	dP(h)
J105152.18+321135.2	2026-53711-0183	900055750	20000	0.0	33.47	1.3	0.0	224.65	77.88
J104851.93+273817.6	2358-53797-0156	900020340	9000	0.14	28.23	2.03	0.02	217.16	72.78
J123414.11+124829.5	1616-53169-0423	87547997	8544	-0.5	1.88	2.26	0.58	106.81	17.61
J103648.66+171045.1	2593-54175-0131	842469335	9500	-0.13	78.82	2.19	0.01	74.88	8.65
J103002.66+163927.4	2592-54178-0417	842467182	22000	0.18	0.47	4.01	0.0	75.75	8.86
J102230.51+144646.8	2590-54175-0191	842452074	8500	0.15	1.04	2.22	0.03	—	—
J103336.57+105710.9	5346-55955-0628	842419765	8000	-0.31	2.62	24.1	9.9	—	—
J100715.55+123709.4	1745-53061-0313	842413869	23000	0.11	0.87	5.08	1.55	—	—
J101519.32+114724.1	1597-52999-0531	842403022	11500	-0.37	76.73	2.77	0.0	—	—
J101529.62+090703.7	1237-52762-0533	842363442	8000	-0.37	2.59	2.51	0.25	—	—
J100356.31+053825.6	4800-55674-0790	842330100	22000	0.11	31.31	163.51	18.08	—	—
J101420.37+060254.0	0996-52641-0025	842294079	19000	0.0	33.47	2.3	0.01	—	—
J101618.37+040920.5	0574-52355-0166	842277977	12500	0.17	30.28	4.05	0.06	142.02	7.78
J103430.15+032736.3	4772-55654-0128	842259458	11500	-0.28	65.82	13.28	1.87	—	—
J103724.11+013528.8	4734-55646-0298	842246240	10500	-0.5	14.07	3.73	2.38	10.71	0.18
J093508.56+042116.7	0569-52264-0452	842195465	19500	0.0	33.47	1.3	0.01	169.85	22.26
J094815.26+041648.6	0570-52266-0632	842180069	16500	0.36	0.16	3.3	0.18	nov	—
J094103.84+032835.8	0570-52266-0279	842162245	25000	0.0	33.47	1.8	0.0	20.41	0.16
J094711.11+003754.6	0480-51989-0082	842138864	9000	0.21	89.92	2.56	0.0	51.61	2.06
J092926.44+013535.6	4742-55660-0420	842123485	13000	-0.29	79.55	2.26	0.08	81.66	5.15
J092242.42+011422.8	0473-51929-0003	842120917	30000	-0.28	23.97	8.5	0.0	nov	—
J092527.46+011328.6	0475-51965-0315	842119542	10500	-0.47	56.99	3.05	0.08	102.80	8.15
J094012.88-000009.9	0476-52314-0597	842095343	24000	0.22	18.3	2.58	0.12	182.39	25.67
J093054.58-012642.9	3767-55214-0562	842088974	10500	-0.32	7.09	10.42	1.05	nov	—
J100005.66+015859.0	0500-51994-0557	842047663	17000	0.31	2.06	25.52	0.11	—	—
J101206.88+022003.1	0502-51957-0495	842043890	8000	0.19	20.12	2.2	0.01	nov	—
J100822.39+015307.4	0501-52235-0077	842039397	40000	0.47	4.24	3.85	0.0	70.43	7.65
J100732.63+010914.6	0501-52235-0004	842035424	9000	0.34	38.75	2.47	0.43	—	—

SDSS name	PMF	TIC	$T_{eff}(K)$	z_{offset}	incl	B (MG)	dB (MG)	P(h)	dP(h)
J094945.34+003619.1	0480-51989-0045	842026479	9500	0.38	0.33	3.0	0.0	105.97	8.66
J094416.62-001855.5	3827-55565-0472	841953843	8000	-0.28	17.5	3.77	0.02	43.66	1.47
J094026.71+631427.6	7447-56746-0198	841186228	11000	-0.36	72.9	2.81	0.18	nov	—
J093813.82+615600.8	2403-53795-0278	841182504	10500	0.22	8.34	2.49	0.01	nov	—
J103655.38+652252.0	7083-56722-0200	841177568	19500	-0.49	3.71	15.37	1.27	36.38	2.04
J102553.68+622929.1	7090-56659-0696	841159092	9000	-0.48	46.08	3.25	0.01	297.44	68.26
J094046.28+595415.8	0453-51915-0325	841143629	12000	0.21	2.05	2.04	0.0	86.82	11.63
J101400.72+594933.1	7087-56637-0772	841109114	8000	-0.23	6.85	1.9	0.04	nov	—
J095919.86+573542.9	0558-52317-0158	841101724	17500	0.15	7.35	5.08	0.02	—	—
J093921.25+581421.4	0452-51911-0553	841068454	21000	0.19	18.17	2.4	0.01	—	—
J092932.55+561318.4	0556-51991-0326	841061440	9000	0.18	7.67	2.26	0.38	188.97	55.11
J095211.45+563020.7	0557-52253-0170	841050295	22652	0.07	69.66	2.01	0.0	223.27	76.93
J095603.30+540907.0	0769-54530-0078	841038609	14000	0.05	4.99	3.51	0.01	37.85	2.21
J094210.10+521313.3	2404-53764-0058	841032611	8000	-0.39	49.68	2.57	0.14	117.05	21.14
J093447.89+503312.1	0901-52641-0373	841017982	8946	-0.1	41.23	6.61	0.52	nov	—
J100932.74+524638.2	0903-52400-0584	840981283	15122	-0.28	81.23	2.28	0.11	nov	—
J102746.58+435156.2	2567-54179-0306	840928345	9500	-0.15	74.41	2.11	0.03	nov	—
J093832.79+474050.6	7307-56720-0130	840884471	12500	-0.43	16.43	90.34	54.26	1.14	0.0020
J100657.97+484506.0	7329-56719-0825	840874386	9000	0.24	4.72	23.97	0.18	—	—
J094458.92+453901.1	1202-52672-0577	840851842	20000	0.16	63.31	15.42	0.08	nov	—
J094111.40+423921.2	4638-55956-0034	840805958	40000	0.49	59.24	3.48	0.02	8.97	0.12
J093409.90+392759.3	1215-52725-0241	840796904	10985	-0.49	50.0	3.08	0.13	nov	—
J101507.34+441507.8	4693-55632-0066	840766988	8000	-0.33	20.3	2.77	0.08	nov	—
J093411.36+364641.2	1275-52996-0174	840678901	10500	-0.29	59.76	2.23	0.06	nov	—
J093200.38+350429.8	10244-58225-0112	840667013	9500	-0.22	81.5	2.19	0.01	1.20	0.0022
J103635.00+391814.0	1430-53002-0078	840608665	8000	0.25	83.93	2.8	0.12	233.57	84.19
J101428.08+365724.5	1954-53357-0393	840599122	11000	-0.36	72.58	14.93	1.14	62.60	6.05
J101339.46+352639.6	1954-53357-0250	840592456	21000	0.07	5.78	2.21	0.91	262.20	106.09

SDSS name	PMF	TIC	$T_{eff}(K)$	z_{offset}	incl	B (MG)	dB (MG)	P(h)	dP(h)
J100657.51+303338.0	1953-53358-0415	840538665	10500	-0.5	35.94	3.23	0.07	—	—
J101847.14+304018.0	1956-53437-0143	840513174	30000	-0.49	50.98	3.05	0.04	272.50	114.59
J101834.81+303330.4	1956-53437-0197	840513148	21000	-0.32	72.28	2.7	0.61	2.54	0.01
J101642.26+281610.2	2348-53757-0040	840501753	25000	0.07	6.6	2.16	0.0	nov	—
J101059.21+284359.6	2348-53757-0485	840496085	19000	0.0	33.47	2.0	0.0	nov	—
J100727.32+281457.8	2348-53757-0279	840495362	11500	0.12	29.33	2.07	0.0	204.85	64.76
J103403.98+305034.4	2354-53799-0536	840478802	12500	0.27	1.27	2.77	0.02	—	—
J103935.51+295413.5	1969-53383-0215	840476369	14388	0.32	88.17	2.4	0.01	—	—
J102535.39+282034.8	2351-53772-0007	840472446	24000	-0.12	10.24	2.38	0.01	198.64	60.89
J102429.16+281435.4	2351-53786-0001	840469963	21000	-0.22	59.98	2.2	0.81	273.13	115.12
J102220.69+272539.8	2350-53765-0543	840468576	17000	0.42	17.63	8.23	0.93	1.74	0.0047
J101712.60+233646.6	6458-56274-0968	840443784	11500	-0.34	60.06	143.03	15.18	—	—
J103036.02+225011.4	6425-56298-0386	840431074	10000	-0.5	20.23	5.33	0.02	—	—
J103350.87+204729.3	2376-53770-0463	840418886	16500	-0.49	27.32	10.91	0.15	158.90	38.96
J093126.14+321946.1	1943-53386-0294	840407577	18000	0.28	0.89	12.95	0.06	—	—
J093415.96+294500.4	2914-54533-0162	840384454	40000	0.35	42.92	32.01	0.74	nov	—
J093654.94+262650.2	2294-54524-0617	840338593	23000	0.38	9.85	3.73	1.87	nov	—
J092355.96+243552.8	2291-53714-0552	840333882	17000	0.25	30.87	5.34	0.24	nov	—
J094235.02+205208.2	5786-56251-0182	840283353	15500	-0.18	62.95	62.79	26.23	nov	—
J092246.94+230812.6	2319-53763-0567	840276900	21000	0.2	57.24	2.61	0.02	1.77	0.0048
J092041.53+221545.4	2319-53763-0557	840275548	24000	-0.1	49.93	2.09	0.01	325.50	40.88
J093059.15+202429.3	2289-53708-0069	840260974	15000	0.43	16.14	3.19	0.39	—	—
J093726.27+205756.9	2361-53762-0408	840260630	18000	0.13	58.49	5.44	0.01	224.48	77.76
J094025.97+201707.2	2292-53713-0048	840251364	10500	0.0	33.47	2.0	0.01	—	—
J092524.25+175712.6	2360-53728-0217	840238169	17314	-0.26	81.68	2.0	0.01	—	—
J100426.98+223810.5	2343-53735-0300	840218506	10500	0.29	75.82	2.29	0.01	148.98	34.25
J095738.55+194601.8	2363-53763-0097	840194317	18000	0.14	8.03	2.09	0.0	nov	—
J102239.05+194904.2	2374-53765-0544	840175973	9000	-0.5	47.12	3.23	0.16	—	—

SDSS name	PMF	TIC	$T_{eff}(K)$	z_{offset}	incl	B (MG)	dB (MG)	P(h)	dP(h)
J100828.97+183633.4	2373-53768-0290	840167068	13000	0.17	2.09	2.38	0.0	—	—
J100758.24+163618.9	2585-54097-0024	840153475	11000	-0.31	79.19	2.27	0.05	—	—
J100759.80+162349.6	2585-54097-0030	840152969	32642	-0.12	40.83	13.02	9.31	—	—
J100645.00+144250.3	2586-54169-0479	840148762	12000	0.4	10.44	2.78	0.01	—	—
J092417.96+142238.2	5305-55984-0002	840119905	30000	0.11	4.05	2.38	0.13	—	—
J093431.10+132814.6	2580-54092-0273	840109755	34332	-0.24	62.35	2.13	0.02	—	—
J094004.19+123930.8	5318-55983-0468	840079716	8000	-0.28	63.18	2.19	0.03	—	—
J092108.83+130111.6	2577-54086-0448	840061732	20000	0.01	0.4	2.47	0.98	—	—
J093707.06+102149.1	5316-55955-0434	840040496	17500	0.43	42.94	394.67	127.88	—	—
J093356.39+102215.6	1303-53050-0525	840040122	9075	-0.38	54.9	2.58	0.23	—	—
J114441.65+171716.4	5892-56035-0686	82596432	23000	-0.2	11.84	2.15	0.21	270.42	112.85
J102054.10+362647.0	4568-55600-0952	8151705	13500	-0.2	52.99	61.2	12.02	168.08	43.60
J090855.40+010552.5	3818-55532-0906	804399274	8000	-0.33	48.63	3.0	0.02	24.34	0.46
J080638.50+075647.5	2076-53442-0521	804287964	21000	-0.26	56.26	2.11	0.69	nov	—
J081523.35+084346.4	2571-54055-0256	804272240	21000	0.17	0.41	5.17	0.02	157.33	19.10
J080719.89+064536.6	1756-53080-0234	804247326	21000	0.15	17.84	2.14	0.11	nov	—
J081144.59+071030.5	1756-53080-0585	804244757	17000	0.13	2.79	2.13	0.0	170.48	22.43
J080905.97+062441.7	2076-53442-0076	804237480	18000	0.18	87.64	2.25	0.09	0.33	0.0001
J082231.16+033113.7	1184-52641-0637	804053167	8000	-0.23	58.73	4.18	0.06	67.27	6.98
J081648.70+041223.5	1184-52641-0329	804038056	15000	0.0	33.47	11.1	0.0	nov	—
J081656.46+030417.0	4787-55863-0846	804020909	8000	-0.25	15.71	4.19	0.33	nov	—
J084155.73+022350.5	0564-52224-0248	803781707	8000	-0.28	9.81	3.67	0.23	165.83	42.44
J084906.22+003722.8	3813-55532-0364	803655578	14500	-0.45	64.16	18.27	4.4	nov	—
J083234.10-042813.7	2828-54438-0149	803218431	9500	0.35	5.97	7.9	0.0	—	—
J080620.12-075457.1	2827-54422-0307	802990973	9000	0.3	28.06	3.19	0.01	nov	—
J085550.69+824905.2	2549-54523-0066	802787535	32081	0.23	66.09	12.19	0.15	51.74	1.38
J083448.65+821059.0	2549-54523-0135	802780613	23000	-0.39	55.53	15.02	0.92	24.23	0.30
J085419.97+603701.6	5709-56571-0108	802385224	11000	-0.19	12.15	62.99	10.03	—	—

SDSS name	PMF	TIC	$T_{eff}(K)$	z_{offset}	incl	B (MG)	dB (MG)	P(h)	dP(h)
J085309.08+563441.5	0483-51924-0203	802348105	10000	0.0	33.47	1.1	0.03	165.53	42.28
J081632.25+522645.2	3689-55180-0826	802270970	8000	-0.4	0.39	2.19	0.36	—	—
J084937.77+561949.1	0483-51902-0296	802265153	15000	0.18	4.88	2.47	0.01	170.00	44.60
J083531.17+533230.8	2331-53742-0197	802256094	8000	-0.46	10.46	14.4	4.25	nov	—
J083051.14+503610.7	3694-55209-0966	802218669	16000	0.3	72.81	2.26	0.15	1.32	0.0027
J091015.08+520310.7	5732-56326-0864	802175706	19500	-0.28	29.69	2.41	0.12	nov	—
J090205.29+454915.5	5736-55984-0466	802108387	11000	-0.44	56.63	2.83	0.3	1.46	0.0033
J081136.33+461156.4	0439-51877-0523	802007438	40000	0.49	3.9	4.95	2.77	nov	—
J082159.66+431127.3	0547-52207-0019	801914894	22000	0.0	33.47	1.7	0.01	118.68	21.74
J082533.22+412400.1	0760-52264-0640	801893231	23000	0.08	9.63	2.27	0.0	1.92	0.01
J084226.97+374040.1	0864-52320-0524	801836127	9500	-0.36	60.38	2.78	0.21	180.83	50.46
J080743.33+393829.1	0545-52202-0009	801818052	20000	0.26	11.63	38.0	0.17	185.00	52.82
J080938.10+373053.8	0758-52253-0044	801808959	11398	-0.1	55.43	46.42	0.21	57.18	5.05
J081018.72+370010.9	0892-52378-0374	801796116	9556	-0.31	80.65	2.5	1.29	69.12	7.37
J082302.39+334534.1	4442-55532-0578	801727360	8000	-0.37	8.84	2.46	0.08	—	—
J081130.20+305720.4	0861-52318-0096	801687739	9000	-0.18	47.0	2.5	0.15	—	—
J091124.68+420255.8	4603-55999-0200	801629491	10500	-0.11	53.7	44.5	8.59	nov	—
J091856.12+411317.9	0938-52708-0413	801618550	9500	0.31	87.79	2.78	0.17	nov	—
J091314.47+410838.6	1200-52668-0079	801616959	19000	0.38	6.96	3.56	1.63	nov	—
J085403.30+361121.3	2400-53765-0291	801563441	10500	-0.35	82.77	2.57	0.17	—	—
J085130.57+353117.6	0934-52672-0080	801561809	8000	-0.07	15.82	2.5	0.21	nov	—
J090746.83+353821.5	1212-52703-0187	801540681	19000	0.25	5.87	19.13	0.13	nov	—
J090623.50+332108.0	1272-52989-0519	801510434	18500	0.47	4.08	3.25	0.02	98.15	14.87
J083446.91+304959.2	4449-55544-0876	801468633	11500	-0.36	85.31	2.56	0.1	271.25	113.54
J082239.54+304857.1	0931-52619-0078	801453567	17500	0.0	33.47	2.4	0.08	—	—
J082835.81+293448.6	1207-52672-0635	801440788	25000	0.15	36.11	33.43	0.17	—	—
J084541.11+312936.6	2960-54561-0009	801425120	12500	0.18	0.45	2.08	0.33	262.20	106.09
J084929.10+285720.3	1588-52965-0565	801402751	15500	0.17	12.57	28.0	0.77	nov	—

SDSS name	PMF	TIC	$T_{eff}(K)$	z_{offset}	incl	B (MG)	dB (MG)	P(h)	dP(h)
J084008.49+271242.6	1587-52964-0059	801376964	12500	-0.44	69.48	11.19	0.36	7.09	0.08
J090451.92+293755.0	10667-58163-0282	801345051	13000	-0.5	52.99	5.35	0.1	38.70	2.31
J085649.67+253441.0	5179-55957-0778	801299418	11500	-0.2	19.31	85.0	11.68	nov	—
J084936.81+224754.9	2085-53379-0131	801263440	25000	0.12	9.03	2.1	0.49	—	—
J091305.58+260748.5	2087-53415-0383	801258859	16000	0.18	19.84	2.3	0.0	nov	—
J090937.94+250820.6	2086-53401-0582	801256984	10500	-0.39	50.91	2.52	0.1	7.09	0.08
J091002.83+232219.9	2287-53705-0470	801241737	21000	-0.03	18.84	2.28	0.56	80.93	10.11
J091310.43+230042.6	2287-53705-0541	801240056	23000	0.08	4.79	2.1	1.2	45.21	0.79
J091132.79+223200.6	2287-53705-0169	801238746	11500	0.4	0.4	3.07	0.01	nov	—
J090554.63+213829.5	2284-53708-0103	801217912	30000	0.0	33.47	2.1	0.06	—	—
J090522.06+205736.2	2284-53708-0091	801216574	19000	0.13	52.9	2.21	0.73	—	—
J082141.04+264800.7	11125-58433-0906	801179353	15500	-0.43	50.15	3.02	0.18	—	—
J080724.47+260238.3	11121-58438-0361	801160218	22000	-0.25	27.61	8.19	0.05	—	—
J083051.08+244615.7	2330-53738-0503	801105047	11000	-0.31	81.05	2.29	0.01	—	—
J083310.56+234812.7	2330-53738-0109	801100122	10500	0.44	17.77	3.0	0.0	—	—
J081819.51+225349.9	4468-55894-0368	801081630	35245	0.36	89.04	2.54	0.21	—	—
J081354.17+223713.6	4469-55863-0047	801080259	21000	0.36	77.38	15.52	2.46	—	—
J080502.28+215320.5	1584-52943-0132	801073734	37141	-0.49	66.27	6.77	0.17	—	—
J081716.39+200834.9	2082-53358-0444	801043807	8000	-0.28	9.66	3.78	0.21	—	—
J080150.49+205012.0	1583-52941-0599	801034661	19000	0.17	22.86	2.18	0.0	—	—
J080440.35+182730.9	2081-53357-0442	801004940	10135	-0.12	16.04	38.26	25.56	—	—
J083918.12+212143.7	2084-53360-0100	800959805	13500	0.0	33.47	3.4	0.0	—	—
J083613.81+201852.1	2275-53709-0526	800953957	9500	-0.33	71.7	2.96	0.02	—	—
J083945.55+200015.7	4484-55565-0072	800953040	15500	-0.27	59.18	2.72	0.26	—	—
J083041.77+204233.7	2083-53359-0553	800945431	17500	-0.19	77.75	2.19	0.06	—	—
J082107.34+194433.6	2082-53358-0617	800939394	25000	0.0	33.47	1.3	0.0	—	—
J083020.35+185814.5	4489-55545-0678	800922014	20000	-0.3	80.38	2.27	0.01	—	—
J082817.60+181752.6	2275-53709-0298	800913435	13000	0.13	31.43	2.19	0.01	—	—

SDSS name	PMF	TIC	$T_{eff}(K)$	z_{offset}	incl	B (MG)	dB (MG)	P(h)	dP(h)
J084845.65+214047.0	2280-53680-0446	800908416	24000	0.37	17.55	3.43	1.14	—	—
J084330.81+201049.1	5176-56221-0564	800898084	25000	-0.42	0.02	21.52	2.13	—	—
J085129.15+195205.4	2280-53680-0018	800887135	9500	-0.42	75.49	3.0	0.02	—	—
J083623.85+163859.6	2278-53711-0270	800840127	11000	-0.38	53.83	2.58	0.11	—	—
J083627.34+154850.3	2276-53712-0107	800836298	30000	0.5	3.75	5.03	4.59	—	—
J083701.89+154454.6	2276-53712-0004	800835990	17000	0.43	8.66	3.0	0.01	—	—
J083438.28+153817.5	2427-53815-0321	800835737	16500	0.28	0.08	5.59	0.0	—	—
J084111.34+154921.0	2429-53799-0358	800833697	19000	0.25	43.13	2.65	0.0	—	—
J084201.41+153941.8	2429-53799-0363	800833464	20000	0.25	81.62	18.12	0.01	—	—
J081748.55+154341.1	2272-53713-0386	800780374	11000	0.0	33.47	1.8	0.0	—	—
J080210.39+153033.8	2266-53679-0534	800767420	19000	0.11	19.88	2.01	0.01	—	—
J080703.25+135537.8	2268-53682-0472	800739322	20000	0.02	3.97	2.81	0.25	139.22	14.96
J080359.93+122943.9	2265-53674-0033	800719597	12347	-0.35	16.97	33.29	4.86	185.93	26.67
J082447.49+131543.2	2422-54096-0588	800676726	22000	0.0	33.47	1.7	0.23	—	—
J081216.23+131708.2	4505-55603-0987	800664052	18000	0.23	4.15	2.66	0.24	167.06	21.53
J091629.56+215011.4	2319-53763-0236	800598612	8000	-0.15	24.48	6.19	0.2	—	—
J091833.32+205536.9	2319-53763-0209	800597027	15584	-0.28	75.5	2.55	0.42	—	—
J091326.64+211250.4	2288-53699-0332	800593326	15500	0.26	84.06	2.23	0.01	—	—
J091526.57+205039.1	2288-53699-0468	800592616	11000	0.11	33.14	2.05	0.02	—	—
J090907.15+193840.6	2286-53700-0176	800586645	14000	0.43	27.95	2.99	0.01	—	—
J091305.88+173932.9	2439-53795-0357	800572312	17500	0.36	0.18	2.76	0.15	—	—
J085523.86+164058.9	5292-55926-0186	800548317	12000	-0.44	20.88	11.04	0.58	—	—
J085153.78+152724.9	2431-53818-0238	800524408	10000	-0.15	65.59	26.97	9.86	—	—
J084522.94+150020.3	2429-53799-0152	800519972	18000	0.17	22.64	2.03	0.02	—	—
J085820.01+103725.4	5291-55947-0999	800433393	20000	0.09	17.15	2.14	0.55	nov	—
J083420.29+131759.5	2426-53795-0387	800424680	21000	0.11	2.73	4.5	0.01	—	—
J084039.36+125706.2	2428-53801-0354	800420766	12000	0.17	0.37	2.22	0.01	—	—
J084219.70+122128.3	2428-53801-0221	800402963	20000	0.12	13.71	2.04	0.66	—	—

SDSS name	PMF	TIC	$T_{eff}(K)$	z_{offset}	incl	B (MG)	dB (MG)	P(h)	dP(h)
J084510.22+112405.6	2428-53801-0089	800394952	16000	0.15	12.4	2.17	0.08	71.75	3.97
J083656.62+103452.1	5284-55866-0690	800385070	17000	0.1	47.85	2.07	0.14	nov	—
J082939.24+100937.7	2572-54056-0399	800350281	22000	-0.21	81.09	2.69	0.71	10.61	0.17
J082239.43+082436.7	1758-53084-0346	800333010	10500	-0.35	69.08	2.57	0.18	nov	—
J083002.71+083631.9	1758-53084-0531	800329826	12500	0.44	18.55	3.01	0.0	nov	—
J084233.36+101806.3	2573-54061-0141	800310802	12284	0.35	77.36	2.78	0.01	73.43	4.16
J084011.39+094244.8	2573-54061-0130	800308377	9500	0.2	5.3	2.19	0.01	nov	—
J084253.04+092226.5	1759-53081-0618	800303146	11500	0.05	5.39	3.4	0.08	nov	—
J083801.80+092548.3	2573-54061-0246	800278677	23000	0.44	1.37	3.77	0.13	nov	—
J084628.04+064532.8	1189-52668-0344	800242069	23000	0.0	33.47	1.3	0.0	152.95	36.10
J083745.12+064313.8	1297-52963-0637	800237984	30000	0.39	15.76	4.76	0.35	nov	—
J091611.06+124808.0	2577-54086-0427	800223030	22000	-0.1	8.54	2.12	0.41	—	—
J091340.18+114112.3	2576-54086-0029	800219866	17500	0.18	11.19	2.19	0.04	—	—
J091239.63+102645.7	5302-55896-0230	800208106	16000	0.44	11.6	3.1	0.06	—	—
J090150.74+091211.4	1738-53051-0002	800202984	11000	-0.35	55.18	2.67	0.12	nov	—
J090827.08+092100.2	5299-55927-0834	800200985	40000	0.14	64.68	46.5	28.29	nov	—
J091220.25+075537.7	1301-52976-0241	800184130	15500	0.19	20.22	2.3	0.29	44.38	1.52
J085841.78+074728.3	5294-55922-0180	800165060	18000	0.25	0.0	2.52	0.0	117.60	10.67
J090632.65+080715.9	1300-52973-0148	800152213	40000	-0.35	29.15	7.55	0.18	155.55	18.67
J084910.12+044528.7	1188-52650-0635	800102412	15000	0.35	6.48	2.49	0.0	153.12	36.18
J091437.35+054453.3	1193-52652-0481	800074212	23420	-0.08	66.59	9.23	8.77	nov	—
J090343.13+011846.3	0470-51929-0403	800004414	11000	0.0	33.47	3.1	0.12	nov	—
J064607.86+280510.0	2694-54199-0175	764255582	19500	-0.31	65.18	2.28	0.06	—	—
J064532.74+280330.4	2694-54199-0201	764255158	11351	0.0	33.47	2.3	0.0	—	—
J075816.63+121428.6	2265-53674-0199	760500838	10000	-0.35	71.82	2.5	0.03	158.22	19.32
J075704.00+085519.9	2945-54505-0148	760311985	22000	0.0	33.47	1.6	0.14	157.06	38.07
J064828.77+840340.8	2548-54152-0616	743745856	11500	-0.17	53.66	3.73	0.01	nov	—
J074403.80+495439.9	1868-53318-0410	742724120	36390	-0.48	50.36	2.99	0.04	136.74	28.85

SDSS name	PMF	TIC	$T_{\rm eff}(K)$	z_{offset}	incl	B (MG)	dB (MG)	P(h)	dP(h)
J073741.49+470421.1	3665-55247-0394	742543722	23000	0.49	3.55	3.59	0.66	10.90	0.18
J073341.55+435348.0	5942-56210-0336	742487127	11500	-0.15	65.31	46.57	7.9	nov	—
J071410.25+401219.4	2943-54502-0612	742170275	18000	0.15	88.78	2.35	0.01	—	—
J071632.91+393553.8	3655-55240-0488	742161261	17000	0.22	87.6	2.44	0.3	4.84	0.04
J073615.91+403335.0	3658-55205-0062	741617118	8000	-0.27	14.46	3.79	0.19	nov	—
J075842.68+365731.5	0757-52238-0439	741534559	8000	0.0	33.47	1.1	0.06	1.17	0.0021
J075819.57+354443.6	0757-52238-0144	741532201	15000	-0.4	20.02	25.68	5.71	1.38	0.0029
J072724.65+403622.4	2701-54154-0301	741520490	10500	-0.37	72.98	2.81	0.13	nov	—
J073237.67+364628.8	2073-53728-0571	741461162	20000	-0.03	69.82	108.72	28.0	nov	—
J073001.65+362713.2	2073-53728-0482	741459452	10000	0.33	84.48	2.77	0.02	nov	—
J073135.36+353108.5	2073-53728-0108	741351877	24000	0.03	1.96	2.05	0.0	76.71	9.08
J074947.00+354055.4	0542-51993-0639	741333532	39100	0.23	6.68	30.0	0.16	nov	—
J072540.81+321402.1	2695-54409-0564	741278115	24000	0.29	57.89	15.15	0.88	69.12	7.37
J065133.33+284423.3	2694-54199-0528	741030076	17841	0.15	8.36	2.16	0.09	—	—
J071814.18+305148.8	2695-54409-0268	740990019	12000	0.47	5.48	3.19	3.33	86.16	11.46
J074213.39+315703.8	4443-55539-0256	740755022	9000	-0.16	11.24	41.4	25.36	72.30	8.07
J074853.07+302543.5	0889-52663-0507	740717798	28932	0.02	35.96	8.15	1.46	224.65	77.88
J073819.64+282126.9	10285-58083-0155	740703585	8000	-0.34	60.56	2.73	0.17	165.53	42.28
J074327.09+273732.4	2075-53730-0278	740666205	9500	-0.31	69.75	2.28	0.05	41.93	0.68
J074224.66+232804.1	4470-55587-0200	740377685	14000	-0.35	55.65	2.84	0.28	—	—
J075036.54+222021.4	2916-54507-0133	740235307	21000	0.08	33.22	2.08	0.0	—	—
J073953.17+204900.2	2079-53379-0051	740190881	22000	0.11	15.63	2.01	0.03	—	—
J074047.65+180907.3	2074-53437-0237	740127578	23000	0.0	33.47	1.7	0.36	—	—
J075234.95+172524.9	2729-54419-0171	740081291	9000	-0.31	48.59	12.68	1.17	—	—
J074924.91+171355.3	2729-54419-0282	740067835	18500	-0.39	57.16	14.95	0.41	—	—
J074958.58+161120.2	2080-53350-0349	740035460	24000	0.03	5.77	2.09	0.0	—	—
J074907.48+154534.1	4495-55566-0435	740033469	22000	-0.25	73.24	2.09	0.08	—	—
J052831.02+005244.3	2072-53430-0336	713047979	16444	0.24	62.18	2.57	0.05	94.04	6.82

SDSS name	PMF	TIC	$T_{eff}(K)$	z_{offset}	incl	B (MG)	dB (MG)	P(h)	dP(h)
J053016.83-001034.4	2072-53430-0233	713010861	19000	0.18	0.32	2.34	0.02	78.07	4.70
J053507.04+001617.0	2072-53430-0508	713007995	18000	0.17	41.67	2.42	0.01	nov	—
J053317.32-004321.9	2072-53430-0096	712998752	40000	0.27	7.72	16.89	0.58	20.65	0.33
J060442.48+641357.1	2301-53712-0476	704998888	13000	-0.44	18.59	20.75	0.89	nov	—
J055814.96+643826.5	2301-53712-0344	702897102	12000	0.44	8.97	3.0	0.0	—	—
J053400.83+625419.7	2302-53709-0579	702868694	8000	0.13	62.91	2.19	0.02	108.15	18.05
J044254.59+120329.8	2669-54086-0377	673331871	8000	-0.34	56.07	33.72	14.03	nov	—
J044641.49+101510.9	2673-54096-0049	673244460	8000	-0.29	57.95	2.17	0.16	126.19	12.29
J041209.32-054031.0	0465-51910-0017	671944105	12000	-0.22	6.48	32.61	0.23	nov	—
J044512.39-052524.5	2942-54521-0487	671896256	18000	0.24	5.82	2.68	0.28	1.29	0.0013
J040054.81-064625.2	2071-53741-0014	671844707	20000	0.18	9.89	4.39	0.34	1.69	0.0044
J045016.37-053847.8	2942-54521-0637	671765265	40000	0.16	2.94	2.15	0.01	—	—
J025001.76-043703.1	7054-56575-0438	652010324	19000	0.15	42.5	309.41	38.57	122.03	22.98
J025506.13-071551.4	7059-56592-0652	651979835	8000	-0.28	6.99	9.0	1.41	342.41	90.47
J032404.30-061756.5	0460-51924-0525	651942038	8000	-0.5	43.37	3.03	0.31	—	—
J031630.64-081529.1	0459-51924-0002	651936432	9500	-0.23	65.04	2.19	0.01	nov	—
J035010.32+085829.1	2697-54389-0048	649929311	14500	0.16	0.27	2.02	0.01	67.00	6.93
J032628.17+052136.2	2339-53729-0515	649883787	16000	-0.49	20.38	15.95	0.52	—	—
J032658.77+040307.9	2339-53729-0046	649879308	13000	-0.42	68.94	2.82	0.21	166.51	21.39
J034511.10+003444.2	0416-51811-0590	649819568	8000	-0.36	12.91	2.5	0.27	208.28	33.47
J032137.43+010437.3	0413-51821-0578	649800430	18000	0.05	16.68	2.86	0.0	nov	—
J032300.93+002221.4	0712-52199-0427	649797616	14500	0.0	33.47	2.7	0.0	174.33	46.90
J030647.72+010949.8	2068-53386-0401	649795919	16000	0.3	22.83	3.08	0.09	108.11	9.02
J030407.39-002541.9	2048-53378-0280	649789635	9500	-0.07	49.81	10.48	1.37	—	—
J030417.87-003216.4	0709-52205-0107	649789588	14000	0.49	12.73	4.29	2.77	213.56	35.19
J031323.65-001659.9	0413-51929-0313	649786561	30000	0.42	0.0	7.3	0.0	210.40	68.32
J031637.81-003310.9	3183-54833-0179	649784589	9000	-0.3	9.35	2.0	0.17	—	—
J033145.69+004516.9	0415-51879-0378	649774436	12000	-0.42	48.36	13.05	2.37	—	—

SDSS name	PMF	TIC	$T_{\rm eff}(K)$	z_{offset}	incl	B (MG)	dB (MG)	P(h)	dP(h)
J034308.17-064127.3	0462-51909-0117	649655898	12000	-0.5	20.09	11.43	0.0	nov	—
J034240.63-073504.0	0462-51909-0084	649651309	19500	0.06	5.54	2.13	0.64	nov	—
J025837.19+000019.2	0410-51877-0065	649601258	10000	0.16	2.51	2.33	0.01	nov	—
J031824.19+422651.0	2417-53766-0568	642660784	8500	0.03	44.11	8.48	0.99	104.02	16.70
J031929.01+410316.9	2417-53766-0064	642629029	10000	0.46	1.01	3.15	0.0	188.23	54.68
J030158.92+372204.2	2443-54082-0190	641504653	12500	0.4	14.86	3.0	0.09	89.62	12.39
J030432.88+365537.8	2443-54082-0137	641502017	18500	-0.04	13.32	2.2	0.01	142.07	31.15
J024903.01+332737.0	2398-53768-0313	641418835	9500	-0.26	85.98	2.66	0.02	124.25	23.82
J030913.96+373057.9	2443-54082-0030	641409601	19000	0.0	33.47	2.3	0.02	124.15	23.79
J030550.34+370759.1	2443-54082-0154	641408620	10500	0.36	0.04	3.0	0.02	nov	—
J024241.66+291608.2	2444-54082-0604	641232340	12000	0.5	10.53	3.36	0.05	166.86	42.97
J024505.94+282542.7	2444-54082-0623	641215634	8000	-0.15	7.55	1.4	0.05	291.00	130.68
J030107.56+053956.9	2322-53727-0136	640056186	18000	-0.17	58.18	2.29	0.05	138.74	14.85
J031058.73+045129.9	2340-53733-0165	640031933	9000	-0.27	80.11	2.55	0.03	208.42	33.52
J030522.15+050213.3	2322-53727-0024	640031028	13500	0.43	9.01	2.95	0.67	85.20	5.60
J023609.43-080823.7	0455-51909-0474	632608446	10500	0.29	11.01	34.0	0.12	88.43	6.03
J012646.78+193454.5	5135-55862-0886	630638900	8000	-0.09	52.27	2.22	0.13	72.23	8.05
J013920.54+152218.7	0426-51882-0524	630603458	18000	0.19	0.56	2.3	0.0	—	—
J013533.20+132249.8	0426-51882-0291	630595680	21000	0.0	33.47	5.1	0.01	—	—
J012215.76+082712.7	2329-53725-0370	630560994	8000	-0.36	82.14	2.57	0.02	—	—
J014032.41+090520.3	11070-58452-0012	630527495	10500	0.46	22.12	4.25	0.33	—	—
J021107.71+072235.4	2321-53711-0409	630414292	14000	0.28	28.13	2.19	0.01	—	—
J021338.51+053023.3	2321-53711-0125	630404165	8500	-0.29	67.74	2.42	0.02	185.50	26.55
J021818.18+035525.3	4264-55506-0408	630364504	8000	-0.36	20.28	2.46	0.01	nov	—
J014230.56+003502.7	1907-53315-0427	630327182	13000	0.36	20.9	2.57	0.02	212.89	69.94
J020514.52+003100.3	2866-54478-0603	630309831	18000	0.22	3.5	2.42	0.03	nov	—
J015748.19-010600.9	0701-52179-0291	630305196	8000	0.22	1.98	2.73	0.01	1.01	0.0016
J021116.37+003128.2	4235-55451-0850	630304345	9000	-0.24	8.18	31.06	8.84	nov	—

SDSS name	PMF	TIC	$T_{eff}(K)$	z_{offset}	incl	B (MG)	dB (MG)	P(h)	dP(h)
J014938.34-004938.0	0699-52202-0012	630294939	16000	0.48	4.02	3.26	0.01	87.33	11.77
J020002.57-020542.3	4349-55803-0892	630285038	8000	-0.33	38.09	2.77	0.32	nov	—
J022335.15+004954.8	0406-51900-0490	630263660	9500	-0.15	65.68	2.16	0.02	352.35	95.80
J022523.67+002743.0	0406-51900-0543	630261777	15500	0.16	0.16	2.02	0.0	nov	—
J022623.80-002313.1	0406-52238-0071	630251962	16500	0.0	33.47	1.3	0.12	196.93	29.92
J012516.68-101313.7	2878-54465-0269	630101832	11500	0.25	0.04	2.61	0.02	—	—
J012339.94+405241.9	2063-53359-0403	622646714	50000	0.0	33.47	4.6	0.04	230.58	82.05
J012105.53+393239.7	2062-53381-0337	622638255	21640	-0.14	70.73	2.09	0.0	199.84	61.63
J012815.71+391130.1	2063-53359-0063	620916949	17000	0.11	2.86	2.05	0.02	—	—
J012115.44+321010.3	2061-53711-0506	620776739	23000	0.02	5.59	2.96	0.41	164.86	41.94
J013314.21+235247.4	2064-53341-0343	620514761	40000	-0.17	37.96	9.0	0.1	58.77	5.33
J013742.53+235138.2	2064-53341-0491	620514236	11500	0.37	0.24	3.0	0.04	108.52	18.17
J013909.14+230844.9	2064-53341-0163	620504992	15500	0.45	3.62	3.33	0.0	—	—
J014313.18+231524.5	2064-53341-0024	620504261	22000	0.4	7.55	3.0	0.0	—	—
J023420.62+264801.6	2399-53764-0559	620389451	40000	-0.02	13.13	30.78	3.45	182.50	51.40
J023157.00+264837.5	2399-53764-0426	620388909	9500	-0.19	70.17	2.29	1.57	236.04	85.98
J023445.31+260553.1	2399-53764-0487	620384192	13000	0.04	5.79	6.65	1.37	224.61	19.46
J023035.63+250831.5	2399-53764-0164	620305187	8000	-0.25	16.87	4.19	0.17	171.61	45.45
J023542.72+241653.7	2399-53764-0030	620300982	9500	0.17	85.49	2.33	0.0	128.55	25.50
J023449.24+240750.2	2399-53764-0070	620300898	8000	-0.29	15.23	3.59	0.16	142.44	31.31
J020316.65+220527.2	2066-53349-0302	620254501	11000	0.19	0.33	2.42	0.01	12.21	0.23
J021230.00+122557.2	0428-51883-0046	620058517	15500	0.14	0.8	2.07	0.11	—	—
J001034.94+245131.2	2822-54389-0025	611706334	10500	-0.32	57.32	11.8	0.3	—	—
J000701.59+240744.8	2822-54389-0042	611697567	8000	-0.3	64.61	2.27	0.01	—	—
J004038.89+243852.7	2058-53349-0195	611604244	10500	-0.36	78.46	2.52	0.01	213.57	70.39
J004254.23+235831.5	2058-53349-0087	611562641	10500	0.18	10.42	2.03	0.01	—	—
J002128.59+150223.7	0753-52233-0432	611416113	9000	-0.46	20.21	76.49	77.59	—	—
J011423.35+160727.6	5139-55866-0410	611338164	22000	0.06	46.94	22.97	13.33	83.12	10.66

SDSS name	PMF	TIC	$T_{eff}(K)$	z_{offset}	incl	B (MG)	dB (MG)	P(h)	dP(h)
J003232.07+153126.6	0418-51817-0346	611303961	17000	0.1	15.36	2.0	0.78	—	—
J003111.75+134919.5	0417-51821-0084	611288072	21000	0.15	0.72	2.24	0.0	—	—
J010311.32+151110.0	5131-55835-0578	611271506	11000	-0.42	67.41	2.81	0.16	43.13	2.87
J010405.12+145907.3	5131-55835-0438	611271319	10500	0.31	89.97	2.78	0.2	42.52	2.79
J004513.88+142248.1	0419-51879-0147	611261863	8000	-0.29	18.68	3.61	0.04	61.17	5.77
J001112.41+155209.5	6178-56213-0312	611224216	15000	0.5	2.61	3.38	0.02	—	—
J003223.65+082329.5	2327-53710-0321	611128619	11000	-0.31	47.14	2.19	0.01	—	—
J000603.80+075514.4	4534-55863-0248	611100360	9000	-0.47	43.92	12.94	9.04	—	—
J011130.67+141049.7	2825-54439-0089	611052262	19000	0.32	2.27	3.3	0.84	162.03	40.52
J004011.48+070255.6	2327-53710-0074	610957295	12000	0.42	8.42	3.12	0.06	—	—
J004528.87+004616.4	4223-55451-0634	610885485	19500	-0.26	61.77	2.19	0.08	—	—
J004248.20+001955.2	0690-52261-0594	610831323	14000	0.37	23.32	8.5	0.19	—	—
J010225.13-005458.6	0693-52254-0099	610770232	22000	-0.01	2.89	2.7	0.55	202.29	63.15
J004148.05-005127.3	1905-53706-0253	610735195	22000	0.48	1.4	4.39	1.69	—	—
J010654.65-104315.1	0659-52199-0207	610594367	8500	-0.19	54.68	2.81	0.22	—	—
J000825.77-054122.3	7035-56568-0241	610534482	30000	-0.35	77.82	2.58	0.08	59.94	5.54
J004122.49-110432.5	0655-52162-0091	610395316	8000	-0.37	11.19	2.44	0.27	nov	—
J010214.99+462620.9	1472-52913-0278	600706639	8033	-0.38	53.48	2.58	0.15	158.65	38.84
J011739.82+242236.2	2060-53706-0086	600006779	10000	-0.28	75.24	2.41	0.04	77.86	9.36
J021205.31+064420.5	7256-56658-0740	471014169	19000	-0.44	8.65	34.0	22.68	207.48	33.22
J034630.98+094827.4	2679-54368-0225	471014106	19500	0.32	89.23	2.79	0.33	—	—
J091005.44+081512.2	1300-52973-0639	471014089	30000	0.11	2.24	2.42	1.29	153.41	18.16
J085106.12+120157.8	2430-53815-0229	471014011	10000	-0.3	68.87	2.28	0.43	—	—
J000555.90-100213.5	7167-56604-0030	471013862	25000	-0.5	40.47	8.3	0.9	314.17	152.32
J080359.93+122943.9	4505-55603-0384	471013666	17500	-0.33	30.89	34.76	8.7	185.93	26.67
J034314.34+102938.3	2679-54368-0356	471013547	40000	-0.5	37.73	8.57	4.02	—	—
J033320.37+000720.6	0415-51879-0485	453828065	9500	0.18	0.1	771.71	214.35	111.83	9.65
J080527.55+073534.4	2056-53463-0557	443854829	8000	0.0	33.47	1.1	0.05	134.99	14.06

SDSS name	PMF	TIC	$T_{eff}(K)$	z_{offset}	incl	B (MG)	dB (MG)	P(h)	dP(h)
J113215.38+280934.3	2219-53816-0329	405494130	8000	-0.33	9.0	2.77	0.16	nov	—
J151625.06+280320.9	1846-54173-0280	357441103	8000	0.0	33.47	2.3	0.07	166.97	43.02
J101805.04+011123.4	0503-51999-0244	345036441	11000	0.01	65.25	122.69	15.97	—	—
J021148.21+211548.2	2046-53327-0048	306449009	12986	-0.31	36.45	167.11	41.51	58.15	5.22
J155857.68+041704.8	1837-53494-0261	272967708	8000	-0.16	9.63	69.82	15.31	—	—
J155620.60+055029.4	1822-53172-0139	272916891	8000	0.27	18.87	42.0	0.01	—	—
J170751.91+353239.4	4988-55825-0107	21831234	18000	-0.38	53.27	2.64	0.43	150.61	17.50
J085830.85+412635.0	0830-52293-0070	21402652	8000	-0.08	45.68	2.2	0.08	nov	—
J235318.56+380913.2	1883-53271-0050	2054409864	11500	-0.32	70.42	2.39	0.12	171.28	45.27
J235431.39+365019.1	1881-53261-0512	2054361413	10500	-0.24	73.86	3.0	0.01	153.72	36.47
J235503.83+350659.7	1881-53261-0042	2054346222	22000	0.29	0.18	2.84	0.01	138.49	29.60
J234858.29+253519.0	6518-56567-0796	2054043826	15500	-0.5	33.38	7.68	0.78	—	—
J224602.81+230704.1	2261-53612-0559	2053790571	15500	0.18	0.34	2.06	0.06	—	—
J224829.60+223355.9	2261-53612-0075	2053788238	10000	-0.32	0.64	37.11	3.43	—	—
J224912.31+220910.4	6120-56206-0747	2053782605	17500	-0.28	84.78	2.14	0.07	—	—
J233958.11+154419.8	6138-56236-0466	2053496902	10000	-0.05	49.87	3.15	0.0	—	—
J231940.37+140121.1	6142-56219-0110	2053409065	17500	0.43	18.05	3.0	0.07	—	—
J232136.69+133133.5	6142-56219-0001	2053407857	10500	-0.38	56.25	2.57	0.13	—	—
J233052.97+143037.5	6143-56267-0900	2053404082	23000	-0.46	9.02	17.5	1.62	—	—
J233817.93+083732.6	6161-56238-0622	2053214277	10500	-0.38	7.12	118.33	62.08	—	—
J224741.46+145638.7	5040-56243-0482	2053135939	18000	0.21	28.92	515.09	72.32	—	—
J224103.29+132853.2	0739-52520-0143	2053125574	23000	0.16	27.51	2.15	0.0	—	—
J225726.05+075541.6	2310-53710-0420	2053017544	9500	-0.44	40.16	17.4	9.54	—	—
J232353.30+060715.7	11294-58451-0284	2052928201	8000	0.06	60.4	15.12	0.1	—	—
J231951.71+010908.7	0382-51816-0565	2052885574	8000	-0.15	25.84	2.4	0.2	—	—
J225230.63+003232.6	0676-52178-0481	2052856351	30000	0.49	10.01	5.2	1.99	—	—
J224707.31+010058.5	1901-53261-0564	2052850399	11000	-0.29	75.73	2.19	0.01	—	—
J224742.57-003317.4	0676-52178-0319	2052844604	30000	0.5	3.81	5.13	25.63	—	—

SDSS name	PMF	TIC	$T_{eff}(K)$	z_{offset}	incl	B (MG)	dB (MG)	P(h)	dP(h)
J230904.69+001803.0	0678-52884-0547	2052824979	8000	-0.42	67.79	2.98	0.06	—	—
J230758.83+000500.4	0678-52884-0498	2052823804	22000	0.08	14.96	3.12	0.01	—	—
J232248.21+003901.0	0383-51818-0421	2052760353	11500	-0.38	33.3	21.2	0.49	—	—
J233328.29-002036.6	0682-52525-0317	2052750847	11000	0.0	33.47	2.7	0.01	—	—
J234710.26+000633.4	0683-52524-0520	2052735985	9500	0.39	5.76	6.0	0.1	—	—
J231432.89-011320.3	0382-51816-0289	2052699825	18500	0.45	4.02	4.5	0.0	—	—
J234623.68-102356.9	0648-52559-0142	2052378601	9500	-0.32	13.84	3.0	0.07	159.78	19.70
J232937.54+524437.8	1663-52973-0119	2044359015	32204	-0.31	74.89	2.24	0.05	144.64	16.14
J233708.96+492532.0	1889-53240-0584	2042663937	9500	-0.28	74.99	2.08	0.12	166.25	42.65
J233039.03+500729.6	1889-53240-0377	2042580607	14500	0.0	33.47	1.2	1.26	164.43	41.72
J235107.47+403453.9	1883-53271-0521	2040871405	15000	0.2	16.55	2.65	0.06	19.72	0.60
J234605.44+385337.6	1883-53271-0272	2040794854	14500	-0.34	4.71	45.0	8.92	151.11	17.62
J225338.68+301803.4	2627-54379-0021	2040231370	23000	0.14	12.68	2.01	0.01	—	—
J224854.51+303845.5	2627-54379-0152	2040211267	22000	0.49	3.58	4.05	1.93	—	—
J225828.48+280828.8	6293-56561-0264	2040069325	10500	-0.35	44.67	137.09	33.81	—	—
J212143.07-060005.7	2320-54653-0445	2029415809	25075	-0.1	53.26	1.94	0.03	—	—
J212514.18-062152.5	2320-54653-0612	2029410609	17000	0.15	4.36	2.1	1.39	—	—
J212232.58-061839.6	2320-54653-0537	2029409529	10500	0.41	0.86	3.0	0.03	—	—
J212425.74-064837.2	2320-54653-0544	2029399802	16822	0.29	89.23	2.3	0.01	—	—
J212329.46-081004.4	2320-54653-0090	2029383570	15500	0.13	18.3	2.29	0.52	—	—
J221141.80+113604.5	5064-55864-0122	2025529218	9500	-0.35	22.29	18.77	1.05	—	—
J214536.12+062726.8	4091-55498-0588	2025181797	17000	0.27	79.52	2.07	0.21	—	—
J220524.60+010503.3	1105-52937-0404	2024743303	19000	-0.17	73.94	2.49	0.01	—	—
J214900.86+004842.7	1107-52968-0374	2024723147	16000	0.0	67.43	11.04	0.0	—	—
J214539.83+000136.5	0990-52465-0080	2024719715	25000	0.0	33.47	1.8	0.95	—	—
J220435.05+001242.9	0372-52173-0626	2024705114	10500	0.13	12.83	2.15	0.0	—	—
J221828.58-000012.1	0374-51791-0583	2024673588	12239	-0.04	24.85	220.78	6.35	—	—
J222313.51+005446.5	1103-52873-0531	2024670409	8000	-0.35	58.97	2.77	0.01	—	—

SDSS name	PMF	TIC	$T_{eff}(K)$	z_{offset}	incl	B (MG)	dB (MG)	P(h)	dP(h)
J220514.08-005841.6	0373-51788-0243	2024651662	14500	0.42	74.8	3.01	0.02	—	—
J220823.65-011534.1	0373-51788-0086	2024648586	9500	-0.5	35.8	3.04	0.11	—	—
J214930.73-072811.9	0644-52173-0350	2024414691	23000	-0.07	76.42	40.98	15.09	—	—
J222348.44+231909.3	6299-56478-0639	2002636572	8500	-0.5	14.66	6.0	1.11	—	—
J215425.28+272109.5	5964-56098-0187	2001697945	8000	-0.47	12.61	17.94	6.33	78.99	9.63
J215209.66+223039.3	7576-56948-0399	2001282588	8500	-0.39	45.28	7.25	0.18	—	—
J213819.85+112311.3	0731-52460-0632	2000298039	9500	-0.39	3.17	2.19	0.15	—	—
J215148.31+125525.2	0733-52207-0522	2000294335	10000	-0.17	66.83	20.71	0.26	—	—
J213148.69+065930.1	4085-55452-0074	2000028199	8000	-0.25	9.37	31.14	9.18	—	—
J204626.15-071036.9	0635-52145-0227	1996792981	8000	-0.4	46.19	2.58	0.24	—	—
J211744.74-073652.8	2320-54653-0312	1996170022	32642	-0.4	26.25	2.48	0.03	—	—
J205233.51-001610.6	0982-52466-0019	1983770011	18500	-0.37	60.48	15.15	0.23	—	—
J203016.12+765022.6	1661-53240-0116	1981693395	14000	0.07	25.19	3.04	0.02	184.37	6.56
J203828.47+764123.1	1661-53240-0023	1981690827	16000	0.15	14.78	2.16	0.23	157.52	4.79
J201822.88+754807.6	1661-53240-0124	1981686250	14500	0.21	6.6	2.61	1.56	335.59	19.31
J203256.47+142652.1	2258-54328-0278	1939341909	24000	0.38	49.6	3.5	1.73	—	—
J203332.93+140115.4	2258-54328-0295	1939307997	18529	-0.15	87.96	2.16	0.01	—	—
J202501.10+131025.6	2257-53612-0167	1939231328	28932	0.15	10.28	10.06	0.69	—	—
J205000.93+170145.5	2259-53565-0530	1938001273	22000	0.06	8.12	3.11	0.7	—	—
J211125.84+110219.6	1890-53237-0390	1935795461	11000	-0.5	32.99	2.82	0.35	—	—
J211504.83+040009.7	4077-55361-0564	1935171261	8000	-0.23	5.82	4.5	0.31	—	—
J160246.45+303914.5	1405-52826-0283	188595599	40000	0.36	8.92	3.55	0.68	166.62	21.42
J192416.73+614833.1	2563-54653-0255	1884112514	9500	-0.38	54.85	2.58	0.01	111.81	1.61
J192553.59+620708.6	2563-54653-0165	1884107417	9000	-0.31	86.27	2.28	0.01	169.18	3.68
J184130.70+410745.1	2819-54617-0104	1716812127	8000	-0.13	4.28	1.4	0.09	177.35	24.27
J103532.53+212603.5	2376-53770-0534	171647302	8000	-0.35	18.17	2.77	0.15	126.57	24.72
J125715.53+341439.3	2006-53476-0332	165916724	9500	0.37	89.83	22.4	3.91	89.26	6.15
J172735.80+280536.8	2193-53888-0570	1508158233	18084	0.22	87.87	2.14	0.06	166.89	21.49

SDSS name	PMF	TIC	$T_{eff}(K)$	z_{offset}	incl	B (MG)	dB (MG)	P(h)	dP(h)
J174755.71+251232.3	2194-53904-0154	1507729277	10500	-0.3	84.15	2.29	0.03	—	—
J172704.99+084857.1	2818-54616-0374	1505009670	40000	0.0	33.47	1.1	0.07	—	—
J075959.57+433521.1	0437-51869-0369	141117787	9000	-0.38	29.35	91.55	57.78	6.71	0.07
J174235.20+640028.3	2561-54597-0021	1400932592	30000	0.0	33.47	2.0	0.01	173.70	3.88
J172623.13+632607.8	2561-54597-0212	1400926684	25000	0.07	87.22	2.85	0.02	113.47	1.66
J173208.55+631950.3	2561-54597-0087	1400923991	24000	-0.14	6.73	2.3	0.02	164.24	3.47
J173235.19+590533.3	0366-52017-0591	1400842448	11500	-0.36	78.63	2.56	0.04	164.56	3.48
J172932.48+563204.1	0358-51818-0239	1400796107	10000	0.49	0.46	6.0	0.04	—	—
J172045.35+561214.8	0367-51997-0461	1400761333	15000	-0.3	78.71	24.67	0.01	157.21	2.93
J172329.14+540755.7	0359-51821-0415	1400750273	10000	-0.05	53.78	36.82	6.75	69.71	1.07
J173915.64+545059.1	0360-51816-0547	1400728101	16000	0.37	31.91	2.69	0.02	105.39	1.43
J173056.41+433000.4	2820-54599-0185	1400349885	20000	-0.04	0.93	2.45	0.65	1.95	0.0029
J172432.14+323414.9	5002-55710-0601	1400005911	22000	-0.2	50.29	257.2	43.61	169.18	22.08
J113756.50+574022.4	1311-52765-0421	137733927	10080	-0.17	13.73	5.0	0.15	79.04	3.21
J171831.24+280825.6	0980-52431-0434	1309443346	30000	0.43	18.2	3.01	0.38	105.30	8.56
J171711.53+262012.0	5016-55709-0596	1309390554	22000	-0.36	52.32	18.49	0.57	158.20	19.31
J165651.45+243802.7	2191-54621-0608	1309344390	10500	-0.34	69.36	2.54	0.0	nov	—
J170019.41+245701.3	1693-53446-0169	1309341794	30000	0.18	25.83	2.02	0.0	106.03	17.35
J170916.36+234111.3	1688-53462-0508	1309305802	18500	0.19	33.14	4.27	0.31	175.72	47.65
J170657.89+232118.9	1687-53260-0019	1309288045	24000	0.09	17.17	3.31	0.3	166.22	42.64
J164626.65+222645.4	1570-53149-0615	1309132151	14000	0.12	1.4	2.11	0.01	—	—
J165413.92+124344.7	2817-54627-0553	1308209413	8000	-0.17	13.46	1.45	0.05	—	—
J164649.56+120547.0	2817-54627-0308	1308198142	40000	-0.47	54.72	3.07	0.08	—	—
J171556.26+600643.7	0354-51792-0318	1271157230	9500	0.17	27.63	2.07	0.01	81.88	0.86
J171441.07+552711.3	0367-51997-0318	1271054357	30000	0.47	3.84	6.45	1.8	181.16	4.60
J164843.29+461803.7	6027-56103-0970	1270906514	12500	-0.34	41.9	18.04	1.23	66.82	3.45
J165439.46+391103.3	2192-54232-0310	1270634672	9500	-0.24	60.16	2.43	0.01	110.60	9.44
J164703.23+370910.2	5198-55823-0511	1270618314	16500	-0.42	47.55	3.01	0.17	168.82	21.99

SDSS name	PMF	TIC	$T_{eff}(K)$	z_{offset}	incl	B (MG)	dB (MG)	P(h)	dP(h)
J171959.47+331614.9	4994-55739-0097	1270424730	21000	0.22	88.33	2.2	0.22	82.33	5.23
J165203.67+352815.7	0820-52438-0299	1270319264	18778	0.2	76.02	10.62	0.3	45.90	3.25
J165029.90+341125.4	1175-52791-0482	1270312778	10500	-0.5	43.28	3.05	0.02	166.22	42.64
J165249.08+333444.9	1175-52791-0095	1270304405	8500	-0.12	57.86	4.58	0.1	104.24	16.77
J170123.81+330853.9	4992-55723-0866	1270276445	12206	-0.32	0.92	37.71	1.24	39.68	2.43
J164342.37+315728.7	5194-56062-0546	1270246087	15500	0.29	73.53	2.25	0.08	106.03	17.35
J170400.00+321328.5	0976-52413-0319	1270207404	25000	0.49	5.16	3.44	0.01	161.84	40.42
J164359.14+273047.7	4190-55686-0984	1270103746	10500	0.27	51.96	2.86	0.04	—	—
J165538.92+253346.2	1692-53473-0163	1270054782	15500	0.32	39.02	2.76	4.34	12.37	0.24
J165354.57+251738.4	1692-53473-0213	1270051358	19000	0.0	33.47	1.2	0.0	nov	—
J164357.02+240201.3	1414-53135-0191	1270024898	23000	0.01	1.02	2.47	1.59	nov	—
J163334.67+194229.7	4061-55362-0761	1205040141	17500	-0.38	44.55	2.67	0.5	106.03	17.35
J161929.62+131833.4	2530-53881-0332	1204864430	22000	0.0	33.47	2.9	0.0	—	—
J163400.34+145651.3	2209-53907-0472	1204845860	15500	0.25	8.55	5.5	0.0	—	—
J163013.93+123941.9	2533-54585-0325	1204793195	13500	0.17	0.3	2.08	0.01	—	—
J163630.30+114452.2	2533-54585-0502	1204746330	10500	0.42	2.18	3.0	0.0	—	—
J160532.18+131748.6	2525-54569-0425	1204706898	19000	0.0	33.47	1.7	0.08	—	—
J160219.42+112606.4	2525-54569-0303	1204684690	9500	-0.03	37.9	2.53	0.0	—	—
J160540.06+093724.8	2526-54582-0223	1204635147	16000	0.17	19.33	2.17	0.01	—	—
J161050.03+094302.4	2526-54582-0115	1204598962	25000	0.0	33.47	2.7	0.0	—	—
J162115.34+075059.0	1732-53501-0455	1204540315	12000	0.29	34.17	2.19	0.01	—	—
J161658.43+070355.4	1731-53884-0442	1204481546	12500	0.46	25.95	3.19	0.44	—	—
J160852.00+064437.0	1730-53498-0252	1204470999	8500	-0.24	73.69	24.86	0.14	—	—
J163917.45+103604.9	4075-55352-0101	1204444252	8000	-0.21	16.94	1.45	0.06	—	—
J160100.43+044236.3	4808-55705-0318	1203978163	11500	-0.28	7.6	44.79	28.35	—	—
J161425.46+493244.9	2884-54526-0254	1201058683	11500	0.44	7.93	3.0	0.01	81.17	5.08
J162727.70+492507.9	0625-52145-0578	1201047378	11000	0.0	33.47	1.1	0.01	319.02	52.35
J163900.06+440808.0	6030-56097-0034	1200990575	13000	0.39	15.02	2.85	0.17	32.00	0.79

SDSS name	PMF	TIC	$T_{\rm eff}(K)$	z_{offset}	incl	B (MG)	dB (MG)	P(h)	dP(h)
J160437.35+490809.2	0622-52054-0330	1200962683	9000	-0.15	13.42	37.97	15.25	367.55	69.49
J160929.96+443857.1	0814-52370-0317	1200925570	30000	0.0	33.47	1.5	0.11	40.99	1.30
J160531.60+385210.0	5200-56091-0678	1200833193	13000	0.38	13.62	2.67	0.11	105.16	8.53
J161710.49+383306.9	5199-56067-0720	1200822323	16500	0.29	76.34	2.45	0.1	35.64	0.98
J161030.50+365442.3	1056-52764-0440	1200810962	23000	0.19	27.22	2.16	0.07	320.75	79.38
J163458.64+415820.0	6036-56093-0308	1200793211	24000	-0.13	52.66	2.06	0.23	84.97	5.57
J163600.24+354625.3	2185-53532-0320	1200673439	25000	0.48	3.71	9.97	3.71	154.58	18.44
J163841.66+334302.1	1339-52767-0092	1200664365	9500	-0.2	70.44	2.19	0.06	346.76	92.78
J163036.79+272451.5	5005-55751-0254	1200400592	11500	-0.19	52.96	35.6	6.3	102.50	16.21
J161118.59+242446.6	1657-53520-0372	1200353727	11000	0.0	33.47	1.3	0.04	83.84	5.42
J161047.77+235301.8	1852-53534-0567	1200348008	14500	0.5	4.57	3.4	0.85	164.68	20.93
J162808.39+233254.1	1573-53226-0099	1200281969	8000	-0.21	18.64	4.77	0.21	5.30	0.04
J161147.94+211136.6	2205-53793-0542	1200169531	10000	0.23	5.58	2.19	0.0	66.48	3.41
J162304.10+183522.2	4060-55359-0296	1200094031	14000	0.28	81.41	2.5	0.07	107.89	17.96
J162216.01+184019.4	4073-55663-0806	1200082308	16500	0.5	6.56	3.43	0.08	116.04	20.78
J160904.12+175337.7	2967-54584-0089	1200063047	9000	-0.24	72.96	2.43	0.17	104.24	16.77
J161344.78+174609.0	2188-54595-0406	1200046061	15500	0.43	32.14	2.96	0.09	175.71	47.65
J161321.40+155332.0	2198-53918-0400	1200030839	9500	0.47	4.03	3.3	0.02	—	—
J160357.92+140929.9	2524-54568-0247	1200005440	9500	-0.24	52.38	49.4	58.55	—	—
J145602.52-005548.7	0921-52380-0528	1180160128	20000	0.0	33.47	2.1	0.0	—	—
J145231.59-025634.1	4023-55328-0122	1180140797	11500	-0.32	72.23	2.28	0.28	—	—
J155651.11+085003.5	1728-53228-0374	1103812251	10500	-0.14	74.13	2.19	0.04	—	—
J155932.57+081904.6	1728-53228-0175	1103804720	13000	0.0	33.47	1.3	0.01	—	—
J154213.46+034800.3	0594-52045-0400	1103614406	9500	-0.19	46.3	8.58	0.17	—	—
J154135.01+030051.1	0594-52045-0253	1103600501	13500	0.0	33.47	3.6	0.02	—	—
J154120.14+022756.5	0594-52045-0315	1103593437	23000	0.12	14.85	3.21	0.18	—	—
J154524.79+010127.5	2955-54562-0061	1103556324	19500	0.0	33.47	2.4	0.03	—	—
J150220.91+001721.1	0539-52017-0202	1103450900	10000	0.0	33.47	2.2	0.02	—	—

SDSS name	PMF	TIC	$T_{eff}(K)$	z_{offset}	incl	B (MG)	dB (MG)	P(h)	dP(h)
J153349.02+005916.1	2954-54561-0048	1103401950	9500	-0.17	65.27	2.62	0.48	—	—
J152855.62-015148.7	0925-52411-0312	1103320315	19500	0.18	0.31	2.4	0.0	—	—
J155238.20+003910.4	0342-51691-0639	1103265263	12500	0.12	41.32	2.16	0.08	—	—
J144408.75+024327.8	0537-52027-0371	1102792408	10500	-0.11	24.11	2.5	0.02	—	—
J144649.26+005215.3	0537-52027-0126	1102778560	18500	0.17	0.8	2.1	0.0	—	—
J144114.21+003702.3	0307-51663-0595	1102771937	21000	0.49	20.7	4.39	0.49	—	—
J144614.00+590216.6	0608-52081-0140	1102343597	16000	0.31	21.27	10.21	0.07	177.60	12.17
J151745.18+610543.6	0613-52345-0446	1102335047	15000	0.36	0.68	23.79	0.09	102.54	3.25
J145636.32+583321.1	0610-52056-0189	1102310706	9500	-0.35	54.75	2.47	1.2	79.28	2.42
J153315.25+564200.2	0614-53437-0579	1102244954	11000	0.0	33.47	2.5	0.0	107.28	4.44
J153301.51+550840.9	0614-53437-0079	1102239509	9500	0.0	33.47	3.6	0.05	170.44	11.21
J153829.29+530604.6	0795-52378-0637	1102186362	9500	0.12	61.27	16.12	0.04	170.44	14.94
J144345.84+482008.9	1047-52733-0099	1102118227	22000	0.12	36.94	2.02	0.01	182.04	25.57
J144541.71+411441.5	1397-53119-0352	1102033358	21000	0.49	3.68	4.29	0.84	107.42	8.90
J144405.60+405338.0	5172-56071-0676	1102032244	25000	-0.17	75.76	2.56	0.12	165.23	21.07
J145414.99+432149.4	1290-52734-0469	1102031582	11500	-0.5	45.85	3.26	0.05	115.76	6.89
J155857.29+480047.3	0813-52354-0328	1101949583	10000	0.25	81.07	2.42	0.01	168.77	21.98
J151102.74+433558.7	1677-53148-0151	1101880185	13000	0.14	2.1	2.19	0.0	333.20	85.67
J151130.16+422022.9	6048-56072-0374	1101874829	11500	-0.28	34.91	12.83	16.96	122.41	11.56
J150813.26+394505.1	1398-53146-0633	1101856210	29032	-0.21	25.68	6.4	1.11	324.88	81.44
J153742.29+434719.7	1052-52466-0619	1101848256	40000	0.24	0.85	2.86	2.62	69.12	3.69
J153532.25+421305.5	1052-52466-0252	1101835037	22000	0.0	33.47	2.8	0.01	167.66	21.69
J153948.03+404528.5	4976-56046-0553	1101829695	12500	-0.35	59.56	18.84	2.75	107.54	17.85
J153057.48+394614.8	1293-52765-0613	1101825735	25000	0.5	3.65	2.2	0.01	393.79	119.65
J153554.17+404414.2	1679-53149-0109	1101825483	30000	0.22	6.36	2.39	0.01	190.96	28.14
J155436.25+413956.6	1334-52764-0235	1101777963	23000	0.31	14.28	13.14	0.08	—	—
J155651.96+351218.9	1417-53141-0512	1101672680	8000	-0.5	46.1	3.07	0.1	147.56	33.60
J154305.66+343223.6	1402-52872-0145	1101661187	30620	0.47	81.04	4.98	0.12	288.41	64.18

SDSS name	PMF	TIC	$T_{eff}(K)$	z_{offset}	incl	B (MG)	dB (MG)	P(h)	dP(h)
J145330.84+390245.2	5174-56047-0828	1101578522	13500	0.31	77.93	2.29	0.13	393.79	119.65
J144331.21+262423.9	6022-56076-0670	1101422311	40000	0.5	3.19	4.78	0.2	118.01	21.49
J151835.81+311911.4	3879-55244-0584	1101392852	8500	-0.23	71.71	2.61	0.08	162.69	40.85
J152934.98+292801.8	1652-53555-0436	1101333652	10000	-0.44	67.06	2.82	0.29	—	—
J154012.07+290828.9	4722-55735-0206	1101323405	40000	-0.49	17.53	11.95	0.3	2.38	0.01
J151606.34+274647.0	2154-54539-0637	1101301512	30000	-0.44	75.43	3.03	0.06	317.25	155.32
J151516.47+244547.7	3961-55654-0708	1101193939	8000	-0.46	67.54	16.39	1.88	166.97	43.02
J145829.87+223040.6	6020-56087-0312	1101173917	9500	-0.15	62.98	32.53	10.51	23.94	0.88
J150809.79+215037.0	3962-55660-0428	1101159910	15000	-0.47	27.66	17.5	2.77	317.25	155.32
J155232.76+264636.6	2474-54564-0392	1101073151	19362	0.0	33.47	1.1	0.0	109.40	18.47
J154605.40+243759.0	1850-53786-0312	1101003811	8000	0.0	33.47	1.1	0.11	nov	—
J154855.04+245112.9	3947-55332-0016	1101003368	17500	-0.39	69.19	8.41	1.3	317.25	155.32
J155818.96+241758.7	1851-53524-0476	1100993822	17500	0.13	8.91	7.19	0.89	75.47	4.39
J155657.69+231358.5	1851-53524-0298	1100985887	13000	0.48	12.55	3.27	0.05	80.69	5.02
J154856.93+230727.9	2169-53556-0491	1100974496	9732	-0.42	62.8	2.81	0.1	176.25	47.94
J152203.44+203438.9	2156-54525-0031	1100904085	14000	0.26	0.85	2.98	0.03	162.69	40.85
J152401.59+185659.2	3945-55648-0726	1100825858	9500	-0.18	21.15	6.49	0.97	—	—
J154141.84+173026.2	2795-54563-0603	1100727827	16500	0.15	0.51	2.19	0.0	—	—
J155202.55+170434.7	3926-55327-0738	1100710903	8000	-0.36	16.89	2.62	0.02	—	—
J154626.16+143754.8	4890-55741-0988	1100630476	30000	0.42	88.92	2.99	0.4	—	—
J154424.84+132650.8	2517-54567-0110	1100599391	13000	0.22	27.14	2.06	0.07	—	—
J154550.71+132040.2	2517-54567-0065	1100594915	10000	-0.32	77.09	2.81	0.02	—	—
J154238.25+101156.9	5206-56033-0032	1100550858	11500	-0.37	72.58	2.56	0.08	—	—
J151436.65+152058.4	2766-54242-0497	1100478964	10500	-0.49	50.42	3.08	0.15	—	—
J152936.81+123436.8	2754-54240-0371	1100335642	10500	-0.36	73.12	2.52	0.07	—	—
J150957.07+092349.3	5487-55982-0596	1100298525	10000	-0.17	9.06	6.0	0.25	—	—
J153843.10+084238.2	1725-54266-0297	1100235123	33803	0.03	43.78	12.66	0.27	—	—
J151415.65+074446.4	1817-53851-0534	1100207634	10090	-0.31	48.53	37.07	11.91	—	—

SDSS name	PMF	TIC	$T_{eff}(K)$	z_{offset}	incl	B (MG)	dB (MG)	P(h)	dP(h)
J145029.51+032218.8	0587-52026-0016	1100095837	22000	0.18	5.7	2.65	0.0	—	—
J144934.72+025502.7	0537-52027-0566	1100092845	8000	-0.49	4.25	3.61	0.02	—	—
J150451.71+052141.0	4776-55652-0509	1100079691	17500	-0.32	69.96	5.25	0.18	—	—
J145801.09+040917.0	0588-52029-0639	1100045573	16500	0.47	13.25	3.19	0.01	—	—
J132203.94+193223.1	2619-54506-0423	1003073445	18000	0.17	1.92	4.09	1.27	—	—
J132002.47+131901.5	1773-53112-0011	1003033181	21000	0.04	4.27	3.17	0.96	38.63	2.30
J133156.48+124055.9	5432-56008-0858	1002999997	20000	-0.18	76.37	2.28	0.29	nov	—
J133007.57+104830.5	1699-53148-0137	1002982830	8000	-0.09	47.51	2.16	0.08	nov	—
J135204.28+112055.2	5445-55987-0622	1002947861	18000	0.16	89.99	2.35	0.07	230.19	81.77
J134845.98+110008.8	5445-55987-0530	1002946285	16500	0.19	4.31	202.58	14.94	199.84	61.63
J135048.10+084512.6	5442-55978-0820	1002882671	8000	-0.1	47.65	2.15	0.08	89.86	12.46
J135107.02+074345.5	5442-55978-0132	1002877007	9500	-0.23	58.02	2.19	0.04	—	—
J133738.54+072440.2	5437-55973-0404	1002834674	13500	0.46	3.59	3.15	0.2	95.62	14.11
J142955.20+044005.4	0585-52027-0467	1002649312	12500	-0.38	67.92	2.57	0.02	—	—
J143147.14+012153.0	4024-55646-0304	1002438987	12000	0.39	74.35	2.72	0.14	—	—
J134043.10+654349.2	6825-56717-0206	1001464194	11500	-0.5	31.5	3.27	0.22	116.69	7.00
J133836.06+652433.1	2460-54616-0042	1001409035	19000	0.16	0.63	2.19	0.01	—	—
J133340.34+640627.3	0603-52056-0112	1001407271	9500	-0.05	13.97	7.25	0.19	284.61	25.00
J133819.06+624018.7	6816-56444-0668	1001395018	13000	-0.25	8.42	40.0	4.22	65.01	1.63
J134017.70+594552.5	0786-52319-0254	1001378245	35770	-0.36	77.51	2.6	0.02	116.00	6.92
J132858.19+590851.0	7117-56685-0012	1001375730	18000	-0.5	1.59	15.43	1.34	108.68	6.08
J141710.80+573546.1	2462-54561-0404	1001310908	8000	-0.04	23.52	2.5	0.07	168.39	10.94
J143632.86+563525.2	0791-52435-0304	1001302478	8500	0.0	33.47	1.1	0.03	115.25	5.12
J142118.19+523547.0	1326-52764-0250	1001274702	25000	0.24	15.78	2.77	0.7	82.61	5.27
J132208.55+551939.0	6828-56430-0780	1001231850	9500	-0.22	44.31	2.91	1.34	114.71	6.77
J132538.57+515152.2	1668-53433-0326	1001198308	10000	0.45	13.0	3.15	0.01	110.07	6.23
J140716.66+495613.7	6746-56386-0678	1001123368	18500	0.41	89.92	15.43	0.48	115.65	10.32
J141808.12+481850.6	1672-53460-0181	1001088554	13000	-0.32	73.22	2.28	0.04	178.29	16.35

SDSS name	PMF	TIC	$T_{eff}(K)$	z_{offset}	incl	B (MG)	dB (MG)	P(h)	dP(h)
J140821.99+443008.0	1467-53115-0557	1001064129	12500	0.47	7.7	3.2	0.01	301.64	70.21
J134131.64+440030.0	6626-56330-0744	1001042061	8000	-0.21	6.54	40.62	80.27	140.26	15.18
J133828.43+415943.8	1464-53091-0605	1001022306	17500	0.46	14.23	3.24	0.66	178.90	16.46
J134820.79+381017.2	3852-55243-0676	1000978148	25000	-0.36	59.1	15.52	4.67	168.82	43.98
J143235.46+454852.4	2932-54595-0542	1000963565	22000	0.43	9.51	11.72	1.93	62.21	2.99
J143218.25+430126.7	1396-53112-0338	1000935382	30000	-0.01	43.03	2.65	0.02	73.91	4.22
J142836.95+383904.9	4713-56044-0844	1000915247	8000	-0.36	10.53	7.0	0.55	176.47	24.03
J135654.77+343617.2	1838-53467-0240	1000869898	30000	0.5	2.96	9.3	2.32	68.42	7.22
J142703.35+372110.5	4713-56044-0230	1000854473	14500	-0.35	65.56	32.06	6.16	183.98	26.12
J141813.21+312340.0	2129-54252-0426	1000810214	8000	-0.37	17.57	2.55	0.12	233.71	84.29
J134024.99+325028.7	3856-55269-0462	1000746564	25000	-0.07	59.41	2.36	0.31	42.20	2.75
J140051.72+330754.3	2121-54180-0369	1000715873	30000	0.28	5.69	3.15	1.04	—	—
J140750.65+301130.2	6495-56339-0886	1000638018	23000	-0.07	27.98	86.0	10.48	114.55	20.25
J132926.04+254936.4	2245-54208-0307	1000579641	28299	-0.39	54.04	2.61	0.18	51.32	4.06
J133025.70+224813.6	2653-54230-0408	1000538867	10000	-0.48	61.25	3.19	0.01	193.44	57.75
J143019.05+281100.8	2134-53876-0423	1000465653	9000	-0.15	18.21	7.26	1.09	106.92	17.64
J143122.55+261026.4	6017-56075-0646	1000460165	9500	0.1	27.59	2.03	0.03	324.87	81.44
J141906.19+254356.4	2131-53819-0317	1000428883	9500	-0.3	60.26	2.27	0.3	178.20	49.01
J141604.48+235404.2	6013-56074-0656	1000376190	14000	0.3	76.82	2.27	0.36	116.64	21.00
J134913.52+205646.9	5869-56064-0446	1000332438	11413	-0.08	69.0	385.05	34.49	—	—
J140444.21+201922.6	2771-54527-0196	1000298498	14500	-0.24	76.47	2.13	0.01	101.75	15.98
J141309.30+191831.9	2772-54529-0217	1000287443	14000	-0.31	67.01	2.53	0.05	173.38	46.39
J135206.28+175333.0	2930-54589-0051	1000274176	8000	0.16	11.14	2.19	0.02	13.73	0.29
J140709.72+154010.2	2745-54231-0343	1000159163	13500	-0.12	62.17	22.82	0.0	258.13	102.83
J141307.56+121537.4	5453-56001-0030	1000098649	30000	-0.44	74.88	2.96	0.29	—	—
J142035.36+112042.2	5460-56000-0598	1000088671	13000	0.43	15.18	3.0	0.11	—	—
J142708.16+100910.9	5465-55988-0464	1000051071	16500	0.26	65.73	2.23	0.17	—	—
J142003.63+103930.4	5456-55980-0016	1000050254	12500	0.32	86.15	2.26	0.11	—	—

SDSS name	PMF	TIC	$T_{eff}(K)$	z_{offset}	incl	B (MG)	dB (MG)	P(h)	dP(h)
J143308.49+102623.0	1709-53533-0511	1000041445	8000	-0.37	18.51	2.49	0.22	—	—
J143506.35+072940.3	5467-55973-0321	1000013638	11500	-0.37	73.66	2.54	0.08	—	—
J053126.75+001738.1	2072-53430-0427	—	13000	0.11	15.24	2.06	0.02	—	—
J225123.66+293945.3	2621-54380-0042	—	8000	-0.17	29.36	1.80	0.08	—	—
J230119.48+101939.0	6154-56237-0386	—	9000	-0.079	36.48	7.34	0.04	—	—
J000505.48+183548.0	6170-56240-0212	—	11500	-0.096	67.88	2.15	0.01	—	—
J004104.51+303819.4	6252-56248-0866	—	9000	0.14	2.24	2.00	0.02	—	—
J085159.32+532540.3	0449-51900-0311	802249299	11500	-0.17	13.81	63.76	28.16	nov	—
J135141.13+541947.2	1323-52797-0293	141874000	10180	0.16	20.4	778.51	0.00	190.95	18.76
J082108.17+372738.3	2674-54097-0103	801799872	8000	-0.33	16.25	0.60	0.00	—	—
J075137.54+670732.3	2944-54523-0569	743292177	8000	-0.17	12.87	0.90	0.00	1.22	0.0023
J163350.80+150822.6	4068-55445-0746	1204846541	40000	0.50	3.81	3.52	12.01	—	—
J090139.03+064022.4	4868-55895-0730	800141986	8000	-0.2	17.5	0.80	0.00	nov	—
J153049.68+344434.7	4975-56037-0762	1101700128	37472	-0.47	63.27	10.43	5.91	317.25	155.32
J105544.90+211105.0	5876-56042-0550	337298217	8000	-0.25	6.98	0.50	0.00	170.79	45.01
J224459.60+331017.3	7142-56567-0966	2040290781	20000	0.30	44.69	421.87	13.77	nov	—
J094351.25+010104.0	0480-51989-0251	842141925	9500	-0.2	89.08	2.19	erro	149.87	17.33
J125434.64+371000.1	1989-53772-0041	17666311	25365	-0.28	0.95	2.64	5.11	nov	—
J074126.28+394118.7	3670-55480-0528	741594878	8000	-0.24	9.23	1.45	0.03	—	—
J075916.53+433518.9	3676-55186-0030	741591188	22420	-0.27	44.98	2.29	0.00	nov	—
J133420.95+041751.3	4786-55651-0518	1002798094	17415	-0.27	73.8	2.43	0.15	5.56	0.05
J155708.02+041156.4	4808-55705-0466	1103633059	23000	-0.08	60.16	40.7	9.41	—	—
J155835.80+122139.4	4901-55711-0358	1103854354	24000	-0.3	88.31	2.13	0.58	—	—
J171102.58+360959.6	4989-55743-0414	1270505616	20546	0.11	14.34	2.30	0.07	61.14	2.88
J150813.26+394505.1	5167-56066-0732	471015260	29032	-0.05	15.13	12.95	9.75	324.88	81.44
J085817.39+471501.2	5735-55980-0410	802113874	10317	-0.42	63.34	2.82	0.14	nov	—
J114828.99+482731.1	6678-56401-0952	900301873	30000	0.37	27.36	41.58	134.21	120.18	22.29
J134758.88+495427.4	6744-56399-0957	1001117148	16628	-0.3	72.13	2.29	0.23	352.94	64.08

D) Resumo simplificado estilo nota de imprensa (press release)

Ajudando a entender a origem de Campos Magnéticos em estrelas Anãs Brancas

A dissertação de Mestrado intitulada “Anãs Brancas Magnéticas ricas em Hidrogênio" da aluna Larissa Luciano Amorim, do Programa de Pós Graduação em Física da Universidade Federal do Rio Grande do Sul, apresenta o maior catálogo de estrelas anãs brancas com campo magnético determinado.

As anãs brancas são excelente laboratório de pesquisa na busca para compreender a natureza e suas leis. Essas estrelas representam o estágio final de evolução de mais de 97% das estrelas e podem apresentar temperaturas, pressões e campos magnéticos inatingíveis na Terra. As altas pressões são decorrentes da concentração de massas tão grandes como a do Sol em espaços tão pequenos quanto o tamanho do nosso planeta. Outra característica relevante dessas estrelas é o fato elas emanarem calor muito lentamente, resfriando durante bilhões de anos. Assim, eventualmente, as temperaturas no núcleo são suficientemente baixas, que em conjunto com as altas pressões, fazem com que este se torne um cristal. Modelos teóricos nos informam se anãs brancas com determinada temperatura e massa já devem ter iniciado ou não seu processo de cristalização.

Já com relação ao campo magnético presente nessas estrelas, existem várias hipóteses de como podem ter surgido. As principais são: um campo magnético interno já existia em etapas anteriores da evolução da estrela e foi apenas conservado e “exposto" quando a estrela se torna uma anã branca; o campo magnético surge na formação da anã branca, quando esta interage com uma estrela companheira, em um sistema binário; o campo magnético é formado durante o processo de resfriamento da anã branca.

Para entender melhor o campo magnético se origina nessas estrelas e afeta outras características estelares determinamos sua intensidade em 808 anãs brancas ricas em hidrogênio e o periodo de variabilidade temporal para 380 dessas estrelas. Além disso, analisamos dados de temperatura e massa, determinando quais já tinham iniciado a cristalização.

A determinação do campo magnético se baseou no fato de que as estrelas emitem luz em cada cor(frequência) de maneira diferente, o que chamamos de espectro. Algumas cores não chegam até nós por serem absorvidas por átomos na atmosfera da estrela. Essa absorção maior em uma determinada cor é chamada de linha de absorção. Ela se divide na presença de um campo magnético, fenômeno conhecido como Efeito Zeeman. Por exemplo,

uma linha pode se dividir em três e a separação entre as linhas adicionais e a original é proporcional à intensidade do campo magnético. Existem modelos teóricos de como essas linhas devem se comportar sob a influência de campos magnéticos de diferentes intensidades. Esses modelos foram comparados com espectros reais de estrelas observados com o telescópio *Sloan Digital Sky Survey*.

Já a determinação dos períodos de variabilidade se fundamentou na medida de toda a luz da estrela observada a cada 30 minutos pelo telescópio espacial *Transiting Exoplanet Survey Satellite*. Com esses dados pode-se construir uma curva de como a luz varia com o tempo e procurar variações cíclicas, determinando assim um período de variabilidade. Esse período é associado à rotação da estrela em torno do seu próprio eixo.

A análise dos resultados levou à conclusão de que as anãs brancas com campos magnéticos mais altos tendem a apresentar massas mais elevadas, temperaturas mais baixas e processo de cristalização já iniciado, reforçando a hipotese de o campo estar sendo gerado e/ou amplificado já no processo de resfriamento da anã branca.